Simulating the kinematics of damped Lyman alpha systems

PERRY, ROBERT,EDWIN

Simulating the Kinematics of Damped Lyman α Systems

Robert Edwin Perry

Submitted for the degree of Master of Philosophy
March 2015

Abstract

We investigate the kinematic properties of simulated Damped Lyman-α Absorption (DLA) systems at redshift $z = 3$ via associated low ionization metal absorption. These multiple-component optical depth profiles provide a direct measure of the dynamical motion of the underlying neutral gas. In particular we focus on the velocity width (extent) of these systems along 1D lines of sight using the v_{90} statistic. We utilize a large set of cosmological, hydrodynamical simulations sourced from the OverWhelmingly Large Simulations (OWLS) project, post-processed for radiative transfer using the 3D reverse ray tracing code URCHIN. We succeed in generating complex and high velocity width systems up to $\sim$ 1000 km/s. However we also produce a persistent overabundance of low velocity width ($v_{90} < 30$ km/s) systems. We investigate the dependencies of the DLA Velocity Width Distribution (VWD) and quantify the physical origin of sightline kinematics using a novel approach. We uncover a slight bias against low velocity width measurements due to intrinsic saturation of unresolved absorbers, potentially weakening the observed v_{90} - metallicity correlation. We find that sightline kinematics are highly stochastic even for isolated host halo systems, reflecting the diverse configurations of neutral gas that may be probed by an unassociated background quasar.

Email: robert.perry100@outlook.com

Simulating the Kinematics of Damped Lyman α Systems

Robert Edwin Perry

A Thesis presented for the degree of
Master of Philosophy

The Institute for Computational Cosmology
Department of Physics
Durham University
England

March 2015

Contents

List of Figures

List of Terms and Acronyms

ΛCDM Λ Cold Dark Matter – cosmological model

CDDF Column Density Distribution Function – $d^2n/dNdX$

CGM Circum-Galactic Medium

CLOUDY A spectral synthesis code designed to simulate conditions in interstellar matter under a broad range of conditions

DLA Damped Lyman-α Absorption – $N_{\rm HI} > 10^{20.3}{\rm cm}^2$

EoS Equation of State – (polytropic) relationship between density and pressure

Friends-of-Friends Friends-of-Friends – a structure identification technique

FWHM Full Width Half Maximum

GADGET A smoothed particle hydrodynamic simulation code designed for cosmological simulations

HIRES High Resolution Echelle Spectrometer

HPC High Performance Computing

ICC Institute for Computational Cosmology

IGM Inter-Galactic Medium

IP Ionisation Potential

ISM Inter-Stellar Medium

LAF Lyman-α Forest $N_{\rm HI} < 10^{17.2}{\rm cm}^2$

LLS Lyman Limit System $10^{17.2} < N_{\rm HI} < 10^{20.3}{\rm cm}^2$

OWLS OverWhelmingly Large Simulations – project / suite of cosmological, hydrodynamic simulations

PDF Probability Density Function – of integral 1

PF Probability Function – of sum 1

QSO Quasi-Stellar Object

SpecWizard A transmission spectra and 1D projection (from SPH) code – available on request

SDSS Sloan Digital Sky Survey

SPH Smoothed Particle Hydrodynamics

STFC Science and Technology Facilities Council

TreePM Tree Particle Mesh - a method for carrying out large N-Body simulations

URCHIN An accurate, 3D radiative transfer, reverse ray-tracing code

UVB Ultraviolet Background – isotropic, photoionising radiation field

VWD Velocity Width Distribution – $d^2n/d{\rm v}_{90}dX$

WMAP Wilkinson Microwave Anisotropy Probe

Declaration & Statement of Copyright

The work in this thesis is based on research carried out by the author between October 2012 and March 2015 under the supervision of Professor Tom Theuns and Professor Richard Bower at the Institute for Computational Cosmology, Department of Physics, Durham University, England. No part of this thesis has been submitted for any other degree or qualification at Durham University or elsewhere. All figures in this thesis were produced by the author except where stated otherwise in the figure captions. All of the work presented in this thesis was carried out by the author except where properly acknowledged in the text.

Acknowledgments

I am truly grateful to everyone who has contributed towards my postgraduate training at Durham University; in particular I'd like to thank my supervisors Professor Tom Theuns and Professor Richard Bower for guiding me and developing my scientific mind, and Professor Carlton Baugh for all of the invaluable outreach opportunities I've enjoyed.

Of course, my time as a postgraduate student has been made all the brighter thanks to the support of the many friends I've made in the department. You should all know how much I have valued our time together and I hope to always stay in touch.

Last but not least, I'd like to thank Dr Gabriel Altay and the OWLS project team for providing the amazing simulation data utilized by this project.

I would like to acknowledge the generous support of a Science and Technology Facilities Council (STFC) postgraduate studentship without which none of this would have been possible.

This work used the DiRAC Data Centric system at Durham University, operated by the Institute for Computational Cosmology (ICC) on behalf of the STFC DiRAC HPC Facility (www.dirac.ac.uk). This equipment was funded by BIS National E-infrastructure capital grant ST/K00042X/1, STFC capital grant ST/H008519/1, and STFC DiRAC Operations grant ST/K003267/1 and Durham University. DiRAC is part of the National E-Infrastructure.

This work was undertaken as part of the Virgo Consortium research programme. This thesis was typeset using a (modified) open source LaTeX template kindly provided by M. Imran.

Dedicated to
My growing family


Durham
University


ICC


The
Ogden
Trust


Science & Technology
Facilities Council


DiRAC


VIRGO

Chapter 1

Introduction

Over the past century, the advent of new technologies has allowed the astronomy community to gain a detailed understanding of galaxy formation and evolution over cosmic time, ever motivated by the latest generation of extra-galactic observations. Despite never venturing far from our terrestrial home, we now grasp a sufficient knowledge of physics to successfully model all manner of galaxy properties and their global distributions under the ΛCDM cosmological paradigm. However, it is becoming increasingly apparent that traditional avenues in astronomy are fast approaching a limit on what they can achieve. For example, ground breaking surveys now require years or even decades of observing time in order to surpass the results of their previous generations. Other examples include the 40m class European Extremely Large Telescope and the Square Kilometer Array, surely representing the ultimate iterations of ground based observational facilities. So, rather than saturating the literature with an endless re-analysis of the same astronomical principals, it is now up to the community to innovate and explore the myriad of unrealized avenues in astronomy if we are to truly develop our understanding of the Universe. One such emerging area is that of damped Lyman α kinematics, which we thoroughly investigate in this work by means of cutting edge cosmological, hydrodynamical simulations. Such simulations provide us with an unprecedented utility in testing our understanding of galaxy formation and evolution; incorporating the world's cumulative knowledge of astronomical scale physics in their entirety. Only by scrutinizing these cyber space universe simulations do we have the opportunity to hypothesize,

investigate and constrain new, exciting astronomical principals that could never be experimented with in the laboratory.

1.1 Damped Lyman α

DLA is a class of intervening Quasi-Stellar Object (QSO) absorption feature with an atomic hydrogen column density exceeding $N_{DLA}(\mathrm{HI}) = 10^{20.3}$ cm^{-2} (Wolfe et al., 1986). Unlike optically thin Lyman-α forest absorbers ($N_{\mathrm{HI}} < 10^{17.2}$cm^{-2}) and Lyman Limit Systems (LLS, $10^{17.2} < N_{\mathrm{HI}} < 10^{20.3}$ cm^{-2}), DLAs are mainly neutral, being self-shielded to the photoionizing background radiation field that pervades the Universe.

As star forming regions are assumed to condense from the same cold, dense, neutral hydrogen gas that gives rise to the DLA system, understanding the nature of DLA host systems is essential for a complete picture of galaxy formation and evolution. Indeed, DLA systems contain the dominant fraction of neutral gas in the Universe since reionisation (Noterdaeme et al., 2009); encompassing the ISM of galaxies as well as the loosely defined Circum-Galactic Medium (CGM).

Unfortunately, associating DLAs directly with galactic counterparts remains an observational challenge due to the obscuring nature of the background QSO, compounded by the possibility that DLA host galaxies may be faint; see for example Fumagalli et al. (2014). As a consequence, a full consensus on the nature of DLA hosts has yet to be reached.

However, in adversity there lies opportunity; namely that if typical DLA host systems are indeed too faint to be studied in emission, then DLA absorption studies provide us with a window into an otherwise unexplored domain of the Universe. We believe DLA systems have the potential to provide powerful constraints on galaxy formation and evolution theories, out to high redshifts.

See Wolfe, Gawiser & Prochaska (2005) for an excellent review on DLA systems.

1.2 Sightline kinematics

At such high column densities, the damped Lyman-α line is saturated over a broad region of velocity space, making it impossible to measure the dynamics of neutral gas solely from H I absorption. However, low ionisation metal species such as e.g. Si II and Fe II will trace the kinematics of the cold neutral gas as they have similar ionisation potentials to H I. By associating unsaturated low ionisation metal absorption features with DLA at the same redshift, we can infer kinematic properties of the underlying host system along 1D lines of sight.

The principal kinematic property of DLAs is the velocity width or v_{90} statistic, as originally defined by Prochaska & Wolfe (1997). This statistic provides us with a measure of the velocity extent of the underlying neutral gas, which may indicate the presence of galactic winds and may potentially constrain the host halo mass.

However, reproducing the kinematic properties of DLA systems has faced limited success, despite significant effort by the community to reproduce their observed properties using semi-analytic models and hydrodynamic simulations.

The attention of most recent works has been on matching the velocity width distribution of 100 high resolution (down to 1.4 km/s) DLA spectra, as presented in Prochaska (2003); Prochaska, Herbert-Fort & Wolfe (2005). These spectra were later re-examined and expanded upon by Neeleman et al. (2013) (hereafter N13).

We will frequently refer to the VWD in this work, defined to be the number of DLA features per unit absorption distance X per velocity width (v_{90}): $\frac{d^2n}{dX dv_{90}}$ where dX is related to the redshift path dz as $dX/dz = H_0(1+z)^2/H(z)$ (Bahcall & Peebles, 1969).

1.3 Previous Works on DLA Kinematics

Pontzen et al. (2008) for example underproduced high velocity width DLA systems, relative to observations, in their series of hydrodynamic simulations of individual galaxy halos. This was despite reproducing the observed column density distribution function and metallicity distribution of DLAs. However, their method of building global distributions by convolving a limited sample by the DLA cross section

weighted halo mass function may have produced biased results. Indeed, examining single halos in isolation neglects the projected alignment of multiple regions of neutral gas that can contribute to the same DLA profile.

Tescari et al. (2009), on the other hand, used full cosmological simulations with a variety of galactic wind models to investigate the properties of DLAs. Their analysis also failed to produce high velocity width systems and overproduced low v_{90} values. They attributed this behavior to poor enrichment of the Inter-Galactic Medium (IGM), with metals being predominantly found in clumps. But it is not clear how their sightline statistics, targeted a priori on the center of the most massive halos in the simulation volume, can be meaningfully compared with observations. Of course, QSO sightlines intersect structure (unassociated with the quasar itself) randomly along the observer's line of sight.

Mstreatments of damped Lyman-α kinematic analysis were explicitly highlighted by Prochaska & Wolfe (2010). For example, Hong et al. (2010) mistakenly excluded DLA spectra based on the saturation of a single metal line rather than considering all available low ion metal transitions.

Cen (2012) can be credited as the first to have used hydrodynamic simulations to produce a DLA VWD that agreed well with observations. They bracketed observational data from Prochaska (2003) using two cosmological volumes, centered on a cluster and on a void respectively. However, this agreement does not hold in comparison with the more recent results of N13 at low velocity widths. That said, as Cen (2012) over smooth their intrinsic optical depth profiles, rather than convolve with an instrumental profile (see section 3.5), we cannot rule out the underlying success of their simulations.

Despite being drawn from overlapping samples of DLA sightlines, the Prochaska (2003) and N13 VWDs differ considerably at the low v_{90} end for two reasons (Barnes & Haehnelt, 2014; Bird et al., 2015). Firstly, N13 exclusively use very high resolution spectra, enabling them to identify smaller velocity width systems than could have been resolved by the older, lower resolution sample of spectra. Secondly, N13 used a more representative sample of DLA sightlines by not including lines specifically targeted as being metal rich – these high metallicity spectra were biased towards

higher velocity widths than a truly blind sample.

Most recently, Bird et al. (2015) (hereafter B15) matched N13's DLA VWD substantially better than previous work. They attribute the success of their simulations to their careful ionisation modelling and their implementation of strong outflows. Driven by supernovae feedback, strong outflows suppress the formation of DLA systems, especially in smaller halos. B15's self-shielding model was implemented live in the simulation itself rather than in post-processing, using the photoionisation fitting formulae of Rahmati et al. (2013a), having corrected for the slightly higher ionisation potential of Si II than H I.

1.4 Thesis Outline

In this work we pay special attention to how v_{90} is calculated and thoroughly investigate the dependencies of the DLA VWD in order to understand the true origin of sightline kinematics. Later, we isolate DLA host halo systems, and comment on the tenuous connection between v_{90} and the underlying host halo properties.

The layout of this thesis is as follows:- In chapter 2, we overview the suite of cosmological SPH simulations used in this work (2.1) and describe our post-processing calculation of the hydrogen (2.2) and metal ionisation states (2.3). We also detail how we generated artificial transmission spectra (2.4), calculated sightline kinematics (2.5), targeted DLA sightlines (2.6) and associated absorption with halo/galaxy structures (2.7) in this section. In chapter 3.2 we present the results of our analysis, including the predicted VWD (3.1) and its dependencies on our implementation (3.1 and 3.3). We comment on the smallest possible velocity widths that can be resolved (3.4) and the importance of projection effects (3.5) before quantifying the physical origin of sightline kinematics in section 3.6 using a novel approach. We then explore the nature of our simulated DLA host systems in section 3.7. The implications of our results are discussed as they arise. We summarize our main conclusions in chapter 5. Finally, we have attached our derivation of unresolved SPH particle turbulence in appendix A.

We refer to Altay et al. (2013) for a study of the impact of different physical

processes on the abundance statistics and Column Density Distribution Function (CDDF) of DLAs and LLSs for the same suite of simulations used in this work, analysed using the same post-processing calculation. The focus of our study lies squarely on the velocity widths of DLA systems.

Chapter 2

Methods

2.1 Simulations

This work is based on the OWLS project suite of cosmological simulations (Schaye et al., 2010). The OWLS project was performed with a modified version of the SPH Tree-PM code GADGET (last described in Springel, 2005), including: sub-grid models for star formation (Schaye & Dalla Vecchia, 2008), galactic winds (Dalla Vecchia & Schaye, 2008, 2012), chemodynamics (Wiersma, Schaye & Smith, 2009) and element-by-element cooling for 11 species whose abundance is traced individually within each baryonic particle (Wiersma et al., 2009). Gas in the ISM at densities above $n_{\rm H}^* = 0.1$ cm^{-3} is assumed to be multi-phase and starforming. This is modelled by moving these particles onto a polytropic Equation of State (EoS) of the form $P = P_*(n_{\rm H}/n_{\rm H}^*)^{4/3}$ and converting EoS particles into collisionless star particles probabilistically. The star formation rate of each EoS particle is determined by rewriting the observed Kennicutt-Schmidt star formation law as a pressure law (Schaye & Dalla Vecchia, 2008).

The majority of this work will focus on the OWLS reference model (REF) at redshift $z = 3$ run with a periodic box size of $L = 25$ comoving Mpc/h, containing 512^3 SPH particles and as many dark matter particles. The baryonic and dark matter particle masses are $m_{\rm b} = 1.4 \times 10^6 M_\odot$/h and $m_{\rm dm} = 6.3 \times 10^6 M_\odot$/h respectively. The equivalent Plummer gravitational softening length is $\epsilon = 1.95$ comoving kpc/h. REF assumes a ΛCDM cosmological model with cosmological parameters best fit to

the Wilkinson Microwave Anisotropy Probe (WMAP) 3-year results: { $\Omega_{\rm m}$, $\Omega_{\rm b}$, Ω_{λ}, σ_8, $n_{\rm s}$, h, } = {0.238, 0.0418, 0.762, 0.74, 0.951, 0.73} (Spergel et al., 2007). The primordial helium mass fraction is assumed to be 0.248.

The great advantage of these simulations is that they have been repeated systematically many times: varying the subgrid model of the baryonic physics, as well as the cosmology, resolution and box size. We make use of this highly effective strategy to isolate the effects of individual physical mechanisms on the inferred kinematics of DLA systems. Rather than describing here all the model variations analysed in this work, we shall simply highlight the relevent differences between them and REF as we encounter them in our results (see section 3.3). For a full, detailed description of the OWLS project and the suite of variations, see Schaye et al. (2010) and citations thereof.

As these aspects are crucial to the discussion, we highlight that the radiative cooling rates, along with photo-heating due to a spatially uniform but time varying UV/X-ray background radiation field, are calculated in OWLS element-by-element using the photoionisation package CLOUDY version 7.02 (most recently described in Ferland et al., 2013) as detailed in Wiersma, Schaye & Smith (2009). These calculations assume independent photo/collisional ionisation equilibrium for each particle, in the optically thin limit. All of the OWLS models which include a photoionising Ultraviolet Background (UVB) use the Haardt & Madau (2001) (hereafter HM01) model.

2.2 Hydrogen Self-Shielding

When calculating the ionisation state of hydrogen, it is important to break the optically thin approximation and account for the self-shielding of the cold, dense, neutral gas that comprises DLAs and LLSs. We perform this calculation in post-processing using the accurate 3D radiative transfer, reverse ray-tracing code URCHIN (Altay & Theuns, 2013).

In this code, an initial neutral fraction is calculated for each gas particle using an analytic equilibrium solution, assuming a uniform, frequency dependant, optically

thin photoionisation rate ($\Gamma^{\rm thin}$) derived from the UVB radiation field. Rays of physical length $l_{\rm ray} = 100$ kpc are then sampled in $N_{\rm ray} = 12$ directions around each gas particle to calculate the optical depth τ perceived at its location. This value is then used to relate each gas particle's shielded photoionisation rate to the optically thin value, $\Gamma^{\rm shld} = \Gamma^{\rm thin}\exp(-\tau)$. The particle's ionisation state is then updated. This procedure is iterated until convergence is reached. Most gas particles occupy regions that are either optically thin ($\tau << 1$), or optically thick ($\tau >> 1$) where the scheme converges quickly; URCHIN hence focuses the majority of the computational effort on photoionisation fronts, where it is needed. The above values of $N_{\rm ray}$ and $l_{\rm ray}$ lead to converged results for the $z = 3$ CDDF in the simulations used in this work (Altay et al., 2013).

Ionizing photons from recombinations are assumed to immediately escape for particles with $\tau < 1$ (so called Case A) and are absorbed on the spot for particles with $\tau > 1$ (Case B). This approximation results in a steeper transition between the optically thin and optically thick gas than found by Rahmati et al. (2013a), who explicitly follow recombination radiation in OWLS using a completely different radiative transfer code TRAPHIC (Pawlik & Schaye, 2008). However, their overall results regarding H I column density statistics agree very well with the results of the URCHIN code (see their appendix C3, and Altay et al., 2011).

Because OWLS gas particles experience the unattenuated HM01 UVB when calculating their heating and cooling rates in the simulations, many particles are artificially photo-heated. To compensate for this, we set a temperature ceiling of $T_{\rm shld} = 10^4$ K for particles that become self-shielded ($\tau > 1$). Furthermore, the temperature stored for OWLS gas particles on the polytropic equation of state is simply a function of the local density. We set the temperature of these particles to $T_{\rm EoS} = 10^4$ K – a value typical of the warm neutral phase of the ISM. Altay et al. (2013) found that using lower values of $T_{\rm EoS}$ did not affect their results.

Note that the cooling rate of gas particles feeds into the OWLS hydrodynamics solver; hence the modifications we have made to particle temperatures above are not self-consistent. That said, Pontzen et al. (2008) found that using a live, local UVB attenuation approximation in addittion to their post-processing radiative transfer

implementation only had a minor effect on their results. Similarly B15, who implemented a self-shielding model in their simulation itself, found that correcting for self-shielding post-processing instead had a negligible effect on their DLA VWD. However, we cannot infer that our results would experience the same self consistency. Implementing a full radiative transfer prescription live within cosmological simulations such as OWLS would be very computationally expensive on the fly.

Based on the observations by Blitz & Rosolowsky (2006), we apply an empirical relation to calculate the molecular hydrogen mass fraction for particles on the OWLS starforming equation of state. The molecular fraction is given by a power law scaling to the particle pressure and should be considered an upper limit to how much H_2 is present within DLA hosts. This relationship was used to remove H_2 from the hydrogen density field before the radiative transfer calculation (see sections 2.4 and 5.1 of Altay et al. (2013) for further details).

At $z = 3$, the UVB that pervades the Universe is mostly uniform. However, close to the sources of the photoionizing radiation, such as clusters of young stars and accreting super massive black holes, there exist proximity regions where the radiation field is stronger than the UVB. As these point-like sources (on cosmological scales) cluster in regions of high gas density, it is reasonable to expect that their proximity regions will affect the abundance and spatial distribution of H I gas and hence the properties of DLA systems. Indeed, Rahmati et al. (2013b) found that local stellar radiation on the OWLS reference model lowered the abundance of high column density H I absorbers. However their results were very sensitive to the assumptions made about the ISM above $N_{\rm HI} = 10^{21}$ cm^{-2}. This is not surprising as modelling radiation transport through the ISM involves scales which are many orders of magnitude smaller than what current cosmological simulations can resolve. Because the predicted abundance of DLA is already too low for the OWLS reference simulation (see section 2.6), and because star formation is already modelled using a subgrid recipe, we have neglected the addition of local radiation sources in this work.

2.3 Metal Ionization

At DLA column densities, H I is highly saturated over a large velocity interval, making it impossible to recover kinematic information from this ion directly. Therefore, it is necessary to measure the kinematics of DLAs from associated, relatively narrow, low ionisation metal lines. For this purpose, we haven chosen to investigate Si II as our representative low-ionisation metal absorber. This is the most common ion used in the dataset of 100 DLAs analysed by N13.

The actual choice of low ionisation species should be inconsequential for our analysis, provided that the ion's Ionisation Potentials (IPs) is similar to that of H I. As shown by e.g. Prochaska (2003) (see their Figure 1), the apparent optical depth profiles for low-ion metals such as Si II and Fe II follow each other very closely; implying that the metal abundance ratios within DLA systems are more-or-less constant along the velocity space line of sight. This is expected as low ion metals are thought to have a common origin and to be well mixed throughout the neutral medium.

On the other hand, high ionisation transition lines, associated with the same DLA systems, exhibit very different velocity structures as a consequence of their different origins. In practice at least one low-ion metal transition satisfying both strength and non-saturation criteria necessary for kinematic investigation has been found in every high resolution DLA examined to date, (Prochaska & Wolfe, 2010). This is reassuring as some of our sightlines exhibit very low column densities in Si II, with corresponding transmission profiles that would be unobservable in reality.

We assume an ionisation fraction of Si II perfectly coupled to that of atomic hydrogen:

$$n_{\rm SiII}/n_{\rm Si} = n_{\rm HI}/n_{\rm H} \ , \tag{2.3.1}$$

This is in line with previous authors (e.g. Pontzen et al., 2008; Cen, 2012) and incorporates the assumption that low ionisation metal absorbers trace the kinematics of the neutral hydrogen gas. However, this coupling neglects the difference in IP of Si II (16.3eV) and H I (13.6eV), which may allow the metal ion to persist in lower density environments than H I. Hence, the Si II regions in our simulations may be

somewhat too compact. We consider this further in section 3.2.7.

2.4 Artificial Transmission Spectra

In order to generate apparent optical depth profiles, we followed the procedure of Theuns et al. (1998), appendix A4, implementing a modified version of the artificial transmission spectra code SpecWizard.[1] All atomic data are taken from Morton (2003).

Given a coordinate and orientation, SpecWizard first extracts the intersected gas particles along a 1D line of sight. The code then calculates a true SPH projection of particle properties along the sightline in real space, weighted by the integrated particle kernel and number density of the given ion species. For this purpose, we implemented a Gaussian particle kernel, truncated at each particle's smoothing length, having the same amplitude as the cubic spline kernel used in the simulation.[2] This kernel allowed us to quickly integrate particle properties across the real space pixels exactly, capturing all the available small scale structure, rather than taking a central value for each pixel. Given the high spatial resolution implemented, neither using a central pixel value nor implementing the simulation kernel instead affected our results.

In a second step, SpecWizard calculates an *intrinsic* optical depth profile (τ) in redshift space, treating each real space pixel as a slab absorber. Both the peculiar velocity and Hubble velocity of each pixel are taken into account. The Doppler broadening parameter b for each absorber is calculated by adding in quadrature the thermal component $b_{\rm therm}$ to a turbulent, kinematic component $b_{\rm turb}$:

$$b_{\rm therm} = \sqrt{\frac{2k_{\rm B}T}{m_{\rm ion}}} \ , \tag{2.4.1a}$$

$$b_{\rm turb} = \sqrt{2}\sigma_{\rm turb} \ , \tag{2.4.1b}$$

$$b = \sqrt{b_{\rm turb}^2 + b_{\rm therm}^2} \ , \tag{2.4.1c}$$

[1] Available on request.

[2] See Altay & Theuns (2013) for a derivation.

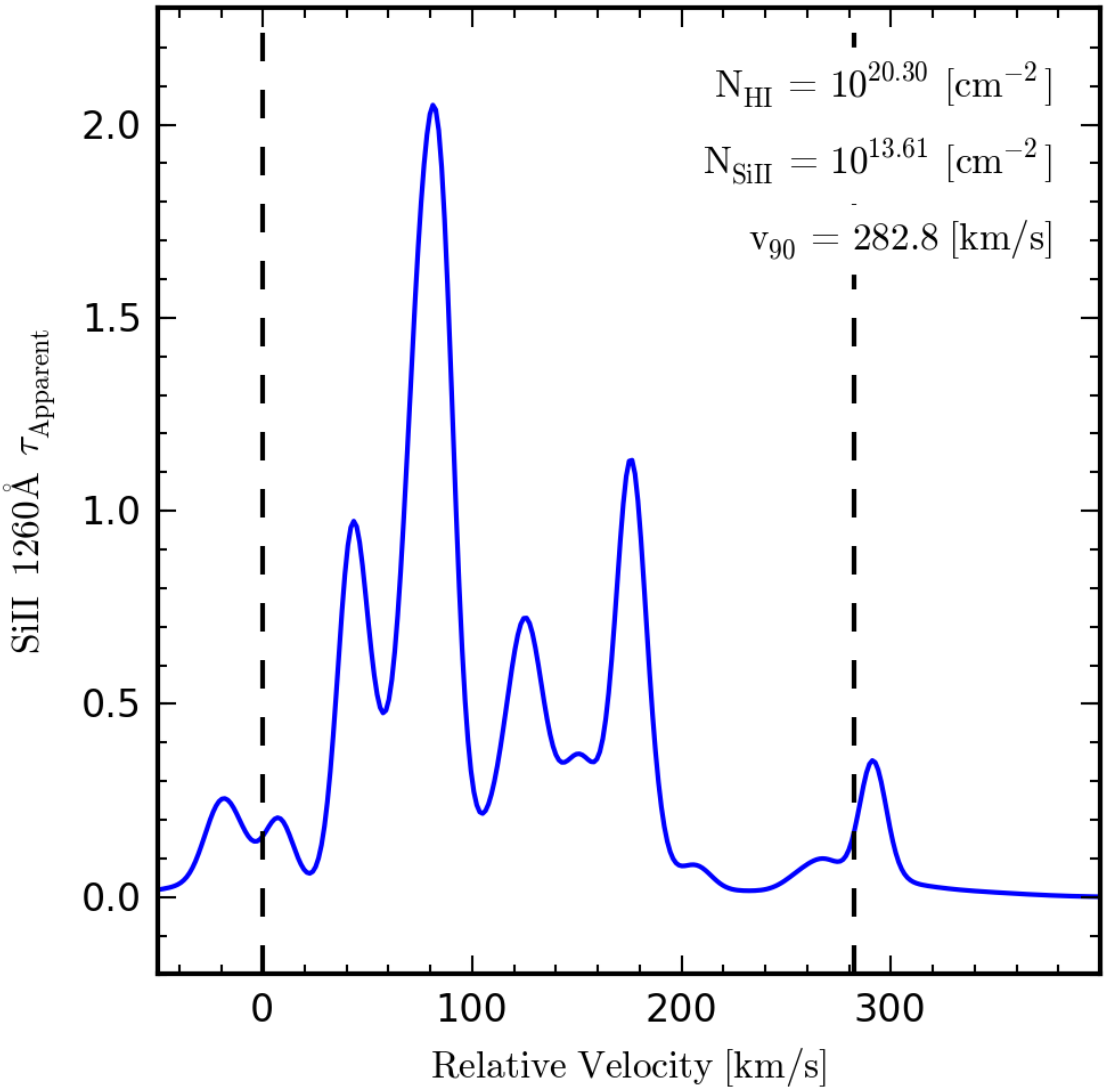

Figure 2.1: An example simulated Si II 1260Å apparent optical depth profile, associated with a redshift $z = 3$ DLA, observed using a Gaussian instrument of FWHM 8 km/s. We do not add artificial noise for display purposes. The atomic hydrogen column density is very close to the DLA threshold, $N_{\rm HI} = 10^{20.3}$ cm^{-2} and the Si II column density is $N_{\rm SiII} = 10^{13.61}$ cm^{-2}. The profile has been smoothed using an 8 km/s top hat and shifted to the left edge of the 282.8 km/s velocity width interval – as indicated by the dashed lines. A complex kinematic structure along the line of sight can clearly be distinguished.

where T is particle temperature, $k_{\rm B}$ is the Boltzmann's constant, $m_{\rm ion}$ is the mass of the absorbing ion species and $\sigma_{\rm turb}$ characterizes the one dimensional unresolved turbulent velocity dispersion of the gas within each absorber. $\sigma_{\rm turb}$ is defined such that the total internal energy of each particle is conserved (see appendix A) and is projected along sightlines in the same manner as other real-space particle properties.

We did not include a convolution with the ions' natural Lorenzian in order to produce a Voigt profile for each absorber. Although this transformation is essential in producing realistic highly saturated optical depth features such as damped Lyman-α (where the tail of the Lorenzian dominates the profile), it is not important in producing the low ionisation metal absorption profiles considered in this work. See for example figure 2.1. We did not perform Voigt profile fitting on our optical depth profiles; we calculated the ion column densities directly for each of our lines of sight.

To emulate observed spectra, we convolved all our transmitted intensity spectra $Tr \in [0, 1]$ with a Gaussian instrumental profile G, allowing us to calculate the apparent optical depth $\tau_{\rm app}$:

$$Tr = \exp\left(-\tau\right) \ , \tag{2.4.2a}$$

$$\tau_{\rm app} = -\ln\left(Tr * G\right) \ , \tag{2.4.2b}$$

We used a spectral bin size of 1.4 km/s and instrumental FWHM of 8 km/s, consistent with the Keck, High Resolution Echelle Spectrometer (HIRES, Vogt et al., 1994) observations of N13.[3]

It is important to point out that even (state of the art) 8 km/s FWHM observations are not truly "resolved" with respect to the underlying optical depth profile of metal ions. For example, (relatively light) Si II at 10^4 K has a Doppler parameter of 2.43 km/s, with a corresponding FWHM of 4.05 km/s – appreciably narrower than the instrumental profile. Strictly speaking, current high resolution spectra "distinguish" multiple kinematic components in (often complex) apparent optical depth profiles, for low-ion metals. The significance of this distinction will become evident later when we consider $\tau_{\rm app}$ profiles close to saturation in section 3.2.5.

[3]In practice some of these observations achieved a smaller FWHM resolution.

2.5 Sightline Kinematics

The velocity width or v_{90} statistic was originally defined in Prochaska & Wolfe (1997) as a measure of the velocity extent of low-ion metal lines associated with damped Lyman-α absorption. Formally, v_{90} is the velocity interval containing the innermost 90% of the total integrated apparent optical depth of a low-ion metal transition, having convolved the $\tau_{\rm app}$ profile with a top hat smoothing function. This smoothing is done to prevent differences in spectral resolution from affecting the velocity width measurements. In line with N13, we smooth all our $\tau_{\rm app}$ profiles using an 8 km/s top hat.

The v_{90} interval is found by stepping in pixel-by-pixel from each side of the smoothed $\tau_{\rm app}$ profile until the outermost 5% has been excluded. The reasoning behind this method is that small, outlying absorption features should not skew the velocity width measurement towards high values. Note that extended metal absorbers may contain considerable kinematic structure. Explicitly:

$$\tau_{\rm final} = (\tau_{\rm app} * \mathrm{TopHat}) \ , \tag{2.5.1a}$$

$$\mathrm{Tot} = \int_{-\infty}^{+\infty} \tau_{\rm final}(\mathrm{v}) d\mathrm{v} \ , \tag{2.5.1b}$$

$$\int_{\mathrm{v_{hi}}}^{+\infty} \tau_{\rm final}(\mathrm{v}) d\mathrm{v} = \int_{-\infty}^{\mathrm{v_{lo}}} \tau_{\rm final}(\mathrm{v}) d\mathrm{v} = 0.05\mathrm{Tot} \ , \tag{2.5.1c}$$

$$\mathrm{v_{90}} = \mathrm{v_{hi}} - \mathrm{v_{lo}} \ , \tag{2.5.1d}$$

Where in practice, the integration limits $-\infty$ and $+\infty$ are replaced by the maximum velocity interval over which the optical depth is attributed to the same low-ion metal transition i.e. is unblended with any other transitions. As we calculated all of the allowed Si II transitions separately, we faced no ambiguity in attributing absorption to a given transition.

We chose to step in our velocity width window from 1250 km/s either side of the peak Si II optical depth. This interval corresponded to the maximum relative velocity between any two absorbers in our 25 Mpc/h reference simulation at $z = 3$, i.e. half the Hubble flow across the volume ($\mathrm{v_{box}} = 2499.53$ km/s given a WMAP3 cosmology). In order to prevent our periodic simulation boundaries from erroneously separating absorption components, we singled out sightlines where v_{90} exceeded

$v_{box}/2$. For these sightlines, we cycled the optical depth profile in velocity space and selected the minimum velocity width obtained as our chosen measurement. This method did not remove all velocity widths above $v_{box}/2$ as some sightlines intersected multiple strong absorbers, separated significantly in velocity space. We discuss in section 3.5 whether associating such absorption with the same DLA system is justified. As the box periodicity was visibly imprinted via low mode density fluctuations within our reference simulation, we excluded (rare) sightlines of velocity widths exceeding $v_{box}/4 = 625$ km/s from the majority of our analysis. Note that the largest measured value of v_{90} by N13 is 484 km/s.

We choose the strongest, unsaturated Si II transition to determine the final v_{90} value for each sightline. Unsaturated transitions satisfy the requirement that the apparent transmission exceeded 0.1 over the entire profile; i.e. $\max(\tau_{app}) < -\ln(0.1) = 2.30$, in line with N13. We did not implement a minimum absorption strength threshold in choosing a Si II transition, as numerically our Si II spectra were not affected by detection limits. As a consequence, Si II would have been undetectable for some of our DLA sightlines. We show that this does not effect our results in sections 3.2.3 and 3.2.4. We chose not add any noise to our artificial transmission spectra.

2.6 Targeting DLAs

In order to efficiently identify sightline coordinates exceeding N_{DLA}, we first projected all the gas particles in the simulation onto a H I column density grid, integrating our Gaussian kernel exactly across each of $16,384^2$ pixels – corresponding to a pixel separation of 1.53 comoving kpc/h. The calculated column density for each pixel (N_{2D}) is in fact an average over its projected area. As the one dimensional column density for sightlines within single pixels sometimes varied by up to 1 dex, we randomly projected sightlines through a mask satisfying $N_{2D}(\mathrm{HI}) \geq 10^{19}$ cm^{-2}

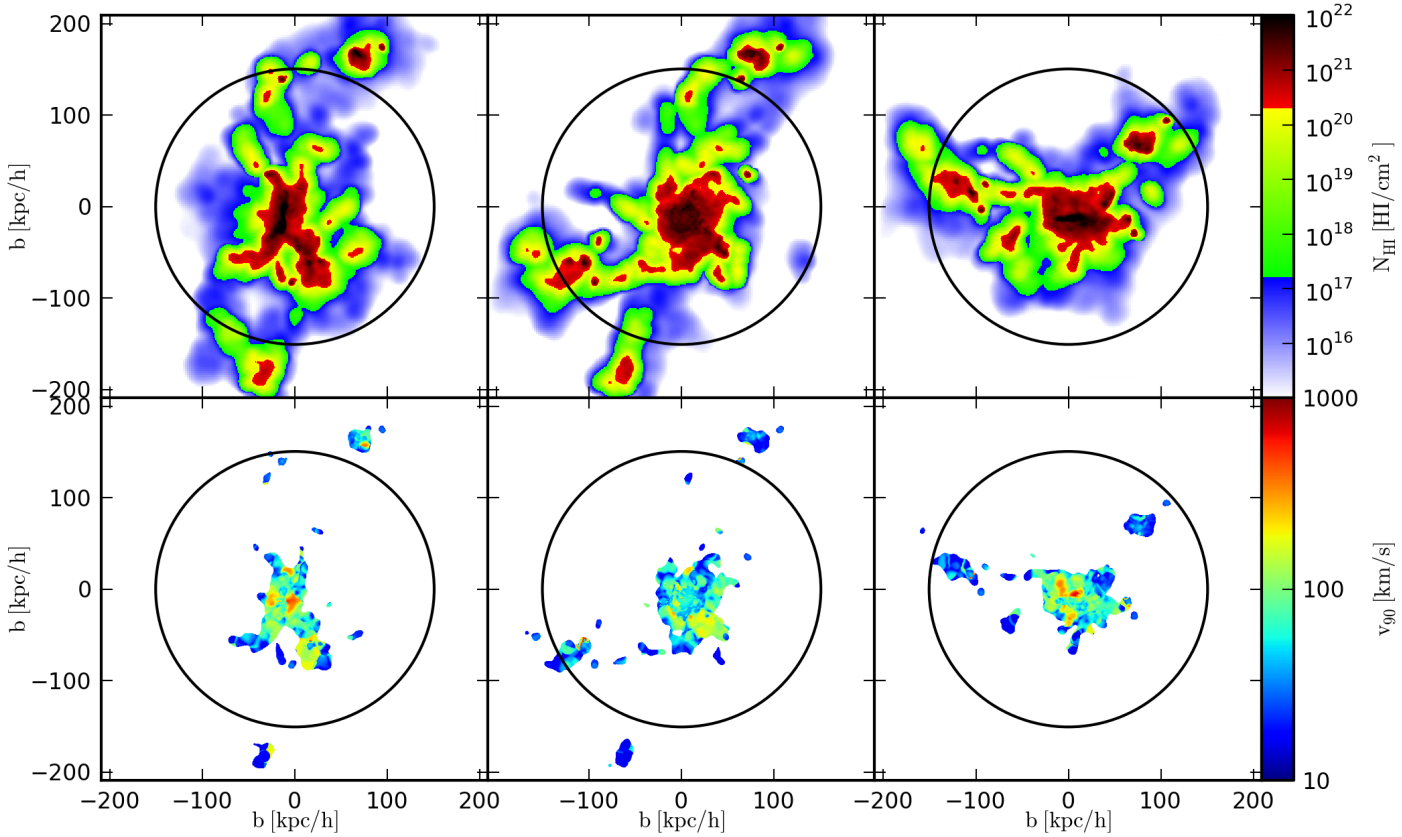

Figure 2.2: Top: three orthogonal projections of the H I column density for an isolated $10^{11.5} M_\odot$ mass Friends-of-Friends halo at $z = 3$. Impact parameter b is given in comoving coordinates. The halo's virial radius (151 kpc/h) is indicated by the black circle. The three ascending colorbars correspond to Lyman-α forest, LLS and DLA absorption (Pontzen et al., 2008). Bottom: the corresponding maps of DLA velocity widths. The v_{90} statistic appears stochastic, varying rapidly on small scales, yielding values in the range 15.4 km/s to 810 km/s. The median velocity width for this halo is $50.4^{+75.6}_{-30.8}$ km/s.

and retained only those where $N_{\rm 1D} \geq N_{\rm DLA}$. [4] This method allowed us to efficiently extract DLA coordinates whilst remaining sensitive to the random intersection of structure by unassociated background QSOs. This method also makes no prior assumption that DLAs originate from single independent halo structures, nor artificially suppresses contributions by the IGM and low mass halos to H I column densities and Si II transmission spectra.

One caveat of this method is that structures with large DLA cross sections are probed many times; whereas it is very rare observationally to find a foreground galaxy probed by multiple QSOs. However, we do not expect 1D properties such as v_{90} to be constant across complex halo/galaxy structures in our simulations nor in the real Universe. We found that generating $10,080$ random DLA sightlines was sufficient to produce converged kinematic results.

Another caveat of this method is that aligned but discrete neutral gas structures may be identified as DLA-hosting due to their combined H I column densities along the line of sight i.e. by probing multiple LLSs. Furthermore, we did not break up sightlines having intersected more than one DLA-hosting structure. However, it is important to point out that it is not always possible to distinguish such absorbers from "true" independent DLA, commonly envisioned as being hosted by single galaxy/halo structures. We shall expand on this topic, and the influence of projection effects on our kinematic results, in section 3.5.

The line density of DLAs is defined as the number of absorption lines n per unit absorption distance dn/dX, where dX is related to the redshift path dz as $dX/dz = H_0(1+z)^2/H(z)$ (Bahcall & Peebles, 1969). Each pixel of our H I column density grid corresponds to a line of sight transversing an absorption distance of $\Delta X = H_0(1+z)^2 L_{\rm box} c^{-1}$, where $L_{\rm box}$ is the comoving box size. Hence the total absorption distance is given by $16,384^2 \times \Delta X$ and the number of DLA lines equals the number of pixels exceeding $N_{\rm DLA}$. For our $L_{\rm box} = 25$ comoving Mpc/h reference simulation at $z = 3$, $\Delta X = \frac{4}{30}$ and $dn/dX = 0.0359$. Hence, our reference simulation underpredicts the

[4] We checked that the 2D and 1D projection methods produced converged H I CDDFs by projecting 10^6 truly-random sightlines through the reference simulation along the z-axis (without calculating their spectra).

abundance of DLA systems by a factor of 2.02, relative to an observed line density of $dn/dX = 0.0724$. We obtained this value from the systematically corrected sample of 583 Sloan Digital Sky Survey (SDSS) III DLAs between redshifts 2.9 and 3.2, presented in Noterdaeme et al. (2012), assuming a (reference) WMAP3 cosmology.

Throughout this work, we frequently refer to the DLA Velocity Width Distribution . Formally, we define the DLA VWD to be the number of DLA features per unit absorption distance X per velocity width (v_{90}): $\frac{d^2n}{dX dv_{90}}$.

2.7 Identifying and Isolating Halo Structure

To identify physical structures within each simulation volume, a group catalogue was first calculated using the standard Friends-of-Friends algorithm of Davis et al. (1985) run on the dark matter particles, with the baryonic particles linked to their nearest neighboring dark matter particle. We shall refer to these structures as Friends-of-Friends halos. Gravitationally bound sub-structures within each Friends-of-Friends halo were then identified using the Subfind algorithm (Springel et al., 2001; Dolag et al., 2009). We shall refer to these structures as Subhalo galaxies. For every sightline, we recorded the H I and Si II column densities contributed by each Friends-of-Friends halo and Subhalo galaxy intersected, allowing us to associate absorption with the underlying gas structures.

Further to our targeting of random DLA sightlines in the previous section, we also isolated 1000 Friends-of-Friends halos from the reference simulation and projected their H I density fields, along three orthogonal directions, onto individual 2D column density grids. The grid resolution was set below 0.1 comoving kpc/h per pixel side. We then projected sightlines through the center of each pixel satisfying $N_{2D}(\mathrm{HI}) \geq 10^{19}$ cm^{-2} and retained only those where $N_{1D} \geq N_{DLA}$. This method allowed us to build kinematic images of DLA host halos (see figure 2.2) and to qualitatively examine the connection between velocity width and some DLA host halo properties in section 3.7. We found that the chosen resolution level was sufficient to produce converged N_{HI} and v_{90} distributions.

The chosen isolated halos were required to contain at least 50 gas particles, be

DLA hosts and to have well defined[5] R_{200} radii, i.e. the spherical radius within which the density of the halo exceeds 200 times the critical density. We shall refer to R_{200} interchangeably as the virial radius, as per common practice. We analysed all 695 reference simulation halos with mass $M_{\rm FoF} > 10^{10.5} M_{\odot}$ at $z = 3$ and 305 further halos equally spread over $\log(M_{\rm FoF})$ space.

[5] R_{200} is not well defined for halos that do not exceed 200 times the critical density, nor for those with (very) close neighbouring halos.

Chapter 3

Results

3.1 Velocity Width Distribution

On figure 3.1, we show the VWD for $10,080$ randomly targeted DLA sightlines through the $z = 3$ reference simulation, normalised to the simulation DLA line density of $dn/dX = 0.0359$. We compare our profile to N13's sample of 100 DLAs, of mean redshift $z = 3$, whose observational procedure we have emulated as closely as possible. We estimate the uncertainty on our profile by bootstrapping 10^5 subsamples of 100 sightlines and show the 68^{th} and 95^{th} percentile bands. The uncertainties drop off the plot where they correspond to zero DLA systems of a given velocity width being observed. For comparison, we also show the "DEF" v_{90} distribution of B15, which we reproduced from their figure 2.

As it can be seen, the simulation overproduces low velocity width systems below $v_{90} = 10^{1.4} \simeq 25$ km/s. This corresponds to 45.4% of the total number of sightlines. Our median velocity width is $26.6^{+110.6}_{-8.4}$ km/s,[1] substantially lower that the observed value of $70.0^{+78.5}_{-42.0}$ km/s. However, we also readily produce DLAs with high velocity widths – a success for cosmological, hydrodynamical simulations. Note that if we were to retrospectively reweight the simulated VWD to match the observed relative abundance of sightlines above(below) 32 km/s, the profile would be shifted up(down) by a factor of 1.88(2.76) and would reproduce the observational VWD of N13 within

[1]Note that all errors given in the text indicate the corresponding 16^{th} to 84^{th} percentile bands.

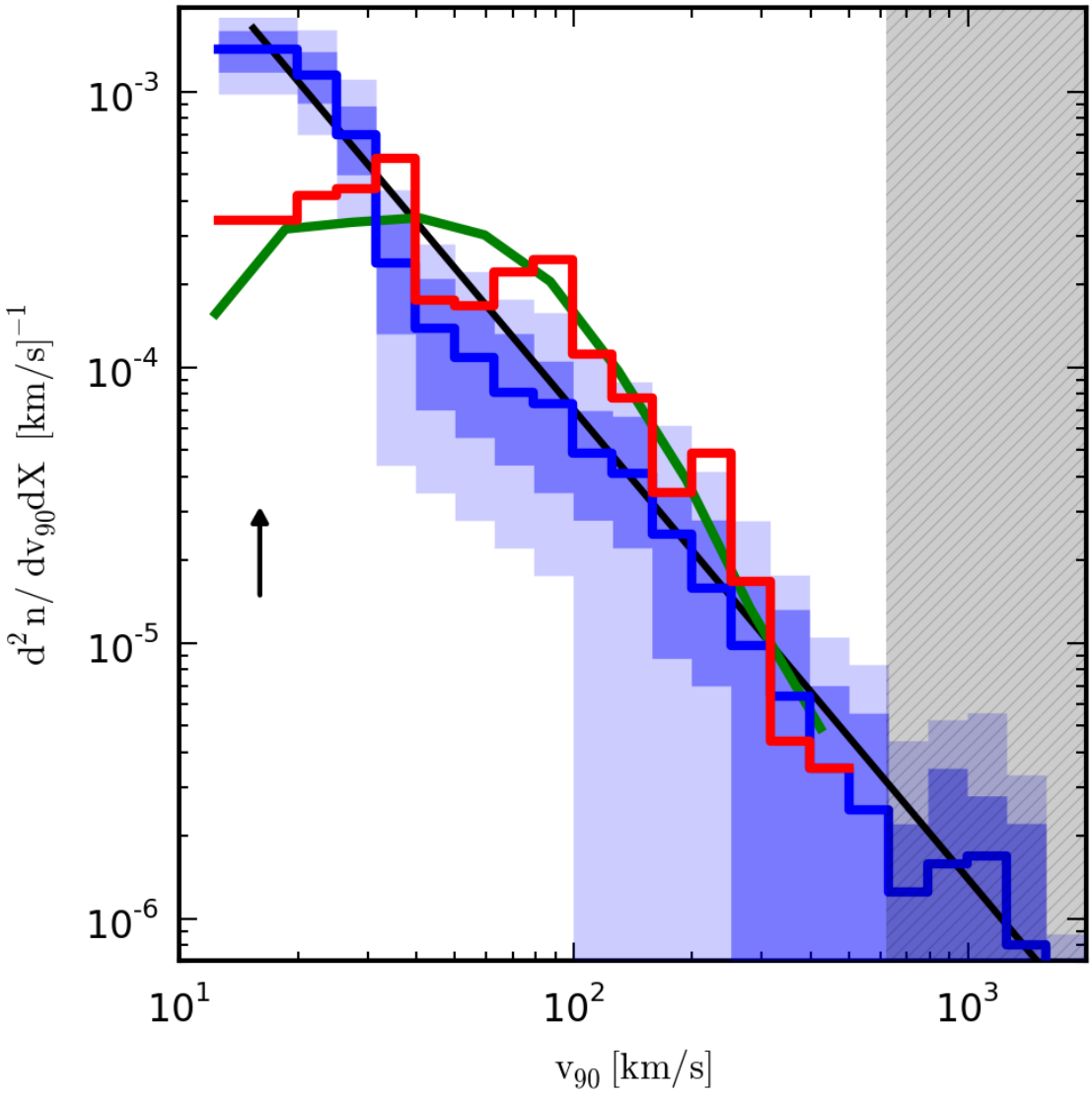

Figure 3.1: The DLA Velocity Width Distribution or number of DLAs per velocity width, per absorption distance. The 100 observations by Neeleman et al. (2013) are shown in red. The OWLS reference model at $z = 3$ is shown in blue, with bootstrapped $68^{\text{th}}(95^{\text{th}})$ percentiles for sub-samples of 100 DLAs, shown by the dark(light) shaded regions. We have reproduced the reference VWD from Bird et al. (2015)'s figure 2 in green. All profiles are normalised using a DLA line density of $dn/dX = 0.0359$. Renormalising to an observed DLA line density of $dn/dX = 0.0724$ (Noterdaeme et al., 2012) would shift the profiles up by the black arrow. The simulation VWD can be fit by a power law of slope $-1.70^{+0.01}_{-0.01}$, as shown by the black line. Velocity widths greater than 625 km/s, have been shaded out (see text). The simulation produces high velocity width DLAs but overproduces systems with $v_{90} < 25$ km/s, relative to N13.

the statistical uncertainty.

Demonstrating neither a turn-over at low velocity widths, nor a peak around 80 km/s (potentially seen in N13's observations), our full VWD is readily fit by a power law of slope $-1.70^{+0.01}_{-0.01}$. We calculated this slope by performing a least-squared fit on the cumulative v_{90} probability function, for 10^5 bootstrapped subsamples of 10,080 sightlines, to avoid any dependencies on binning and to reduce the impact of outliers respectively. This power law departs from N13's log-normal fit to the full VWD (a functional form which admittedly describes B15's profile very nicely).

3.2 Implementation Variations

On figure 3.2, we show the VWD for several variations to our reference analysis (always shown in blue), as described in the following sections.

3.2.1 Redshift Evolution

On the top-left panel of figure 3.2, the redshift evolution of the VWD for three simulation outputs, $z \in \{2, 3, 4\}$ is shown. The simulated line densities of DLAs are $dn/dX = 0.0384$ at $z = 4$, 0.0359 at $z = 3$ and 0.0301 at $z = 2$, a decline due to the increasing amplitude of the HM01 photoionising UVB. This UVB evolution manifests in fewer low v_{90} sightlines at $z = 2$, due to e.g. small isolated clouds of neutral gas. Apart from this difference, we find negligible redshift evolution of the VWD. N13 did not find any significant redshift evolution either in their observational sample of 100 DLAs spanning the interval $z \in [1.66, 5.06]$. We only consider the simulation output at $z = 3$ for the remainder of this work – the mean redshift of the N13 sample.

3.2.2 Metal Diffusion

In the OWLS simulations, there is no subgrid mechanism for diffusion of metals between gas particles. As a consequence, the simulation metal distribution is not necessarily smooth. It is known that enriched SPH particles sometimes find them-

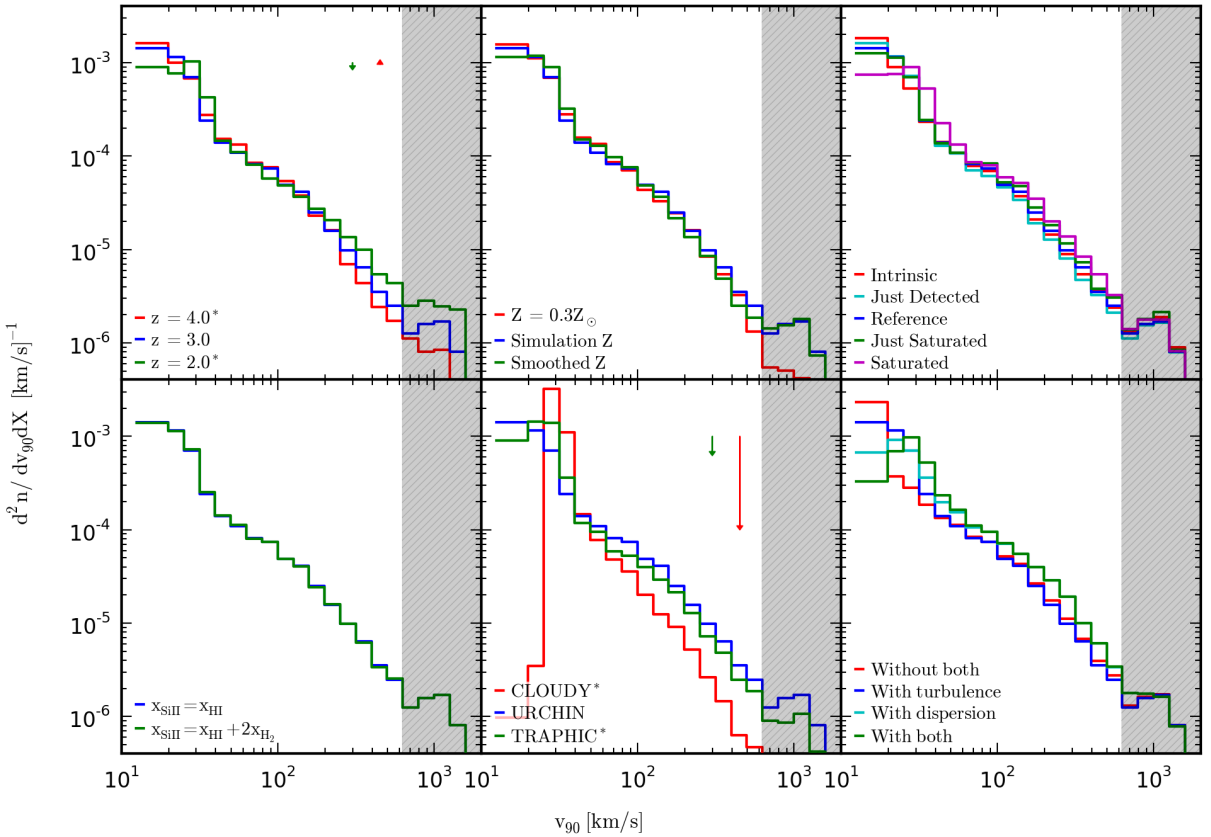

Figure 3.2: The DLA VWDs for several variations to the reference simulation (blue) as detailed in the text. Each distribution is normalised to the reference line density, the colored arrows correspond to a shift to the true line densities of some variations (indicated: *). Top left: redshift evolution. Top middle: changing the particle metallicity. Top right: demonstrating saturation bias. Bottom left: bracketing the treatment of molecular hydrogen. Bottom middle: implementing photoionization fitting formulae (TRAPHIC) or neglecting self-shielding entirely (CLOUDY) in place of full radiative transfer. Bottom right: kinematic implementation, with/out adding unresolved turbulence and SPH particle velocity dispersion to absorbers' Doppler parameters.

selves isolated in otherwise metal-poor regions of space, having being kicked out of dense star-forming regions by supernovae feedback. Such particles could potentially produce discrete, outlying absorption features in our DLA spectra. We tested the influence of metal transport on the VWD by performing our analysis again using a metallicity that was smoothed over each particles' 48 nearest neighbors. Reassuringly, this calculation had little effect on the DLA VWD, as demonstrated in the top-middle panel of figure 3.2. The only difference is an increased broadening of single component sightlines, with $v_{90} < 20$ km/s, by a few km/s.

3.2.3 Metal Distribution

The transmission spectra of low-ion metals, associated with DLAs, exhibit diverse profile shapes and are often complex. However it is not obvious whether this effect is dominated by fluctuations in the metallicity, temperature or the ionisation sate of the underlying neutral gas along the line of sight. Disentangling these properties is virtually impossible given observational absorption information alone.

Fortunately, we have the freedom to test which fluctuations dominate absorption profiles within our numerical simulations. For instance, we found that the miscellany of metal distributions along DLA sightlines does not significantly affect the global VWD (see the top-middle panel of figure 3.2). We obtained this by setting the particle metallicity to $Z = 0.3Z_{\odot}$ everywhere, assuming a solar silicon-to-metal ratio (Asplund et al., 2009).

However, this result does not imply that metals are distributed evenly within DLA systems. Using a constant (or a smoothed) particle metallicity can in fact change the measured velocity width radically on an individual sightline basis. Rather, it appears that for sightlines intersecting complex regions of neutral gas, the outermost gas in velocity space is equally likely to be more/less enriched than the rest of the DLA system. Thus the corresponding $\tau_{\rm app}$ features were equally likely to be promoted/demoted above/below the updated 5% total integrated optical depth threshold, thus increasing/decreasing the velocity width.

The value $0.3Z_{\odot}$ was chosen as it is approximately the H I weighted mean metallicity of all the particles in the reference simulation. However, using different values

yielded similar results, as variation in the metal abundance is offset by our choice of selecting the strongest, non-saturated transition of Si II to measure the sightline kinematics. In principle, v_{90} is independent of the magnitude of the optical depth, provided that the profile is unsaturated. Again, this result is reassuring as the Si II column density is so low for some of our reference spectra that the ion would have been undetectable observationally. In practice however, in observervational studies, there is a large set of low-ion metal species with unsaturated transitions that can be used – not just Si II.

3.2.4 Metal Species

We checked the robustness of our results to the choice of Si II as our representative low-ion metal species by repeating our analysis using Fe II, Al II and O I. These species are a subset of those used by N13 to measure DLA kinematics and are amongst the 11 elements traced individually in OWLS. We excluded the effects of varied ionisation potentials of these species by assuming the same ionisation fractions as for Si II (see equation 2.3.1 and section 3.2.7).

The resulting VWDs were virtually unchanged relative to the reference profile (not shown). Hence, chemical abundance ratios did not vary greatly along lines of sight for our simulated DLA systems. Indeed, it has already been observed that the optical depth profiles of low-ion metals follow each other very closely, reflecting their common origin.

3.2.5 Saturation Bias

To ensure that every significant kinematic feature in $\tau_{\rm app}$ has been detected, observational studies typically implement a minimum strength criterion for their choice of low-ion metal transition to measure the DLA kinematics. Prochaska & Wolfe (2010) for example require that $max(\tau_{\rm app}) \geq -ln(0.6)$. In addition, these studies implement a maximum strength threshold to counter the effects of saturation on $\tau_{\rm app}$. This criterion is typically $\tau_{\rm app} \leq -ln(0.1)$ over the entire profile. Of the qualifying transitions, the strongest profile is then chosen to measure the sightline kinematics.

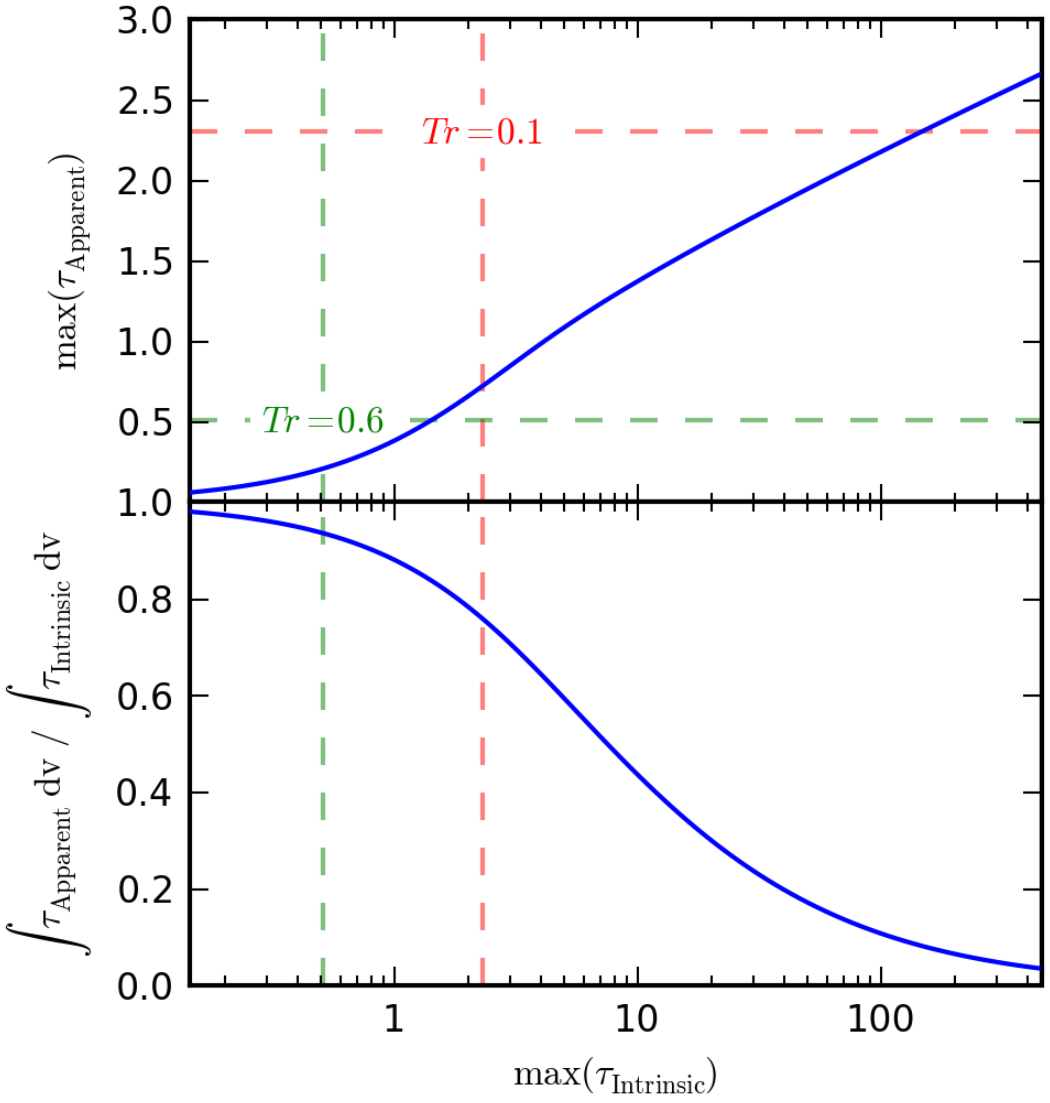

Figure 3.3: Top: the peak *apparent* optical depth as a function of the peak *intrinsic* optical depth for 10^4 K Si II occupying a single velocity phase – as observed by a 8 km/s FWHM Gaussian instrument. Analogous to the curve of growth, this profile diverges from linearity for absorbers exceeding $\tau = 1$. A single phase $\tau = 144$ absorber may appear unsaturated: Si II is unresolved. Smoothing of τ_{app} is not included here; this practice exaggerates the above behaviour given an 8 km/s top hat. Bottom: the ratio of the integrated apparent and intrinsic optical depth profiles. The amplitude of strong, intrinsically saturated absorption features are greatly diminished, influencing the measured velocity width as lower column density features become relatively significant. See text.

Due to the *intrinsic* saturation of unresolved Si II lines (with respect to the instrumental profile): we have discovered a bias towards larger velocity widths for spectra that, nevertheless, satisfy the above criteria.

Because the transmission, not the optical depth, of each QSO sightline is convolved with an instrumental profile, the resulting $\tau_{\rm app}$ profile is not a simple convolution of two Gaussians.[2] As a result, when transforming from τ to $\tau_{\rm app}$, the overall amplitude of strong, saturated absorption features are greatly diminished relative to weak, unsaturated features. On figure 3.3, we illustrate this non-linear transformation for a single velocity phase Si II absorber at 10^4 K as a function of amplitude. Such an absorber may appear unsaturated given a peak intrinsic optical depth of up to 144. In this worst-case scenario, the intersection of a second 10^4 K absorber of column density $1/500^{\rm th}$ that of the primary absorber will contribute 5% of the total integrated apparent optical depth, hence determining v_{90}. As low column density, outlying absorption features are common, such sightlines will yield artificially inflated velocity width measurements. This applies if few discrete velocity phases are intersected.

Continuous velocity phase (e.g. diverging/converging) gas on the other hand, will yield extended (non-Gaussian) intrinsic optical depth profiles, preserving saturation information when transforming from τ to $\tau_{\rm app}$. Such sightlines do not exhibit saturation bias.

It is interesting to point out that choosing the strongest "unsaturated" low-ion metal line to measure v_{90} exacerbates the effect of saturation bias. Furthermore, as higher metallicity spectra are more likely to contain (strong) transitions close to the saturation threshold, saturation bias may be partly responsible for the observed metallicity-v_{90} correlation.

We demonstrate and bound the effect of saturation bias on the DLA VWD in the top-right panel of figure 3.3. We show the intrinsic optical depth VWD in red. The reference distribution (in blue) exhibits 1961 fewer $v_{90} < 20$ km/s sightlines than in the intrinsic case. By rescaling τ such that $max(\tau_{\rm app}) = -ln(0.1)$ (green line) and

[2]However, this approximation does hold at low optical depths.

$max(\tau_{\rm app}) = -ln(0.6)$ (cyan line) we limited the effects of saturation bias on the DLA VWD using the strength/saturation criteria above. This rescaling mimics the freedom to choose a transition from a multitude of low ionisation metal species and not just Si II. Although this bias is only significant below 20 km/s, we demonstrate (in magenta) that relaxing the saturation criterion can dramatically change the DLA VWD. This last profile was obtained by measuring v_{90} on the strongest (1260Å) Si II transition for each sightline, producing a turn over at low velocity widths.

3.2.6 Molecular Hydrogen

By default, we remove molecular hydrogen from the density field using an empirical relationship (derived from Blitz & Rosolowsky, 2006) before performing radiative transfer on our simulations (see section 2.2). Altay et al. (2013) showed that this implementation steepens the CDDF of DLA systems with a column density $N_{\rm HI} > 10^{21}$ cm^{-2}. Such sightlines correspond to intersections of the densest systems in the simulations, where the neutral fraction of hydrogen is saturated. As the amount of H_2 produced by this model should be considered as an upper limit, comparing with a model without H_2 should bracket the influence of molecular hydrogen on our results. Hence, we also considered a variation to our reference model where the ionisation balance of Si II is perfectly coupled to the total neutral fraction of hydrogen, (cf. section 2.3, equation 2.3.1):

$$n_{\rm SiII}/n_{\rm Si} = \left(n_{\rm HI} + 2n_{\rm H_2}\right)/n_{\rm H} \tag{3.2.1}$$

The resulting VWD is shown in the bottom-left panel of figure 3.2. There is no appreciable difference in DLA kinematics between the two implementations.

This can be understood for two reasons. Firstly, the covering factor of the high density gas that is sensitive to our treatment of H_2, is low. Secondly and less importantly, absorption associated with very high density gas is most likely to lie in the center of the optical depth profile. It is the lower density gas also along the line of sight (which is insensitive to our H_2 prescription), that is most likely to occupy the outskirts of the optical depth profile and determine the velocity width.

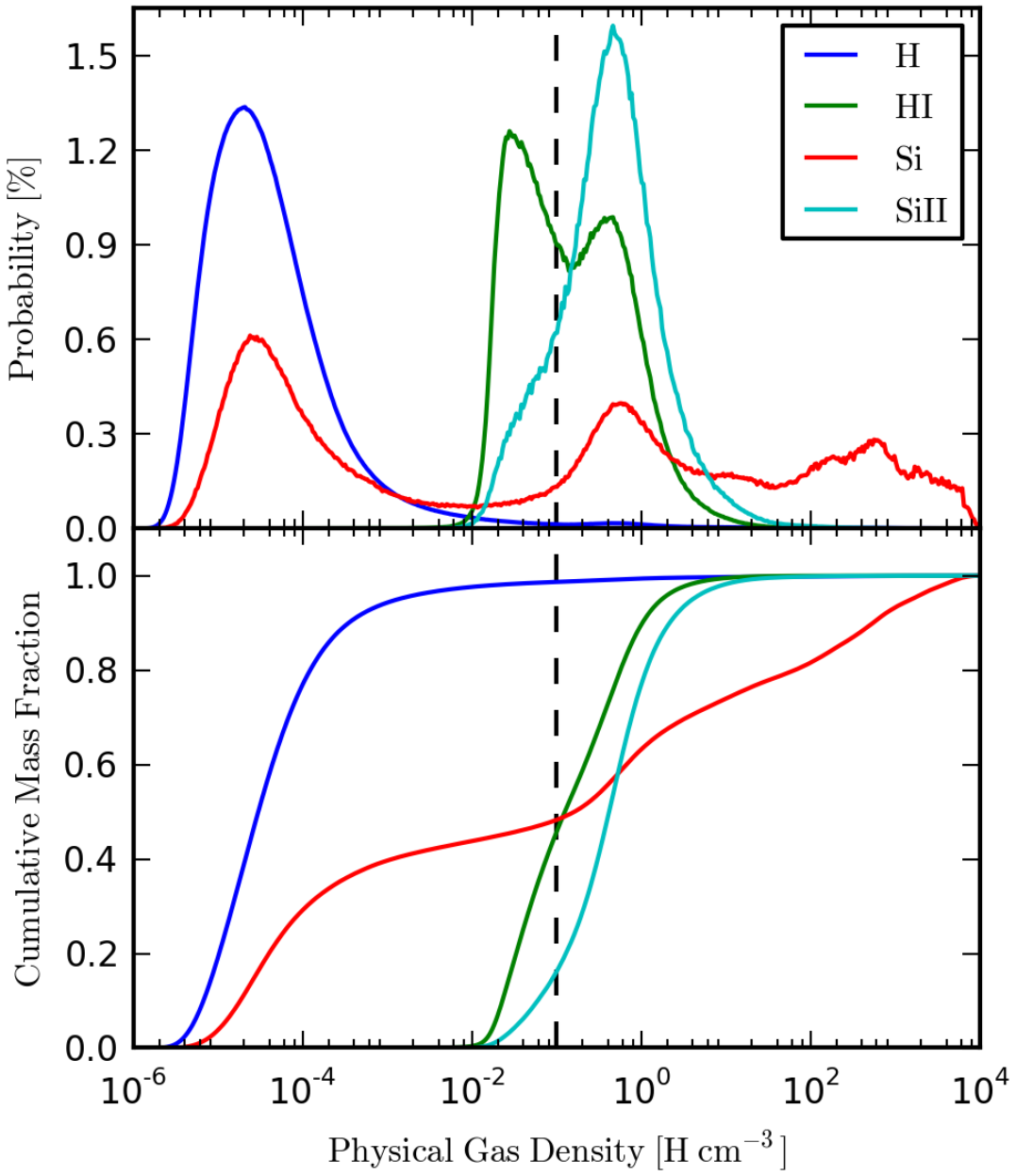

Figure 3.4: The normalised probability function (PF, top) and cumulative PF (or mass fraction, bottom) of SPH particle densities, weighted by their mass in hydrogen (blue), H I (green), silicon (red) and Si II (cyan) for our reference simulation at redshift $z = 3$. The EoS star forming threshold is indicated by the dashed line. Structure formation, enrichment and the influence of self-shielding all influence the distribution of Si II as a function of density in the simulation.

3.2.7 Silicon II Ionisation Potential

In this work, we assumed a Si II ionisation fraction perfectly coupled to that of H I (equation 2.3.1) . However, this neglects the slightly higher Ionisation Potential of Si II (16.3eV) than H I (13.6eV). For a gas of uniform chemical abundance, the additional IP may allow Si II (and other low-ion metals) to persist in lower density environments than H I. Hence, it is possible that some Si II regions in our simulations may be somewhat too compact. Bird et al. (2015) demonstrated that this causes a bias towards low velocity widths (as less velocity space is available to Si II), dramatically shifting the peak of their VWD from ≈ 70 km/s to ≈ 25 km/s.

To investigate this effect, we consider the element/ion weighted probability functions (PF) of particle densities in our reference simulation, see figure 3.4. The majority of baryons in the Universe are within the IGM, as reflected by the hydrogen weighted PF. The transition from optically thin to optically thick gas occurs above $\rho_{\rm H} = 0.01$ cm^{-3} due to self-shielding, giving rise to H I above this density. As this transition is sharp for our URCHIN implementation, the neutral hydrogen fraction saturates quickly. Hence the second peak in the H I profile is solely due to Jean's stability of cooling/collapsing gas piling up at a gas density of $\rho_{\rm H} \simeq 0.5$ cm^{-3}. Above $\rho_{\rm H} = 1.0$ cm^{-3}, the formation of molecular hydrogen suppresses the abundance of H I and the PF quickly drops off.

The distribution of silicon is more complex. Processes such as structure formation and enrichment due to star-formation at high gas densities, as well as outflows of metal enriched gas into the CGM and IGM (below the EoS threshold), are all reflected in the silicon weighted PF.

Alltogether, Si II is found predominantly in environments of higher gas density than H I, where the ionisation fraction is saturated. Away from the H I ionisation front, our Si II – H I coupling assumption is likely to be valid.

In section 3.2.3 we trialled setting the particle metallicity to a constant everywhere. This implementation was paramount to greatly enhancing the abundance of Si II in the interval $0.01 \leq \rho_{\rm H} \leq 0.1$ cm^{-3}, taking this ion right up to the H I ionisation front. This enhancement had no significant effect on the global DLA VWD. Little further velocity space was made available.

We note that if Si II does extend beyond the H I ionisation front, then this additional material must coincide with the host systems' unchanged DLA cross section, have a divergent velocity from the bulk of the neutral gas and have significant column density in order to increase the measured velocity width. As these conditions are quite strict, we do not expect the higher IP of Si II over H I to significantly bias the DLA VWD for our simulations. This conclusion is consistent with the results of Pontzen et al. (2008) (section 5.2) who investigated the effect of braking the perfect coupling assumption by recalculated their Si II ionisation states in the presence of their self-shielding corrected radiation intensity field. However, this conclusion being contrary to the results of Bird et al. (2015) warrants further in investigation. Proper modeling of the Si II ionisation state is probably the most significant limitation of our analysis.

Despite this caveat, we have identified an important issue. A fundamental assumption of DLA kinematic analysis is that low-ion metal absorption provides us with a direct measure of the dynamics of the underlying neutral (hydrogen) gas. Care must be taken in interpreting DLA sightline statistics, such as v_{90}, when this assumption is broken.

3.2.8 Optically Thin Results

As discussed in section 2.2, we performed full, 3D radiative transfer on the OWLS simulations post-processing, using the accurate reverse ray-tracing code URCHIN (Altay & Theuns, 2013). This was a necessary step in calculating the ionisation state of both hydrogen and silicon, as the cold, dense gas that comprises DLA systems is self-shielded from the photoionizing UVB that permeates the Universe. Here and in the following section, we investigate the sensitivity of the DLA VWD to our self-shielding implementation.

For this analysis, we first neglected self-shielding entirely, calculating the ionisation state of silicon (and hydrogen) in the optically thin limit by referring to tables produced by the photoionisation package CLOUDY, in the presence of a HM01 photoionizing background. We used the temperature stored by the simulation for most particles but set the temperature of particle EoS to $T_{\rm EoS} = 10^4$ K. The re-

sulting VWD generated by re-using our reference DLA sightline coordinates (not shown) was virtually identical to the reference distribution. Seemingly, neglecting the self-shielding correction only decreased the amplitude of the Si II optical depth profiles.

However, many of the optically thin reference sightlines no longer corresponded to DLA systems, given their diminished H I column densities. Hence, we also randomly targetted new DLA sightlines using CLOUDY ionisation states for both hydrogen and silicon, having projected the optically thin H I field onto a 2D column density grid (see section 2.6). We show the resulting VWD on the bottom-middle panel of figure 3.2 (red line). As the abundance of DLA systems dropped dramatically, by a factor of 10.01, we normalised the CLOUDY VWD to the reference DLA line density to ease comparison.

In the absence of self-shielding, many regions of previously neutral gas became fully ionised. Only the densest regions in the simulation remained host to sufficient H I to exceed the DLA threshold. As a consequence, turbulent broadening suppressed the abundance of velocity widths below 25 km/s. Only 7 of the $10,080$ CLOUDY sightlines satisfied $v_{90} < 25$ km/s. Sightlines of velocity width $25 < v_{90} < 100$ km/s still existed in the absence of self-shielding. These sightlines probed the dynamics of the coldest, densest gas in the simulation, primarily found in massive, gravitationally bound structures. Far fewer sightlines exceeded $v_{90} > 100$ km/s as the covering fraction of multiple intersections of regions of neutral gas was greatly reduced. We explore the origins of DLA absorption kinematics more closely in section 3.6.

3.2.9 Self-Shielding Implementation

We also considered an alternative self-shielding correction to our reference model by implementing the photoionisation rate fitting formulae of Rahmati et al. (2013a). These fitting functions accurately reproduce the results of post-processing the OWLS reference simulation using the explicitly photon-conserving radiative transfer code TRAPHIC (Pawlik & Schaye, 2008, 2011; Raicevic et al., 2014).

TRAPHIC differs from the URCHIN radiative transfer scheme in several sig-

nificant aspects. Most importantly, recombination radiation is followed explicitly in TRAPHIC, with individual photon packets being traced through the simulation, travelling at the speed of light. This leads to shallower photoionisation fronts than for URCHIN; where photons from recombinations are assumed to be immediately lost or absorbed depending on the local optical depth. On the other hand, URCHIN can calculate the neutral fractions of particles based on the full knowledge of the amplitude and spectral shape of the local radiation field, unlike TRAPHIC which is limited to a small number of frequency bins. As both of these schemes have been used with similar success in predicting the observed H I CDDF of LLSs and DLAs (Altay et al., 2013; Rahmati et al., 2013a, both using the OWLS reference simulation), we expected their resulting H I density fields to yield similar DLA kinematics.

We implemented the Rahmati et al. (2013a) photoionisation rate fitting formulae assuming the usual HM01 photoionising background. As in the optically thin case, we found that recycling our reference DLA sightline coordinates resulted in a very similar VWD (not shown), although the relative abundance of $v_{90} < 20$ km/s sightlines did drop slightly.

In order to fairly probe the fitted TRAPHIC H I density field, we targetted random DLA sightlines as was described in section 2.6. The resulting VWD is shown on the bottom-middle panel of figure 3.2 (green line), normalised to the reference DLA line density for comparison. The total DLA abundance was in fact reduced to $dn/dX = 0.0224$, an offset shown by the green arrow. The abundance of $v_{90} < 20$ km/s sightlines is diminished relative to URCHIN by 36.6% and values in the interval $20 < v_{90} < 10^{1.6} \simeq 40$ km/s are enhanced by 55.5%. Outside this interval, the shape of the DLA VWD profile is unaffected, but the normalization is slightly lower.

This can be understood by the shallower TRAPHIC photoionisation fronts reducing the projected neutral gas cross section of many structures relative to our URCHIN implementation. This reduces the average impact parameter of DLA sightlines with respect to the host halo/galaxy structure. Hence, as sightlines are more likely to intersect high density gas, turbulent broadening contributed more significantly to the VWD, enhancing velocity widths in the interval $20 < v_{90} < 10^{1.6} \simeq$

40 km/s. Furthermore, the reduced neutral gas cross sections meant that fewer sightlines intersected multiple regions of neutral gas along the line of sight. This reduced the total line density of DLAs and lowered the relative normalization of the VWD $\gtrsim$ 40 km/s.

TRAPHIC also suppresses the formation of simple/small, neutral clouds of hydrogen gas, otherwise found in our reference simulation. Such semi-shielded clouds may exist ithe samen isolation in URCHIN, having central densities $\rho_{\rm H} \approx 0.01$ cm^{-3}, insufficient to become self-shielded given the shallower TRAPHIC photoionisation fronts. Other semi-shielded clouds may exist as part of a larger but discontinuous region of hydrogen gas. In our full radiative transfer URCHIN implementation, these clouds are shadowed by neighbouring regions of neutral gas, which significantly obscure the (otherwise isotropic) perceived photoionizing background. For the TRAPHIC fitting functions however, this complex spatial information is lost and lower density gas structures cannot become shielded. It is not clear how this phenomenon affected the resulting VWDs.

Notice that both the TRAPHIC fit (0.0224) and URCHIN (0.0359) implementations significantly underproduce the abundance DLA systems in comparison with recent observations, e.g. $dn/dX = 0.0724$ for Noterdaeme et al. (2012). We anticipate that simply weakening the amplitude of the UVB (which is uncertain by a factor of a few), would shift the transition from ionized to self-shielded gas to lower densities and increase the simulated DLA line density. However, given the complex interplay between DLA velocity widths and the H I distribution, it is hard to predict how changes to the UVB model would affect the VWD. This degree of freedom in the UVB amplitude and spectral shape warrants further kinematic investigation in future work.

3.2.10 Turbulence and Velocity Dispersion

In section 2.4, we calculated the Doppler parameter b of real space absorbers by adding in quadrature a thermal component $b_{\rm therm}$ to a turbulent, kinematic component $b_{\rm turb}$ which characterized the one dimensional unresolved turbulent velocity dispersion of the gas (fully defined in appendix A). Turning off our novel turbulence

prescription yielded the VWD shown in red on the bottom-right panel of figure 3.3. In this case, the abundance of sightlines with velocity widths $v_{90} < 20$ km/s was enhanced by a factor of 1.64, almost exclusively at the expense of sightlines in the interval $20 < v_{90} < 32$ km/s. Unresolved turbulence plays a significant role in broadening single component spectra for our reference simulation, but is not sufficient to produce a VWD that turns over at low velocity widths.

We considered adding the macroscopic particle velocity dispersion to the kinematic broadening of absorbers; as it has been argued that in not doing so, small-scale velocity information is lost for high density systems (see Bird et al. (2015), appendix B). Consider for example two particles with the same mass, contained in a single real space bin, moving with equal and opposite velocities. Averaging their properties will yield an absorber with a peculiar velocity of zero, with a non-zero velocity dispersion – broadening information that may be considered lost.

We added the ion density and kernel weighted dispersion of the particles' peculiar velocities σ_{1D} along the line of sight to each absorption pixel's Doppler parameter thus:

$$b_{\rm disp} = \sqrt{2}\sigma_{1D} \ , \tag{3.2.2a}$$

$$b = \sqrt{b_{\rm therm}^2 + b_{\rm turb}^2 + b_{\rm disp}^2} \ , \tag{3.2.2b}$$

The resulting VWDs including the macroscopic velocity dispersion of particles (cyan) and including both unresolved turbulence and macroscopic velocity dispersion (green) are also shown on the lower right panel of figure 3.2.

Adding the particle velocity dispersion enhanced the relative abundance of v_{90} values above 20 km/s by broadening and/or splitting previously single component optical depth profiles. The overall effect on the VWD was more pronounced than for our turbulence implementation, levelling the VWD below 32 km/s. We found that including both the dispersion and turbulent broadening mechanisms was sufficient to produce a low velocity width turnover at around 30 km/s.

However, this calculation of velocity dispersion diverges from the standard (correct) interpretation of SPH within GADGET simulations. Each SPH particle does not embody a discrete population of gas that could contribute to a physical velocity dispersion. In doing so above, we have falsely implied that the simulation gas

is multi-phase everywhere – in fact, every point in the simulation is within many (~ 48) particles' domain. Rather, gas at any given point in real space is single phase with properties that are by construction the mass- and kernel-weighted average of all the neighbouring particles. Therefore, we did not include particles' peculiar velocity dispersion in our reference analysis.

In summary, the molecular hydrogen prescription and choice of low ion metal species have little effect on the DLA VWD. Simulation redshift, metallicity implementation, saturation bias and the chosen self-shielding correction for neutral hydrogen all affect the VWD at low velocity widths to some degree. The implementation of kinematic broadening may significantly impact the VWD at low velocity widths. Other than neglecting self-shielding entirely, all variations to our reference implementation considered led to consistent DLA VWDs above ~ 35 km/s. We do not expect the higher ionisation potential of Si II to significantly change our results.

3.3 Simulation Model Variations

Thus far, we have focused on the OWLS reference simulation (REF) at $z = 3$, using a 25 Mpc/h box side, 512^3 SPH particles and cosmological parameters from the WMAP 3-year results. The great advantage of the OWLS suite is that the simulations have been repeated systematically many times. By examining the output of each model variation with respect to the reference simulation, it is possible to isolate the effects of individual physical, numerical and cosmological mechanisms. This highly effective strategy has been employed in Schaye et al. (2010) to study the cosmic star formation history; where a detailed description of the OWLS suite can be found. We will only highlight details relevent to our kinematic results.

Altay et al. (2013) also present a detailed analysis on the abundance statistics of LLSs and DLAs in OWLS, for many of the models considered here. In summary, the (normalised) H I CDDF is only sensitive to changes in sub-grid physics models for column densities exceeding $N_{\rm HI} \approx 10^{21.5}$ cm^{-2} (i.e. "strong DLA") where the ISM makes a significant contribution to the matter intersected. As the ISM gas

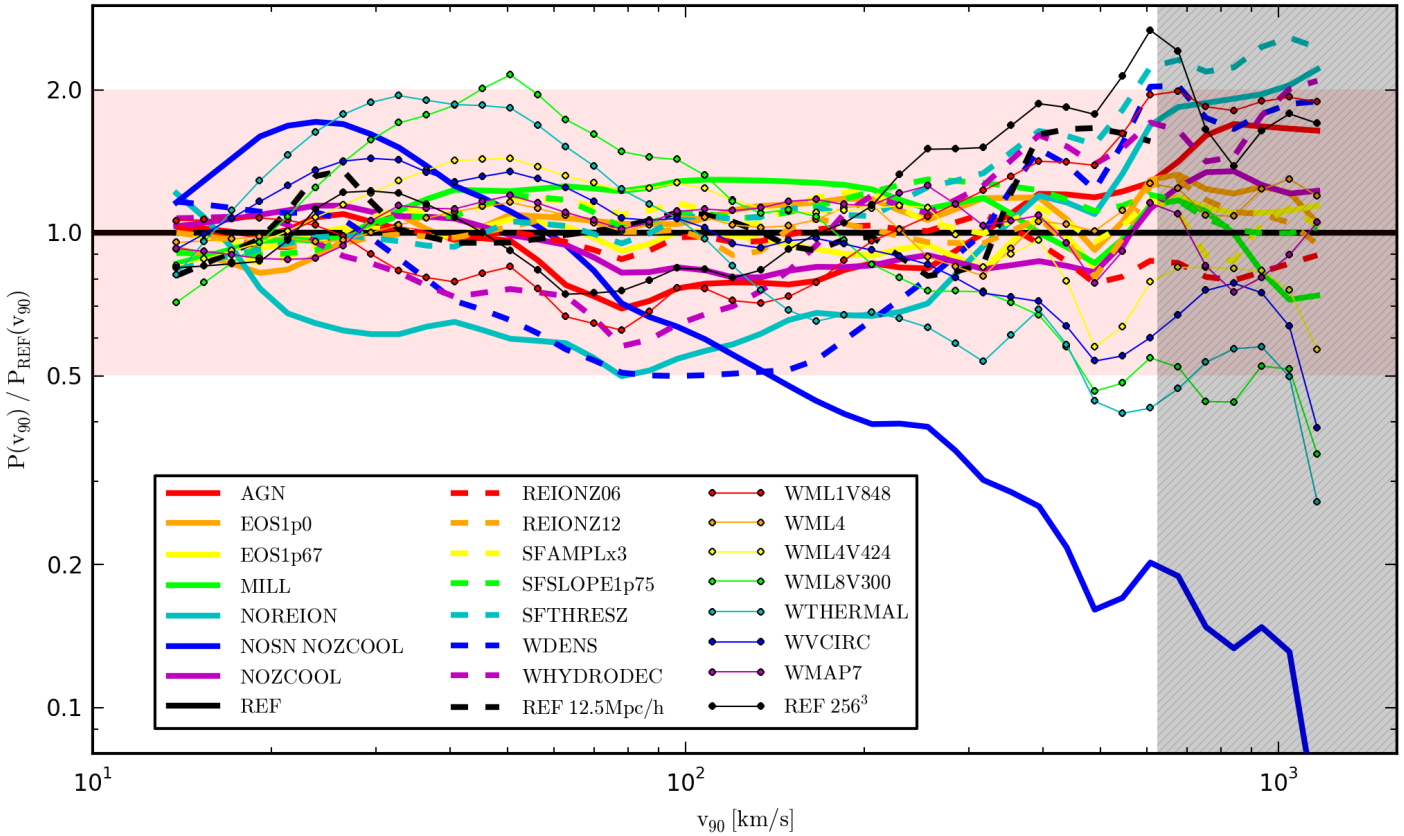

Figure 3.5: The DLA velocity width Probability Function , relative to the reference (REF) 25 Mpc/h, 512^3 SPH particle result, for 23 alternative simulations. Each PF is normalized to one, neglecting changes in the relative abundances of DLA systems. Included are variations to the cosmology, subgrid physics model (including some non-physical models), box size (at the same resolution) and resolution (using the same box size). The shaded pink band highlights a factor of 2 relative difference between the reference and variation velocity width PFs. The v_{90} distribution is broadly unaffected by these changes.

undergoes self-regulating star formation, changes to the sub-grid physics model only significantly affect the distribution of H I gas at high gas densities, hence high column densities. The statistics of strong DLA systems may thus be a valuable resource in constraining the physics of galaxy formation.

On figure 3.5, we plot the DLA velocity width PFs, for 23 alternative OWLS suite simulations, relative to the reference velocity width PF. For each model, we repeated our procedure set out in section 2.6 and pick out 10,080 randomly targetted DLA sightlines at $z = 3$. Each PF is normalised to one, hence neglecting the changes in the relative abundances of DLA in the simulations. Included are variations to the sub-grid baryonic physics model, timing of reionisation, cosmological parameters, resolution and box size. Overall, the distribution of DLA velocity widths in the OWLS suite are robust to these model variations. All but one (non-physical) model are within a factor of 2 of the reference model (highlighted by the shaded pink band).

3.3.1 Non-Physical Outliers

The OWLS project constituted the first simulations to compute particle cooling rates element-by-element and were the first high resolution cosmological simulations to include the effects of photoionisation on the heavy elements. During each time-step, star particles distribute the mass they eject over their neighbouring gas particles using the SPH interpolation scheme. The NOZCOOL model (solid magenta line) neglected metal-line cooling, resulting in consistently lower star formation rates than for REF. However, the resulting distribution of DLA velocity widths did not differ significantly from the reference simulation. Therefore, we identify neglecting the supernovae feedback mechanism in the NOSN NOZCOOL model as the physical cause of this outlying distribution.

Supernovae feedback in OWLS is implemented kinematically by default; where an average of 2 SPH particles, neighbouring newly formed star particles, are launched at 600 km/s in random directions. Removing SN feedback in NOSN NOZCOOL (solid blue line) removes galactic winds/outflows from the simulation, reducing the relative abundance of many dynamic DLAs. Furthermore, gas is allowed to persist more often in the ISM, producing more compact DLA systems than in REF. This

increases the incidence rate of sightlines dominated by dense, turbulent gas – enhancing the abundance of $v_{90} \simeq 25$ km/s sightlines. The typical neutral gas cross section of DLA host systems being smaller for this model, the likelihood of intersecting multiple regions of neutral gas is also reduced, further lowering the relative abundance of $v_{90} \gtrsim 200$ km/s sightlines.

As the name suggests, the NOREION (solid cyan line) model did not include a model for the epoch of reionisation. For REF, this is implemented at redshift $z_r = 9$. [3] We followed our usual procedure in *post-processing* this model at $z = 3$ in the presence of a HM01 UVB in order for our analysis to be consistent. In the absence of reionisation, gas is not photo-evaporated out of sufficiently shallow potential wells (e.g. Okamoto, Gao & Theuns, 2008), nor does photo-heating lead to the gas distribution being smoothed with respect to the dark matter density field (e.g. Pawlik, Schaye & van Scherpenzeel, 2009). As a consequence, the NOREION matter and H I distribution are very different to REF, leading to this outlier in figure 3.5. In fact, the DLA line density of this model is more than doubled ($dn/dX = 0.0873$) relative to REF ($dn/dX = 0.0359$).

3.3.2 Timing of Reionisation

For the REIONZ06 (dashed red) and REIONZ12 (dashed orange) models, where the HM01 UVB was switched on at $z = 6$ and $z = 12$ respectively, the velocity width PFs are very close to the reference result. This reflects the fact that cosmic gas at $z = 3$ retains very little memory of the history of reionisation (e.g. Theuns et al., 2002).

3.3.3 Cosmological Parameters

By default, OWLS used the best fitting ΛCDM parameters to the WMAP 3-year results: $\{\Omega_m,\ \Omega_b,\ \Omega_\lambda,\ \sigma_8,\ n_s,\ h\} = \{\ 0.238,\ 0.0418,\ 0.762,\ 0.74,\ 0.951,\ 0.73\}$ The MILL (solid green) variation assumed the "Millennium cosmology", taken from a

[3] Note that REF assumes that at a photodissociating background is present at $z > z_r$, suppressing molecular cooling at all redshifts).

combined analysis of the WMAP 1-year results and the 2-degree Field Galaxy Redshift survey: { 0.25, 0.045, 0.75, 0.9, 1.0, 0.73}. Model WMAP7 (dotted magenta) duly used the best fitting cosmological parameters to the WMAP 7-year results: { 0.272, 0.0455, 0.728, 0.81, 0.967, 0.704}. As the physical matter density $\Omega_{\rm m}h^2$, physical baryon density $\Omega_{\rm b}h^2$ and the linear amplitude of matter fluctuations σ_8 are higher for these variations than in REF, the MILL and WMAP7 simulations contained a greater abundance of DLA hosting structure: their DLA line densities were 0.0593 and 0.0532 respectively. However, their resulting velocity width PFs did not differ significantly from the reference result. This consistency reflects the hierarchical growth of (DLA hosting) structure in these ΛCDM cosmological simulations.

3.3.4 The ISM Equation of State

The simulations used here have neither the resolution nor the physics to model the multi-phase ISM (Schaye & Dalla Vecchia, 2008). Instead, a polytropic EoS is imposed with slope $\gamma_{\rm eff} = 4/3$ for gas above the star formation threshold $n_{\rm H}^* = 0.1$ cm^{-3}. The EOS1p0 (solid orange) and EOS1p67 (solid yellow) models implemented an isothermal ($\gamma_{\rm eff} = 1$) and adiabatic ($\gamma_{\rm eff} = 5/3$) variation to the EoS. Schaye et al. (2010) have shown that these implementations produce almost identical star formation histories as REF. This was surprising as Schaye & Dalla Vecchia (2008) show that the EoS strongly affects the morphology of galaxies. We also find consistency between these and the reference models' DLA velocity width PFs. Given that turbulence plays a vital role in shaping the REF VWD and depends directly on the polytropic index (see appendix A), this result may be surprising. In total, 54.4% of the H I mass and 84.0% of the Si II mass in the reference simulation is on the EoS at $z = 3$.

3.3.5 Star Formation Model

In OWLS, supernovae feedback enables galaxies to self-regulate their star formation by balancing the accretion rate with galactic outflows. Altay et al. (2013) found that

varying the star formation model only affects the distribution of gas significantly at very high densities, corresponding to H I column densities above $N_{\rm HI} = 10^{21.5}$ cm^{-2} (i.e. "strong DLA"). As only 2.77% of the reference DLA sightlines exceed this column density, it was as expected that the velocity width PF was relatively insensitive to variations in the star-formation model: see models SFAMPLEx3, SFSLOPE1p75, and SFTHRESHZ (dashed yellow, green and cyan lines respectively).

3.3.6 Supernovae Feedback

In the reference model, newly formed star particles inject kinetic energy into their surroundings by kicking, on average, 2 of their SPH neighbours in random directions.

For the WML8V300 (dotted green) model, the total energy injected per supernovae feedback event is the same as in the REF model, but this (kinetic) energy is divided between an average of 8 SPH particles rather than 2. This produces far less efficient galactic winds than in REF as the wind particles are launched at a lower velocities (300 km/s cf. 600 km/s), making this material less likely to overcome both gravity and hydrodynamic drag in escaping the progenitor's potential well. As a result, gas collects more efficiently in the ISM and the relative abundance of dense, turbulent ($v_{90} \approx 25$ km/s) and dynamic ($v_{90} \gtrsim 40$ km/s) DLA sightlines is enhanced. Simultaneously, less neutral gas is entrained in galactic winds, reducing the abundance of $v_{90} \gtrsim 200$ km/s sightlines. Furthermore, the neutral gas cross section of structures is typically reduced, lowering the abundance of the highest velocity width sightlines due to multiple line of sight intersections.

This same behaviour can be seen to a lesser extent in the WML4V424 (dotted yellow) model, where 4 particles on average are launched at 424 km/s. Using a thermal, instead of a kinematic supernovae feedback prescription for the WTHERMAL (dotted cyan) model (Dalla Vecchia & Schaye, 2012) produces even less efficient galactic outflows than for WML8V300.

Conversely, the opposite behaviour can be seen in both the WML1V848 (dotted red) and WHYDRODEC (dashed magenta) models, where galactic winds are produced more efficiently than REF – given WML1V848's average mass loading of 1 particle and WHYDRODEC's temporary decoupling of wind particles from the

hydrodynamics.

For the WML4 (dotted orange) model, the reference mass loading is doubled to 4 particles, but the launch velocity is held at 600 km/s. Hence the kinetic energy injected per feedback is also doubled. However the velocity width PF is virtually unaffected as self-regulation of star formation reduces the frequency of these feedback events. It is primarily each feedback model's launch velocity that effects the DLA kinematics, as demonstrated by the analysis of the WML1V848 model. Although the initial mass loading of this model is low, high velocity (hydrodynamically coupled) wind particles can entrain other gas particles into outflows more efficiently than by ramping up the injected energy.

The WDENS (dashed blue) model was run using a launch velocity which scaled with the local gas density from which the star particle formed. The energy injected per feedback event was held at the reference value but the launch velocity was always higher than for REF. This produced much more efficient winds than REF, yielding a similar, but exaggerated offset in the velocity width PF as the WML1V848 model. Note however, that even this outlier remains within a factor of two of the reference result.

Finally we consider the WVCIRC (dotted blue) feedback model, where the launch velocity and mass loading scales with the the local circular velocity (or halo mass). Overall, this model suppresses the highest column density systems more efficiently than WML1V848 at $z = 3$, but less efficiently than the WDENS model. However, the WVCIRC distribution of velocity widths diverged from the reference result oppositely to these models. In this case, both the wind efficiency and the H I distribution is affected in a manner dependant on the progenitor's mass.

In conclusion, the chosen SN feedback model does not significantly effect the DLA VWD for our range of reasonable prescriptions. Excluding galactic winds entirely however is a different matter. We shall attemt to quantify the importance of galactic winds in determining DLA velocity widths later in section 3.6.

3.3.7 Convergence Tests

We also analysed two further simulations, to test the convergence of our results. The simulation "REF 12 Mpc/h" (dashed black) was run using a 12 Mpc/h box side, so encompassed one eighth of the reference volume. The particle mass resolution was held constant in this simulation by using 8 times fewer SPH and dark matter particles. Simulation "REF 256^3" (dotted black) was run using the same cosmological volume as REF but using 8 times fewer SPH and dark matter particles, of mass $1.1 \times 10^7 M_\odot$/h and $5.1 \times 10^7 M_\odot$/h respectively.

In section 2.5, we countered artificially high v_{90} values caused by Hubble flow across the periodic simulation volumes by cycling our spectra in velocity space. Hence for the 12 Mpc/h $z = 3$ simulation, the velocity width PF drops off above 625 km/s – i.e. 50% of the Hubble flow accross the volume. Strictly, we should exclude velocity widths above $v_{box}/4 = 312.5$ km/s from our analysis of this simulation, due to low mode density fluctuations imprinted on our periodic simulation volumes. The resulting distribution of DLA velocity widths below $v_{90} = 300$ km/s is remarkably consistent with the reference result. This result will be negated in section 3.7 where we show that our reference volume is too small to have converged. The consistency shown here simply reflects that the re-simulated sub-volume was well chosen such that its halo mass function was as close as possible to that of the full reference simulation.

For the 256^3 particle simulation, the velocity width PF is also close to the reference result – within a factor of two almost everywhere. However again, we do not regard the consistency of this result as reliable evidence that our results are converged with respect to the particle mass resolution. The enhanced abundance of $v_{90} > 200$ km/s sightlines is due to a greater incidence rate of multiple neutral gas structures – the typical neutral gas cross sections being larger in this reduced resolution simulation.

We examined the number of particles that gave rise to our reference DLAs and found that $20.84^{+17.26}_{-8.92}$ gas particles contributed 90% of the total H I column density along individual lines of sight. However only $8.61^{+7.89}_{-4.74}$ particles on average contributed 90% of the total Si II column density. Where few neutral, Si II enriched

particles are intersected by DLA sightlines it is very likely that the absorber's underlying kinematic structure is under-resolved. That said, having examined subsets of DLA lines of sight containing fewer than or more than $n \in [2, 8]$ significant $N_{\rm SiII}$ particles, we found that the reference VWD remained robust. Nevertheless, it is our expectation that our persistent over-abundance of low v_{90} DLAs will be somewhat alleviated in higher resolution cosmological simulations as smaller scale spatial variations and velocity space structures can be resolved.

3.4 Smallest Possible Velocity Widths

Consider an absorber with a single velocity phase – for example, a stable gas cloud. In velocity space the resulting intrinsic optical depth profile τ is a Dirac-delta function (of finite amplitude), regardless of the absorber's spacial configuration. Thermal and/or turbulent Doppler broadening will transform τ into a Gaussian profile. Similarly, convolving the transmission with a Gaussian instrumental profile will result in an (almost-) Gaussian $\tau_{\rm app}$ profile, provided that τ is unsaturated. This allows us to solve for the velocity width due to unresolved dynamics ($v_{90,\rm un}$) hence:

$$b_{\rm inst} = \frac{\rm FWHM}{2\sqrt{ln(2)}} \ , \tag{3.4.1a}$$

$$b = \sqrt{b_{\rm inst}^2 + b_{\rm therm}^2 + b_{\rm turb}^2} \ , \tag{3.4.1b}$$

$$v_{90,\rm un} = 2b{\rm erf}^{-1}(0.9) \ , \tag{3.4.1c}$$

where $b_{\rm inst}$ is the pseudo Doppler parameter due to instrumental broadening. Note that this expression does not account for limited spectral resolution and neglects any top-hat smoothing of the $\tau_{\rm app}$ profile done in practice.

For single phase 10^4 K Si II, observed using a Gaussian FWHM= 8 km/s instrument, we find that $v_{90,\rm un}$ = 12.47 km/s. Including 8 km/s top hat smoothing, this increases to 14.60 km/s. Limiting ourselves to 1.4 km/s (high) resolution spectra, we found that the smallest measurable velocity width is 13.6 km/s, or 15.4 km/s with smoothing. At 10^5 K, these values increase to $v_{90,\rm un}$ =19.6 km/s and 22.4 km/s respectively. The smallest (smoothed) observed velocity widths by N13 are 17 km/s overall and 18 km/s for Si II in particular. We hence conclude that DLA sightlines

with $v_{90} \lesssim 20$ km/s are consistent with underlying neutral gas occupying a single velocity phase.

On this subject, we note that Cen (2012), who bracketed observational data from Prochaska (2003), smooth their 3 km/s resolution τ profiles using a 9 pixel box car (27 km/s), rather than calculate the apparent optical depth by convolving their transmission with an instrumental profile. Even for a single phase absorber, with zero broadening, this method would result in a minimum velocity width of 24.3 km/s, biasing Cen (2012)'s VWD against low velocity widths.

3.5 Projection Effects

In section 2.6, we identified DLA sightlines based solely on their total H I column densities through the simulation volume. By recording the $N_{\rm HI}$ due to each Friends-of-Friends halo and Subhalo galaxy intersected along each line of sight, we were able to quantify the contribution by aligned but spatially independent LLS absorbers that exceeded the DLA H I column density criterion.

In total, we found that 361 of 10080 reference sightlines did not intersect an isolated DLA-hosting Friends-of-Friends halo; of which, 290 were promoted to DLA status by another Friends-of-Friends halo and 71 by H I gas in the IGM. Excluding these sightlines did not impact the (normalised) reference VWD. We also found that 1118 sightlines did not intersect an isolated DLA-hosting Subhalo galaxy. Again, excluding these sightlines did not significantly affect the reference VWD. In any case, it is not clear on what scale independent, coincident LLSs with small velocity separations can be distinguished from an independent DLA-hosting structure.

Further, in section 2.6, we did not break up sightlines having intersected more than one DLA-hosting structure. In total, 177 reference sightlines intersected two or more DLA-hosting Friends-of-Friends halos and 352 sightlines intersected two or more DLA-hosting Subfind galaxies. Once again, excluding these sightlines did not affect the reference VWD and besides, it is not clear whether DLAs hosted by structures separated by less than $L/2 = 12.5$ comoving Mpc/h can indeed be distinguished.

Note that multiplying the DLA line density by the total absorption distance (as done by some previous authors) is a poor approximation of the incidence rate of multiple DLA intersections. $dn/dX \times \Delta X = 0.0359 \times 10080 \times 0.133 = 48$ in our case, being three times too low. This is of course due to clustering of DLA-hosting structures, being found primarily in overdense environments.

Consider now the observed equivalent width of a damped Lyman-α H I line (Wolfe, Gawiser & Prochaska, 2005):

$$\Delta\lambda(z, N_{\rm HI}) \approx 10 \times (1+z) \left[\frac{N_{\rm HI}}{10^{20.3}\ {\rm cm}^{-2}}\right]^{1/2}\ {\rm \AA}\ , \tag{3.5.1}$$

expressed in terms of a wavelength interval $\Delta\lambda$. In searching for metal absorption, coinciding with the DLA, we believe it would be reasonable to associate lines within $\Delta\lambda/2$ of the transition's redshifted wavelength. Such a wavelength interval is equivalent to a physical velocity offset Δv due to the Doppler effect and indeed is also equivalent to a Hubble flow redshift error due to a comoving radial separation ΔD_C of absorbers along the line of sight. Consider:

$$\mathrm{v}(z) = c\left[1 - \frac{2}{(1+z)^2+1}\right]\ , \tag{3.5.2a}$$

$$\Delta\mathrm{v}(z) = \mathrm{v}\left(z + \frac{\Delta\lambda}{2\lambda_0}\right) - \mathrm{v}\left(z - \frac{\Delta\lambda}{2\lambda_0}\right)\ , \tag{3.5.2b}$$

$$\Delta D_C(z) = \frac{c}{H_0}\int_{z-\frac{\Delta\lambda}{2\lambda_0}}^{z+\frac{\Delta\lambda}{2\lambda_0}} \frac{dz'}{E(z')}\ , \tag{3.5.2c}$$

where $\lambda_0 = 1215.67$Å is the rest wavelength of Lyman-α and $E(z) = \sqrt{\Omega_m(1+z)^3 + \Omega_\Lambda}$.

By combining equations 3.5.1 and 3.5.2, we find that $\Delta\mathrm{v}(z=3) = 546$ km/s and $\Delta D_C = 24.68$ comoving Mpc/h at the DLA column density threshold at $z = 3$. For N13's sample of 100 high resolution DLA spectra: $\langle\Delta\mathrm{v}\rangle = 852^{+809}_{-353}$ km/s, exceeding 625 km/s for 70(%) of their sightlines; and $\langle\Delta D_C\rangle = 35.9^{+33.1}_{-9.13}$ comoving Mpc/h, exceeding L for 87(%) and $L/2$ for 100(%) of their DLA sightlines.[4]

Therefore, we believe we were justified in utilizing all the Si II absorption exhibited by our artificial transmission spectra in calculating v_{90} (see section 2.5) regardless of whether it originated in a single independent DLA host system or not.

[4]Calculated assuming the OWLS WMAP3 cosmology.

Rather than excluding the contribution of projection effects in this work, we are probably missing some mid- to high-velocity width sightlines due to the limited extent of our simulation volume.

In practice, physical velocities and Hubble flow are indistinguishable given 1D sightline information alone. DLA and metal line absorption associated with DLA can and will originate from multiple independent structures. Care must be taken in interpreting v_{90} as a measure of the gravitational velocity extent of isolated DLA host systems.

We believe it is a misconception to interpret DLAs as arising exclusively from the intersection of single, independent host systems. We quantify how (miss-)association of metal lines with a central DLA host impacts the VWD in the following section.

3.6 Kinematic Weight

Throughout the previous sections, we have highlighted various origins for DLA kinematics without going into much detail. Here we attempt to quantify the fractional contribution by nine distinct kinematic origins to the DLA VWD.

For this purpose, we define $\mathrm{v_i}$ as the isolated velocity extent due to each distinguishable kinematic origin i along each of our DLA sightlines. Note that $\sum_\mathrm{i} \mathrm{v_i}$ needn't equal to the measured velocity width v_{90}. Indeed in the majority of cases, multiple kinematic origins are degenerate or indistinguishable in determining the measured velocity width. With this is mind, we define the kinematic weight k_i of each isolated kinematic origin thus:

$$k_\mathrm{i} = \frac{\min\left(\mathrm{v_i},\ \mathrm{v}_{90}\right)}{\max\left(\sum_\mathrm{i} \mathrm{v_i},\ \mathrm{v}_{90}\right)} \ , \tag{3.6.1}$$

This definition ensures that kinematic origins with larger extents than the measured v_{90} statistic cannot overly dominate the kinematic weight of that sightline. We define the missing kinematic weight k_m as

$$k_\mathrm{m} = \max\left(0,\ 1 - \sum_\mathrm{i} k_\mathrm{i}\right) \ , \tag{3.6.2}$$

such that the total kinematic weight: $k_\mathrm{m} + \sum_\mathrm{i} k_\mathrm{i}$ is always normalised to one.

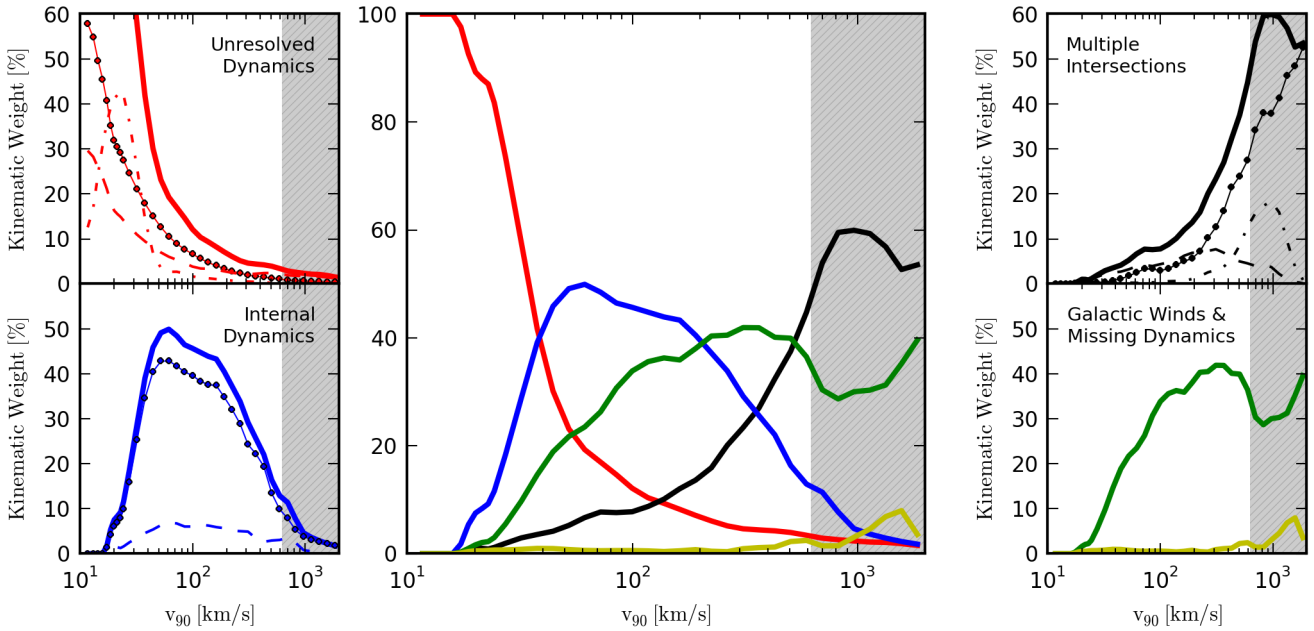

Figure 3.6: The average fractional contributions by different kinematic origins to the velocity widths of randomly targeted DLA sightlines. Unresolved dynamics are shown in red; broken down into instrumental (dotted), turbulent (dot-dashed) and thermal (dashed) broadening. Internal dynamics of host systems are shown in blue; broken down into satellite motion (dashed) and gravitational/hydrodynamic motion (dotted). Dynamics due to galactic winds are shown in green. Multiple intersections of discrete, independent absorbers are shown in black; broken down into pure Hubble flow between host halos (dot-dashed), relative velocities between host halos (dashed) and the total velocities between the primary host and any absorbing IGM material (dotted). Any missing dynamics with respect to v_{90} are shown in yellow.

In figure 3.6, we show the kinematic weight due to each origin as a function of v_{90} for our reference DLA sightlines. As the analysis laid out in this section is a novel approach, we checked that our results did not change significantly for several reasonable variations to our implementation.

3.6.1 Unresolved Dynamics

Firstly, we calculated the kinematic weight ($k_{\rm un}$) due to "unresolved dynamics" – by which we mean thermal and instrumental broadening of low-metal ion absorption lines, as well as broadening due to our prescription of unresolved turbulent motion. To do this, we computed the $N_{\rm SiII}$ weighted average thermal and turbulent Doppler parameters for particles intersected by our reference DLA sightlines and applied equation 3.4.1c to find the total velocity width due to unresolved dynamics ($v_{90,\rm un}$). Note that we applied equation 3.4.1a to find a constant instrumental (pseudo) Doppler parameter of $b_{\rm inst} = 4.80$ km/s for our FWHM= 8 km/s Gaussian instrument. As is shown in the middle panel of figure 3.6, unresolved dynamics dominated the kinematic weight below 38 km/s (red line).

We sub-divided the kinematic weight due to each of the three unresolved origins thus:

$$k_{\rm i} = \frac{b_{\rm i}^2}{b^2} k_{\rm un} \tag{3.6.3}$$

such that their sum equalled to the total unresolved kinematic weight. The break down of unresolved dynamics into these three origins is shown on the top left panel of figure 3.6.

Trivially, the kinematic weight due to constant instrumental broadening decreased linearly with v_{90} (dotted red line). This origin dominated the velocity width of 26.3% of the reference sightlines – Si II being unresolved even for these high resolution spectra.

Similarly, the contribution of thermal broadening (dashed red line) decreases almost linearly. This comes as no surprise as the majority of the neutral gas in the reference simulation was set to a temperature of 10^4 K (c.f. $T_{\rm EoS}$ and $T_{\rm shld}$), yielding a nearly uniform thermal broadening value. The kinematic weight due to thermal broadening raises sightly at high velocity widths due to hot IGM material

that nevertheless contributed at least 5% of the outermost Si II optical depth, see below.

The fact that thermal broadening is less significant than instrumental broadening is because at 10^4 K, $b_{\rm therm} = 2.42$ km/s – only half that of $b_{\rm inst}$. Furthermore, given that $b_{\rm therm} \propto \sqrt{T}$, we can predict that changing the EoS and shielded particle temperatures ($T_{\rm EoS}$ and $T_{\rm shld}$) will not significantly affect the DLA VWD directly (see section 2.2). That said, these temperatures may indirectly affect our results by changing the distribution of H I and Si II gas. Altay et al. (2013) only showed that lower values of $T_{\rm EoS}$ did not change the H I distribution in the reference simulation, warranting further investigation in the future.

Inside the interval $17 < {\rm v}_{90} < 32$ km/s it is turbulent broadening (red dot dashed line) that dominates the kinematic weight (over and above instrumental broadening), constituting 30.5% of the reference sightlines. However, as we have seen previously, the importance of this origin varied greatly with the sub-grid physics model and self-shielding implementation used.

3.6.2 Galactic Winds

As established in section 3.3.6, supernovae feedback driven galactic outflows play a significant role in determining the DLA VWD; although the choice of SN feedback prescription is not important. To isolate the velocity extent due to this origin, we first identified all particles that had been kicked by supernovae feedback after redshift $z = 4$ and removed them from the reference DLA sightlines. In total, such particles made up 18.65% of the Si II mass in the simulation. We then recalculated the resulting velocity widths and chalked up any deficit as the velocity extent due to galactic winds.

This is easily understood where enriched wind material is outflowing, or (later) is infalling having failed to escape the local potential well. On the other hand, gas in the turnaround phase of being recycled does not directly increase the velocity width of most sightlines as it has near-zero relative velocity with respect to the progenitor galaxy. However, all wind material may indirectly increase velocity widths by inflating many galaxy's neutral gas cross section – thus enhancing the incidence

rate of multiple independent structures along the line of sight. In such cases, it is fair to attribute kinematic weight to both multiple intersections (see below) and to galactic winds.

The resulting kinematic weight profile due to galactic winds is shown in green in figure 3.6. Overall the importance of galactic winds rises steadily from ≈ 20 km/s before dominating sightlines within the interval $200 \lesssim v_{90} \lesssim 500$ km/s, constituting 12.2% of all the reference sightlines. At the highest velocity width end, say > 600 km/s, it is the multiple intersection scenario that dominates the kinematic contribution by galactic winds. Although a velocity extent of 1200 km/s is potentially available for our simulated galactic winds, it is highly unlikely to intersect diverging winds travelling parallel to the line of sight at their launch velocity (± 600 km/s).

There are two caveats to this quantification of galactic winds. Firstly, we do not take into account wind particles that have been recycled back onto their progenitor by redshift $z = 3$. Any deficit in velocity widths due to these particles should not have been attributed to galatic winds, but to the internal dynamics of halo structures instead. Secondly, this method also neglects particles entrained into galactic winds by hydrodynamic drag, that weren't directly kicked by a supernovae feedback event (hence weren't assigned a wind-flag). The velocity extent due to these particles is missing from the kinematic weight of galactic winds. Unfortunately, a detailed identification of wind material based on each gas particle's current position and velocity relative to the local potential, in addition to its supernovae feedback history (and that of its closest neighbours), is beyond the scope of this work.

3.6.3 Multiple Intersections

In section 3.5, we showed that the intersection of multiple galaxies, halo structures and the IGM all play a significant role in determining DLA sightline kinematics.

The solid black line in figure 3.6 demonstrates that velocity widths above $\gtrsim$ 500 km/s are dominated by the relative velocities between independent halo structures and between halo structures and the IGM. We consider the relative velocities between central/satellite galaxies belonging to the same halo structure separately

in the next section.

We identified 8% of our reference sightlines as having intersected two or more "significant" Friends-of-Friends halos, where each Friends-of-Friends halo contributed at least 5% of the total Si II column density along the line of sight. For these sightlines, we identified the two outermost Friends-of-Friends halos in velocity space having calculated the relative peculiar velocities between their centre of masses and their separation due to pure Hubble flow along the line of sight. Overall, we found that pure Hubble flow between halos dominated the velocity width of 1% of our reference sightlines, with a kinematic weight profile peaking around 900 km/s (dot dashed black line). The relative peculiar velocities between multiple halos dominated 2.56% of our reference sightlines, peaking around 400 km/s (dashed black line).

We then identified all gas particles in the simulation that did not belong to a Friends-of-Friends halo as being part of the IGM. In total, such particles contributed at least 5% to the total Si II column density for 9.37% of our reference sightlines. By removing all the IGM particles from our reference sightlines and recalculating the velocity widths, we attributed any deficit as originating from the velocity space separation between significant IGM material and the principal DLA host system. This origin dominated the velocity width of 3.75% of the reference sightlines. The resulting kinematic weight is shown by the dotted black line, exceeding the contributions by multiple halo intersections above 250 km/s.

In order for the IGM to contribute so significantly to N_{SiII} for DLA sightlines, this material has to be part of a structure shielded from the photoionizing UVB without being massive enough to be identified as a Friends-of-Friends halo. The neutrality of these structures may be consistent with the phenomenon of semi-shielded clouds arising in the simulation, as discussed in section 3.2.9. Alternatively, it is possible that some of these IGM structures were massive, but had simply been missed by the Friends-of-Friends identification algorithm, having not being linked to any nearby dark matter particles i.e. were entirely baryonic.

These results are likely to be highly resolution dependant. At higher partile mass resolutions, many of the low mass or baryonic structures described above are likely

to be identified as FoF structures, rather than as IGM constituents.

3.6.4 Internal Dynamics

Here we consider the velocity width due to all the resolved internal dynamics within independent DLA host halo systems, encompassing both the relative velocities of central/satellite galaxies and the resolved gravitational/hydrodynamical motion of particles within the halo. For this purpose, we excluded all wind and IGM particles from the reference DLA sightlines. We then re-calculated the spectra having set the Hubble flow of each real space absorption pixel to $v_{box}/2$. The resulting τ profiles were heavily peaked at $v_{box}/2$, with absorption to one or both sides of this peak. We attributed the corresponding velocity widths, less $v_{90,un}$, to the total internal dynamics of each DLA sightline. The corresponding kinematic weight profile is shown in solid blue in figure 3.6, dominating DLA velocity widths between 38 and 200 km/s.

In order to separate out the dynamics due to gravitationally bound central/satellite galaxies along the line of sight, we identified 13.6% of the reference sightlines as having intersected two or more significant Subhalo galaxies (contributing at least 5% to the total N_{SiII}), belonging to the same Friends-of-Friends halo. For these sightlines, we attributed the maximum relative velocity of the Subhalo centre of masses (along the line of sight) to be the velocity extent due to satellite motion. This kinematic origin dominated the velocity width of 5.1% of sightlines and has a relatively flat profile as shown by the dashed blue kinematic weight profile in figure 3.6.

By subtracting the velocity extent due to satellite motion from the total internal dynamics, we identified the remaining velocity extent as being solely due to the gravitational/hydrodynamical motion of particles within each DLA-hosting structure. The resulting kinematic weight profile is shown in dotted blue in figure 3.6. This origin dominated the velocity width of 18.1% of the reference sightlines. Unfortunately, it was beyond the scope of this work to quantify the relative contribution of physical processes such as rotational dynamics to this kinematic origin.

3.6.5 Missing Kinematic Weight

Overall, the missing kinematic weight i.e. the velocity width unattributed to any of the kinematic origins above, only dominated 26 reference sightlines – all of velocity width above 625 km/s. The resulting kinematic weight profile is shown in yellow on figure 3.6.

3.7 DLA Host Halos

In figure 3.7, we plot the PDF of log Friends-of-Friends halo mass for all halos in the reference simulation (black) i.e. the halo mass function. Only 9 halos exceed $10^{12} M_{\odot}$ at redshift $z = 3$. The profile for DLA host halos intersected by our reference sightlines is shown in blue. Multiple halo intersections are weighted by their individual H I column densities, normalised over the total $N_{\rm HI}$ for each sightline. This profile shows that halos with mass $\lesssim 10^{9} M_{\odot}$ do not contribute significantly to the total DLA covering on the sky. The peak at $10^{8} M_{\odot}$ is mainly due to low mass halos being serendipitously intersected by DLA sightlines hosted by other halos, see section 3.5. Above $10^{9} M_{\odot}$, the typical DLA cross section increases with halo mass, offsetting the underlying halo mass function.

It is clear that our results are not converged with respect to the size of the cosmological volume because the (blue) DLA host halo profile does not turn over at high masses. Had we analysed a larger volume at the same resolution, probing the halo mass function out to higher masses, the resulting DLA line density would have been larger. Indeed, the 9 most massive Friends-of-Friends halos were the principal hosts of 17.6% of our reference DLAs.

By breaking down the DLA-host halo profile by velocity width, we can see that low (high) v_{90} DLAs are preferentially hosted by low (high) mass halos. We expect that a larger cosmological volume at the same resolution would exhibit a similar VWD as our reference simulation, but the relative excess of low v_{90} sightlines would be diminished. Note that we find that halos of all masses are host to velocity widths of all values. Despite such velocities not being available gravitationally, low mass halos contribute to high velocity width DLA sightlines via multiple intersections.

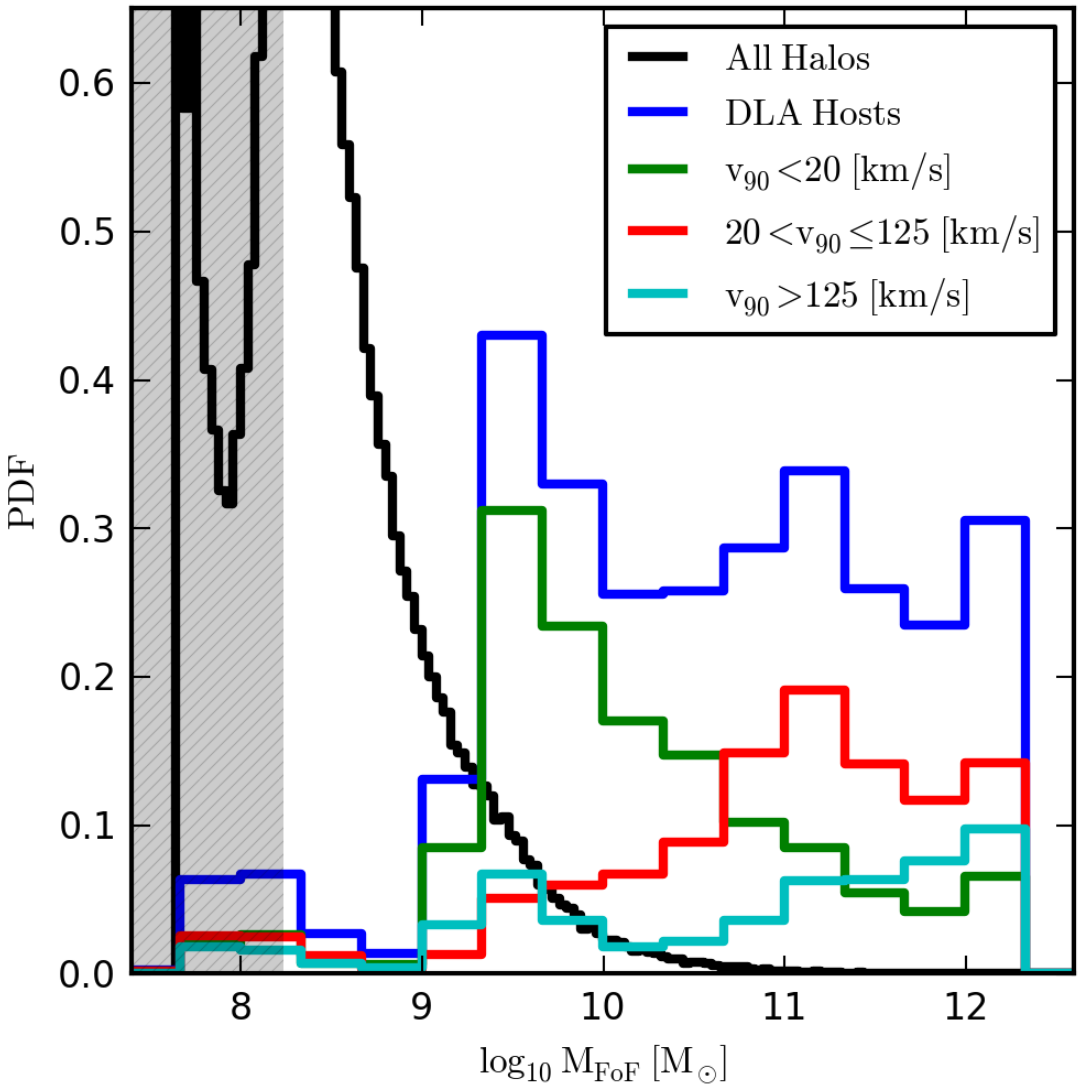

Figure 3.7: The PDF of log Friends-of-Friends halo mass, for all halos within the reference simulation (black) and for randomly intersected DLA hosts (blue) – binned by low, medium and high velocity widths (green, red and cyan respectively). The shaded region excludes Friends-of-Friends halos with < 20 particles. Low(high) v_{90} sightlines are preferentially hosted by low(high) mass Friends-of-Friends halos. As the DLA host halo mass function has not tailed off at high masses, our results are not converged with respect to box size – we are missing high mass DLA host halos.

The average virial velocity for our DLA host halos is $v_{vir} = 75.6^{+99.6}_{-42.5}$ km/s, where $v_{vir} = \sqrt{GM/R_{200}}$. [5] The average velocity width to virial velocity ratio is $v_{90}/v_{vir} = 0.51^{+1.41}_{-0.36}$. These results are consistent with those of B15. Note that we excluded 540 reference sightlines from these calculations as their principal host halos did not have well defined virial radii.

On figure 2.2, we show the projected H I column density and velocity width map for three orthogonal projections of an isolated ($10^{11.5}M_\odot$) Friends-of-Friends halo. This figure indicates that the DLA covering factor drops with increasing impact parameter, fragmenting into a number of DLA clouds. A small fraction of this covering factor extends outside the virial radius. There appears to be no correlation between velocity width and impact parameter; with almost all v_{90} values being obtained at all radii.

We confirmed that these observations are typical by examining a sample of 1000 isolated Friends-of-Friends halos, as extracted from the reference simulation in section 2.7. For example in figure 3.8, we show the stacked, normalised PDFs of impact parameter b (not to be confused with Doppler parameter b) over virial radius (R_{200}) as a function of v_{90} for these halo projections. Each halo projection was weighted by its total DLA cross section and by an integral of the halo mass function: $P \propto M_{FoF}^{-1.9}$ – taken over a mass range closest to that halo within the sample. This method counters the fact that our sample of FoF halos does not fairly represent a ΛCDM universe. We cannot account for halos of mass $< 10^{8.5}M_\odot$ or $> 10^{12.5}M_\odot$ and choose not to extrapolate our results.

It is clear that v_{90} and b/R_{200} are not correlated. Similarly, we found that impact parameter and v_{90} are not correlated. We find that DLA sightlines typically intersect (isolated) FoF halos at $0.30^{+0.50}_{-0.20}$ R_{200}. These conclusions hold for all halo masses. v_{90} is a highly stochastic statistic, reflecting the diverse configurations of neutral gas that may be randomly probed by an unassociated background quasar.

On figure 3.10, we show the stacked, normalised PDFs of v_{90} as a function of N_{HI}, using the same method as for figure 3.8. Above 10^{21} cm^{-2}, a forbidden low-v_{90}

[5] We remind the reader that all errors given in the text indicate the corresponding 16^{th} and 84^{th} percentile bands – 1σ for a normal distribution.

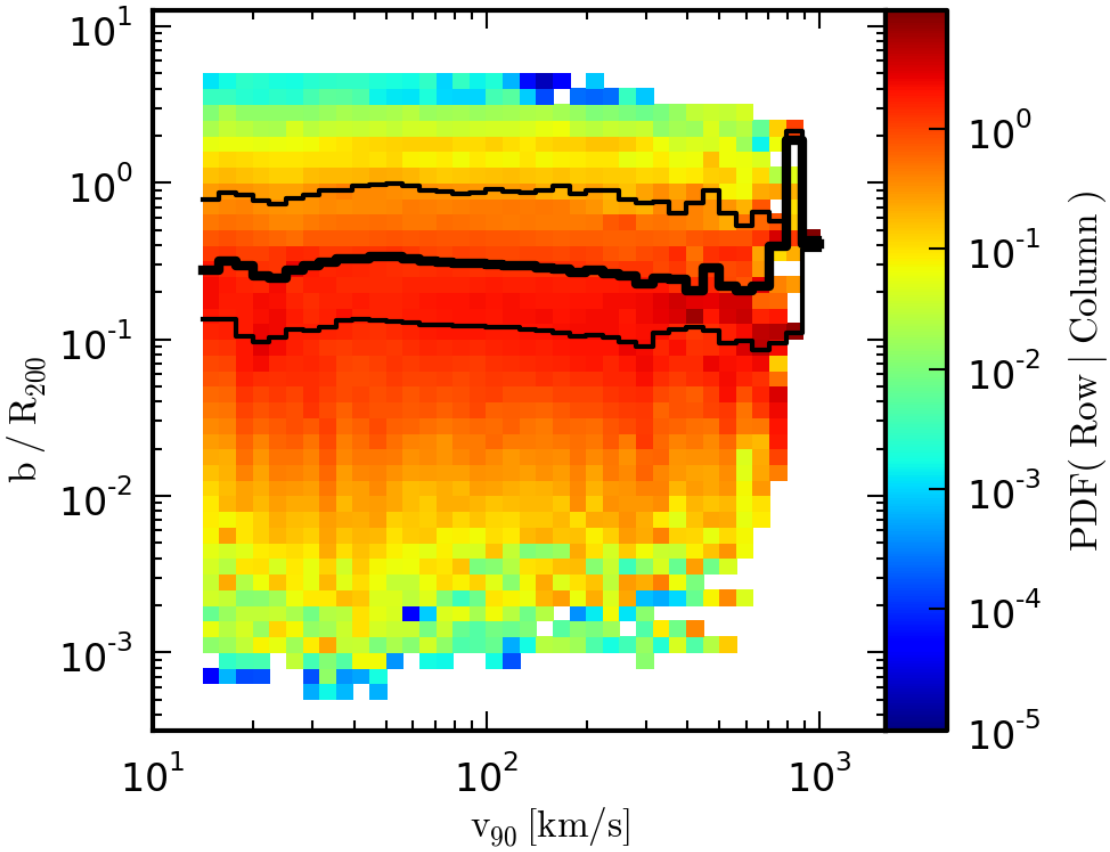

Figure 3.8: The stacked, column normalised PDFs of impact parameter over virial radius as a function of velocity width for our sample of Friends-of-Friends halo projections. Each halo projection is weighted by its total DLA cross section and by an integral of the halo mass function. The 16th, 50th and 84th percentiles are indicated by the solid black lines. It is clear that b/R_{200} and v_{90} are not correlated.

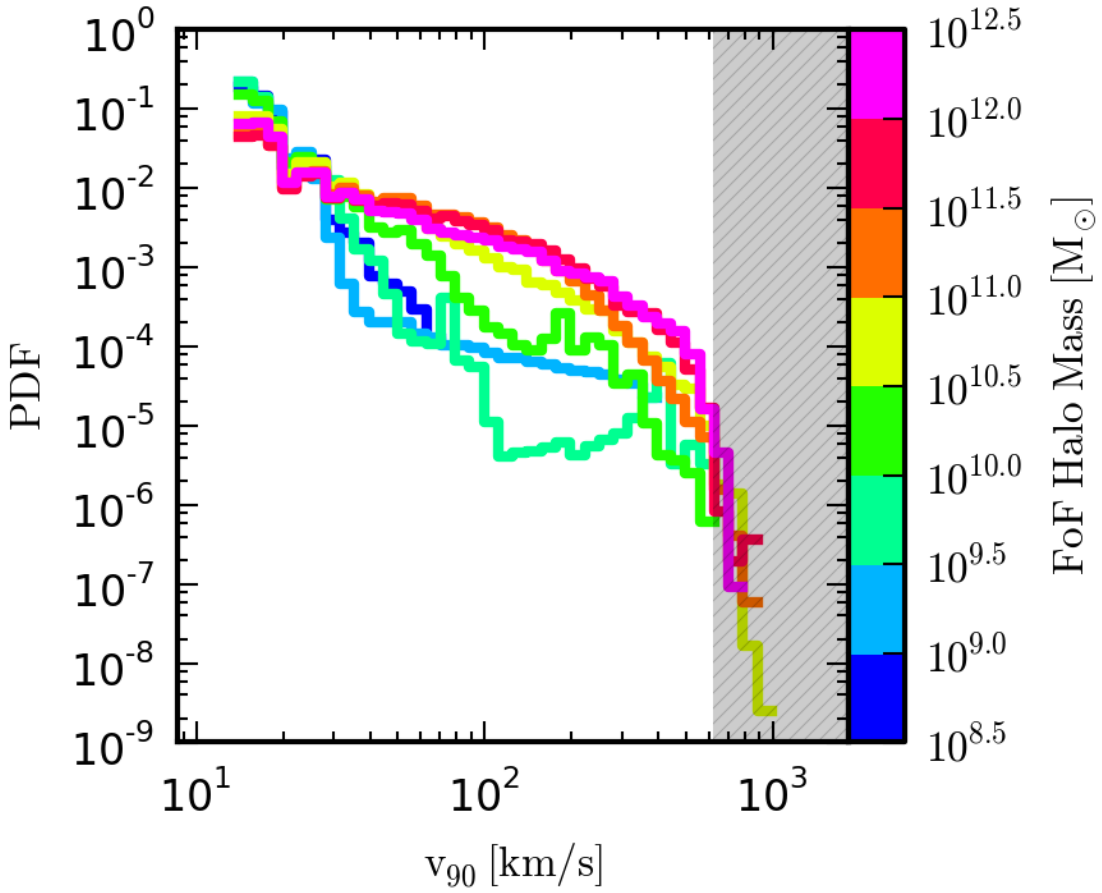

Figure 3.9: The velocity width PDF, binned by halo mass, for our sample of isolated FoF halo projections. Within each mass bin, each halo projection's PDF is weighted by its total DLA cross section and by an integral of the halo mass function. As implied by figure 3.7, the DLA VWD is halo mass dependant, with low(high) velocity widths being preferentially hosted by low(high) mass halos. However, by isolating each halo, we neglect neutral gas in the IGM and multiple halo intersections / projection effects.

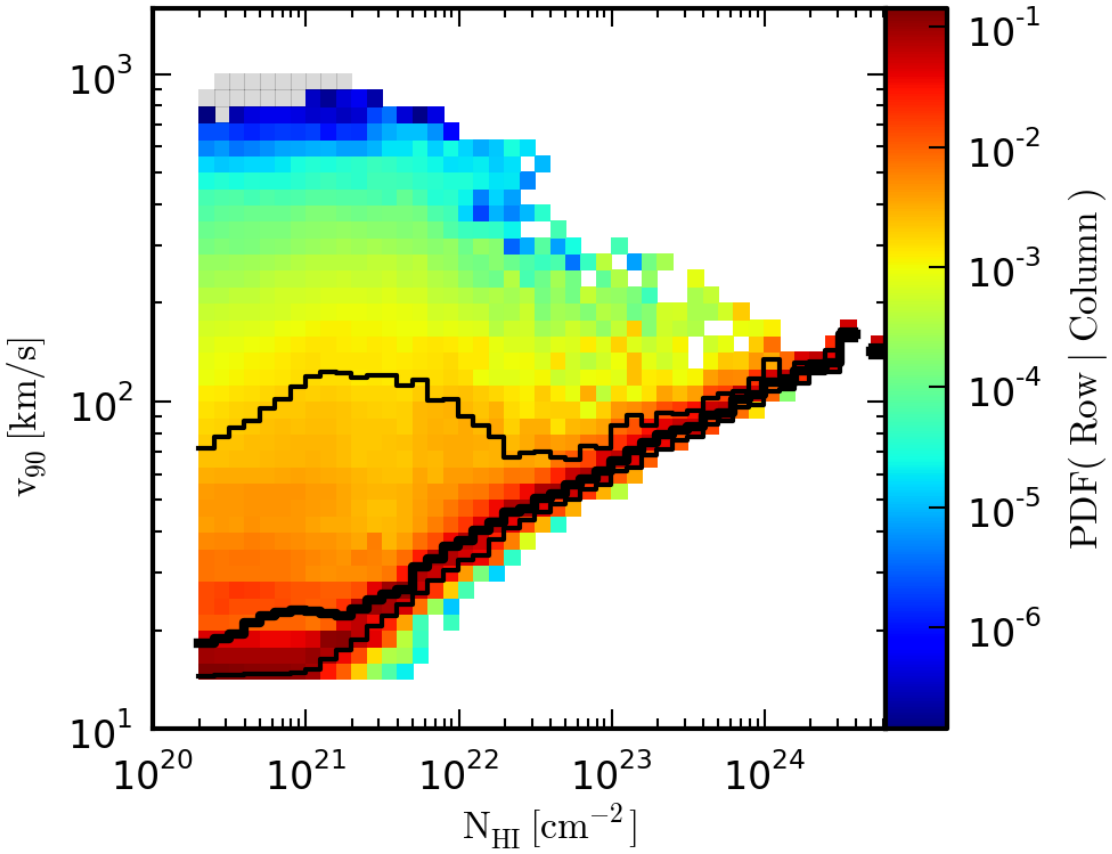

Figure 3.10: The stacked, column normalised PDFs of velocity width as a function of H I column density for our sample of Friends-of-Friends halo projections, as per figure 3.8. Grey pixels have a probability density less than the colourbar's lower bound. Above 10^{21}[cm^{-2}], a forbidden low-v_{90}, high-$N_{\rm HI}$ region is evident, resulting in a tight velocity width – H I column density correlation above, say, 10^{22}[cm^{-2}].

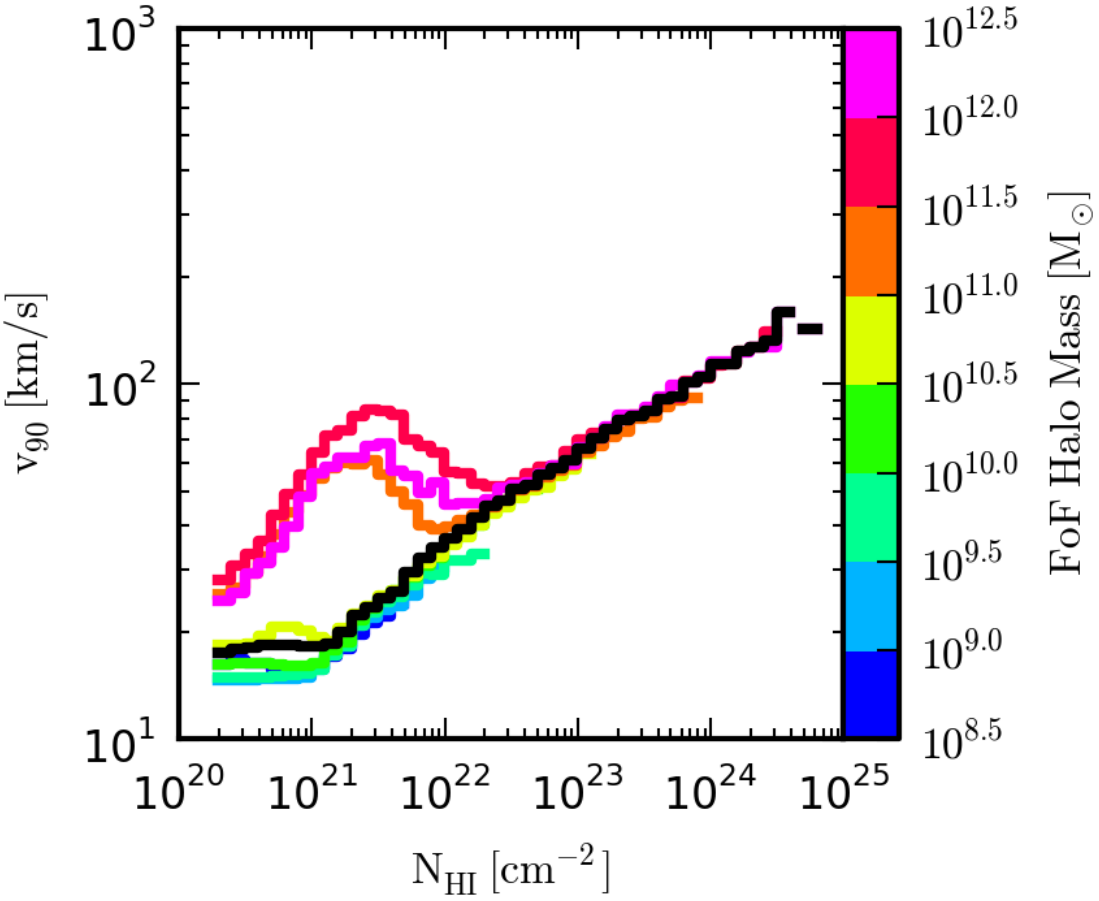

Figure 3.11: The median velocity width as a function of H I column density, binned by halo mass, for our sample of Friends-of-Friends halo projections. Within each mass bin, each halo projection is weighted by its total DLA cross section and by an integral of the halo mass function. In black, we also plot the global median as per figure 3.10. As the v_{90}–N_{HI} correlation evolves somewhat, it may be possible to constrain DLA host halo masses using these two observable properties.

and high-$N_{\rm HI}$ region is evident, resulting in a tight velocity width – H I column density correlation above $\sim 10^{22}$ cm^{-2}. Between 10^{21} and 10^{22} cm^{-2} the correlation is present, but the data is spread over a large velocity width interval. Sightlines can only achieve column densities $\gtrsim 10^{21}$[cm^{-2}] by intersecting multiple, massive (dynamic) or dense (turbulent) regions of neutral gas within these isolated halos – hence suppressing low velocity widths. The equivalent results for $N_{\rm SiII}$ (not shown) are very noisy.

At this point, it is prudent to ask whether we can use the relationship between these two observables to infer underlying properties such as the host halo mass? In fact, the $v_{90}(N_{\rm HI})$ PDF does evolve somewhat with halo mass, albeit below 10^{22}[cm^{-2}], appearing bimodal for host halos of mass above/below $10^{11} M_{\odot}$ – see figure 3.11. This is mainly due to a mass evolution of the DLA VWD, implied in figure 3.7 and shown explicitly in figure 3.9 for our sample of isolated FoF halos.

However, these behaviours are only evident for isolated FoF halos. For our randomly targeted reference sightlines, any underlying v_{90}–$N_{\rm HI}$ correlation is nullified by: multiple halo intersections, neutral gas in the IGM and the fact that DLA column densities above 10^{22} cm^{-2} are very rare. Furthermore, simulated H I column densities above $\sim 10^{21.5}$ cm^{-2} are quite sensitive to the uncertain molecular hydrogen prescription; the CDDF in this regime is not well constrained by current observations. Note that our isolated FoF projections only achieved huge H I column densities up to 10^{25} cm^{-2} because of the very high grid resolution implemented.

We conclude that observables such as v_{90} cannot be used as a proxy for the DLA host halo mass given the current generation of observations on an individual sightline basis. That said, we recognise the potential for sightline/kinematic statistics to become powerful diagnostic tools for constraining the global distributions of underlying DLA host halo properties in the future.

Chapter 4

Further Results

In this chapter, we present further results, supplementary to our main analysis. The reader may wish to skip ahead to the final chapter (5) and then return, rather than distract from the principal theme of this work.

4.1 HI Distribution

In this section, we consider the distribution of H I gas surrounding our sample of 1000 isolated FoF halos, as extracted in section 2.6 with the following addendum: in this section only, we include three orthogonal projections for each isolated FoF halo rather than one. We only consider a single projection elsewhere because of the overhead in calculating sightline kinematics. All the results presented in this section are binned by the total FoF halo mass. Within each mass bin, each halo projection was weighted by an integral of the halo mass function: $\mathrm{P} \propto \mathrm{M}_{\mathrm{FoF}}^{-1.9}$ – taken over a mass range closest to that halo within the sample. This method counters the fact that our sample of FoF halos does not fairly represent a ΛCDM universe. We cannot account for halos of mass $< 10^{8.5} M_{\odot}$ or $> 10^{12.5} M_{\odot}$ and choose not to extrapolate our results. Where appropriate, we also weight each halo projection by its total DLA cross section.

In order to be succinct in this section, we refer the reader to each figure's caption for a discussion of what is shown.

- In figure 4.1 we show how the DLA column density distribution function

evolves with halo mass.

- In figure 4.2 we plot the DLA covering fraction and cross sectional radial profiles as a function of impact parameter and b/R_{200}. Such mass-dependent profiles may be very useful in semi-analytic modelling of DLA hosts.

- In figure 4.3 we plot the LLS covering fraction and cross sectional radial profiles as a function of impact parameter and b/R_{200} (as per figure 4.2). Although we have not considered LLS in this work, they are a considerable area of interest for many readers.

- In figure 4.4 we show the PDF of DLA impact parameter as a function of FoF halo mass. Such PDFs can be derived by integrating the profiles shown in figure 4.2; however, we found these PDFs informative enough to show explicitly.

- Similarly, in figure 4.5, we show the PDF of b/R_{200} for DLA sightlines as a function of halo mass.

- In figure 4.6, we quantify the fragmentation of the DLA covering factor which you may have noticed in figure 2.2. It would be unwise to assume that DLA host halos are surrounded by a continuous, spherically symmetric distribution of H I gas. For clarity, we have used 4 rather than 8 mass bins.

- In figure 4.7, we plot the likelihood of intersecting a continuous DLA silhouette of a given (projected) size. Note that each DLA silhouette may be due to the projection of multiple regions of neutral gas along the line of sight belonging to the same isolated FoF halo. For clarity, we have used 4 rather than 8 mass bins.

Relevant but not shown results include the radial H I column density profiles as a function of impact parameter or b/R_{200}. These quantities are not correlated.

An elegant (semi-analytic) model for the H I distribution around DLA host halos would incorporate all of the subject areas explored in this section.

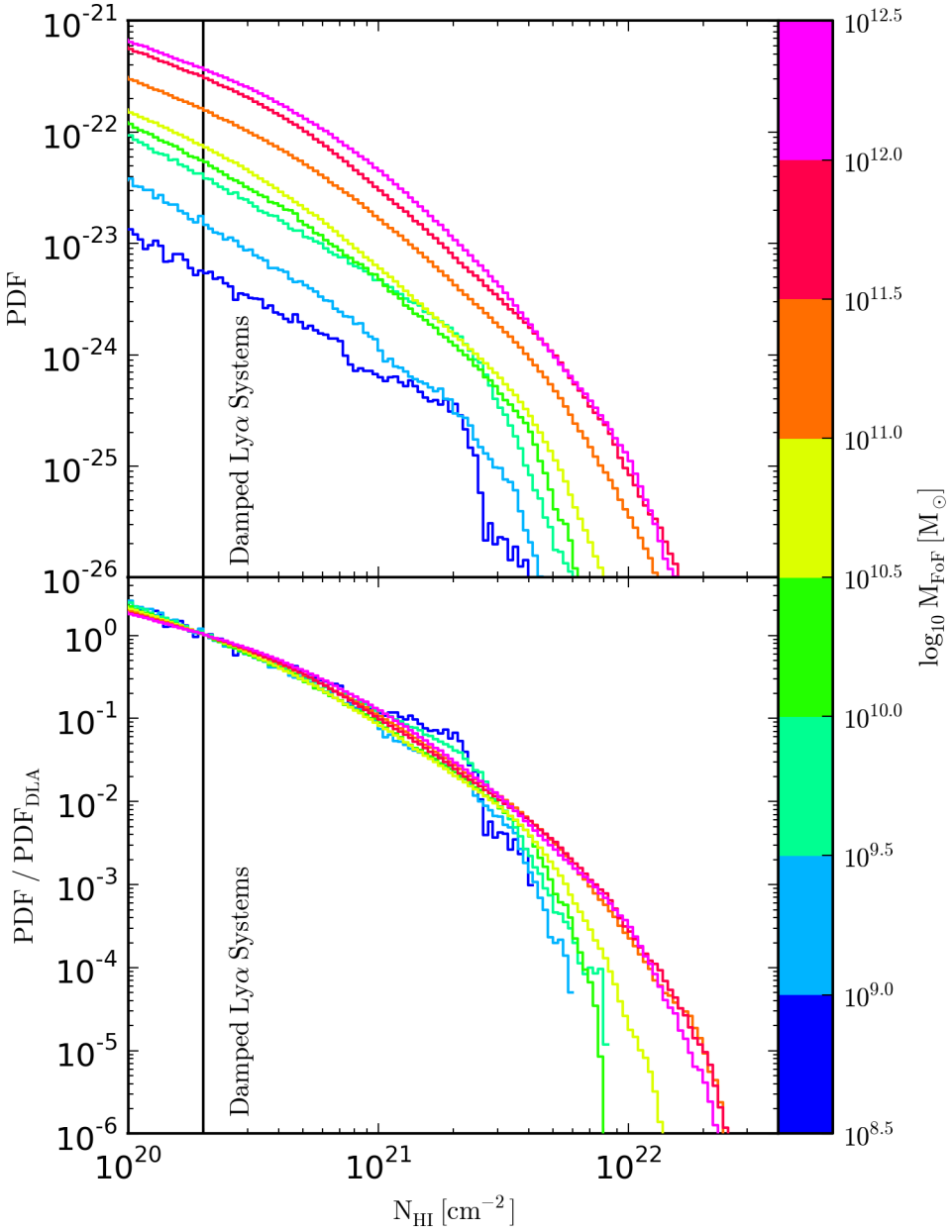

Figure 4.1: Top: the H I column density PDFs for our sample of projected FoF halos, binned by halo mass. Within each mass bin, each halo projection's PDF is weighted by an integral of the halo mass function. DLA sightlines at all column densities are more common for high mass halos than for low mass halos. Bottom: as above, but renormalised at the DLA threshold. Up to $N_{\rm HI} = 2 \times 10^{21}{\rm cm}^{-2}$, the shape of the DLA CDDF is consistent/self-similar for all halo masses; beyond which the profile is gradually cut off, with higher mass halos extending to higher column densities than low mass halos. We cannot rule out that the CDDFs of FoF halos of mass $< 10^{9.0} M_\odot$ level out around $N_{\rm HI} = 10^{21}{\rm cm}^{-2}$, unlike high(er) mass halos. However, these halos have the poorest particle resolution out of our sample and may possibly include spurious neutral structures/clouds – see text.

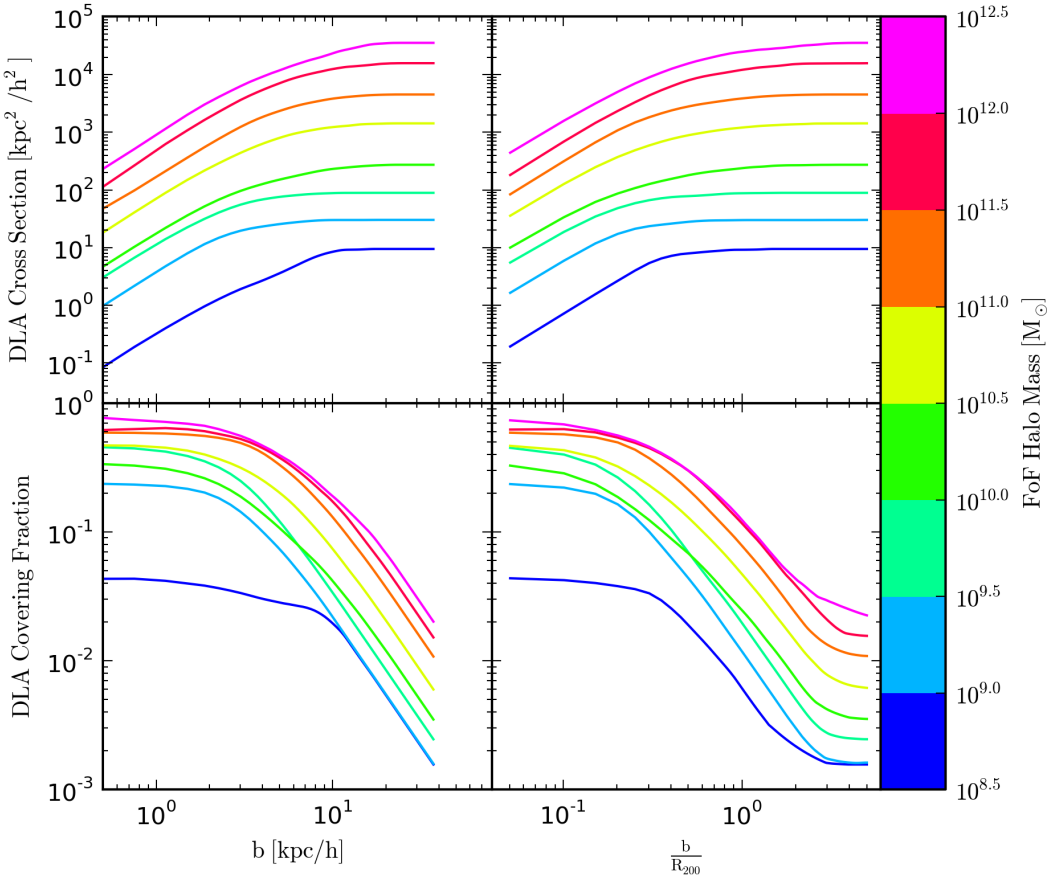

Figure 4.2: The typical DLA cross section (top) and covering fraction (bottom) radial profile as a function of comoving impact parameter (left) and impact parameter over virial radius (right), for our sample of projected FoF halos, binned by halo mass. Within each mass bin, each halo projection's PDF is weighted by an integral of the halo mass function. As expected, high mass halos achieve larger DLA cross sections and covering fractions than low mass halos at all radii. For high mass halos, DLA may extend significantly beyond the virial radius. We candidly note that at the virial radius there is no tangible structural change for halos in general, R_{200} is simply a convenient unit of measurement. These radial profiles are broadly self-similar in shape for all halo masses, except for the lowest mass halos considered ($< 10^{9.0} M_\odot$). However, these halos have the poorest particle resolution out of our sample and may possibly include spurious neutral structures/clouds – see text.

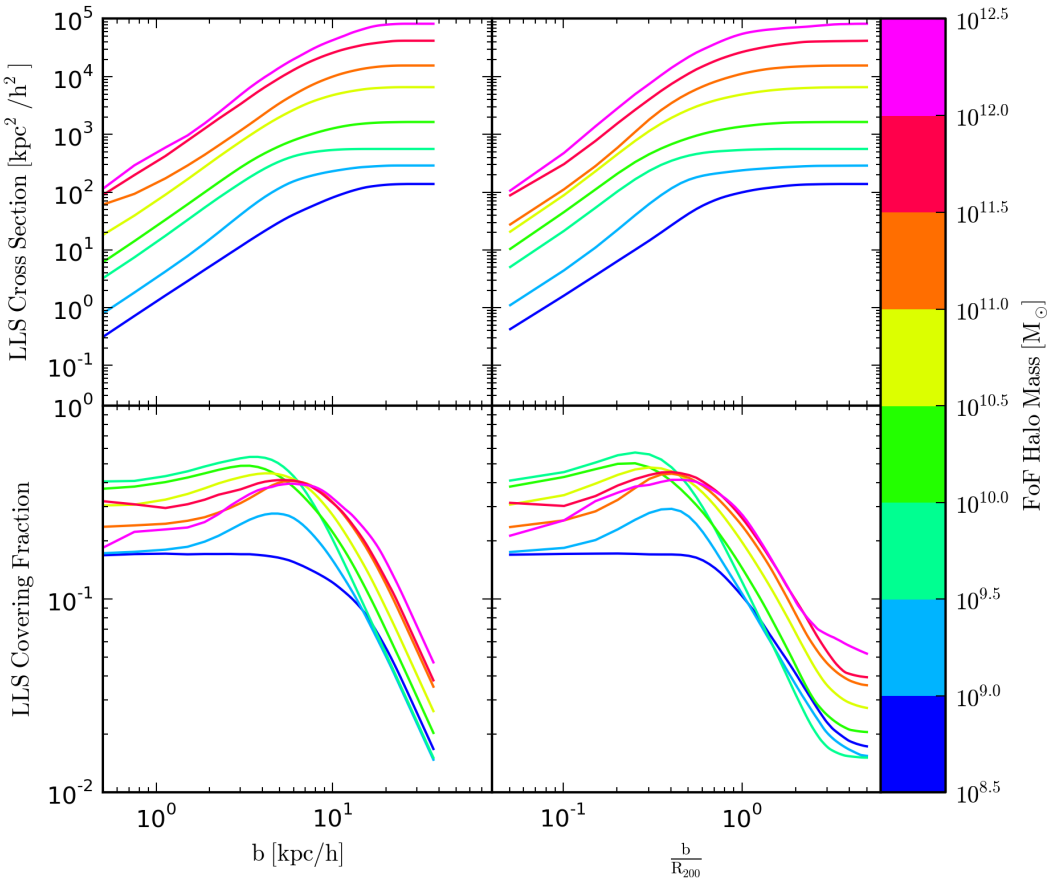

Figure 4.3: The typical LLS cross section (top) and covering fraction (bottom) radial profile as a function of comoving impact parameter (left) and impact parameter over virial radius (right), for our sample of projected FoF halos, binned by halo mass. Within each mass bin, each halo projection's PDF is weighted by an integral of the halo mass function. As expected, high mass halos achieve larger LLS cross sections than low mass halos at all radii, yielding a consistently shaped radial profile for all halo masses. The LLS covering fraction however is complicated by the abundance of DLA, with near-unit covering at low radii – see figure 4.2. There is no clear evolution of the covering fraction radial profile with halo mass, despite their being broadly consistent in shape – constant up until $\sim$ 50kpc/h before declining steadily.

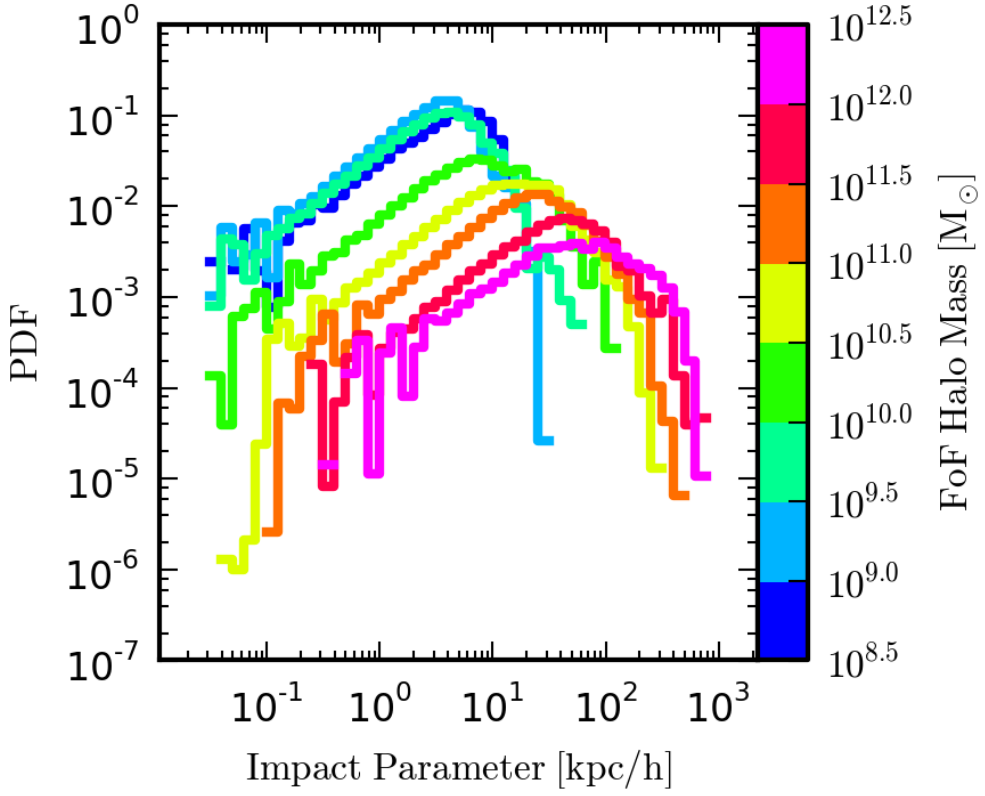

Figure 4.4: The PDF of impact parameter for DLA sightlines intersecting our sample of projected FOF halos, binned by halo mass. Within each mass bin, each halo projection's PDF is weighted by its total DLA cross section and by an integral of the halo mass function. As cross section goes up with radius squared, and because DLA is available at higher impact parameters for more massive halos – the PDF migrates to higher impact parameters with increasing halo mass.

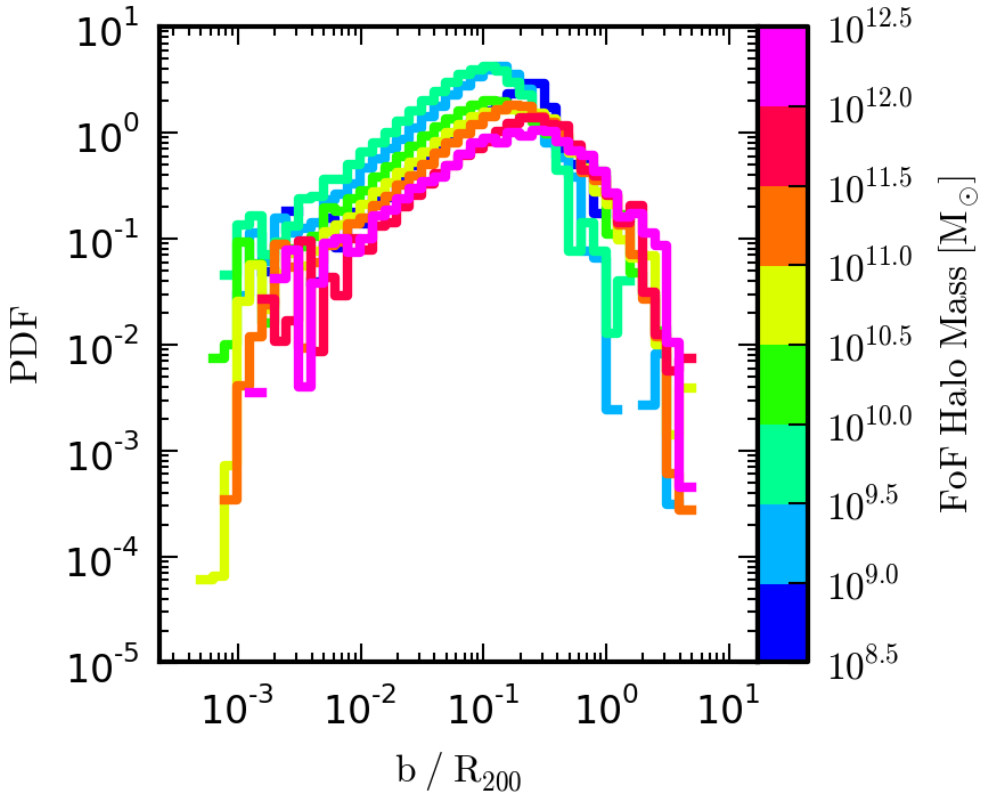

Figure 4.5: The PDF of impact parameter over virial radius for DLA sightlines intersecting our sample of projected FOF halos, binned by halo mass. Within each mass bin, each halo projection's PDF is weighted by its total DLA cross section and by an integral of the halo mass function. These PDFs are broadly consistent between halo masses. However, there is some inflation of the DLA cross section out to larger b/R_{200} values for higher mass halos. Again, low mass $< 10^9[M_\odot]$ halos appear to be an exception to this observation.

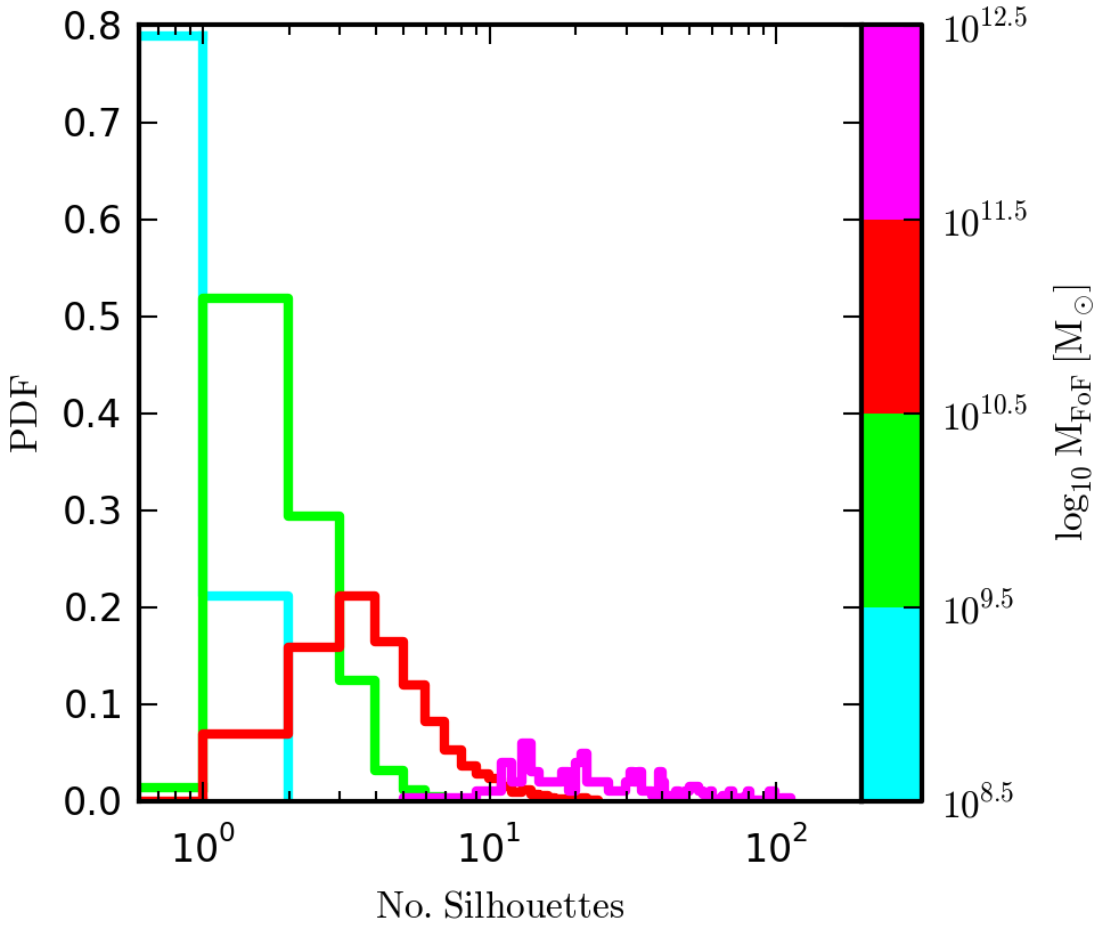

Figure 4.6: The number of continuous DLA projections (or silhouettes) for our sample of projected FOF halos, binned by halo mass. Within each mass bin, each halo projection's PDF is weighted by an integral of the halo mass function. The DLA covering is far more fragmented for high mass halos than for low mass halos. It would be unwise to assume that DLA host halos are enveloped by a continuous, spherically symmetric distribution of H I gas. Note the log-scale: it was necessary to align each bar with the right hand side of its bin.

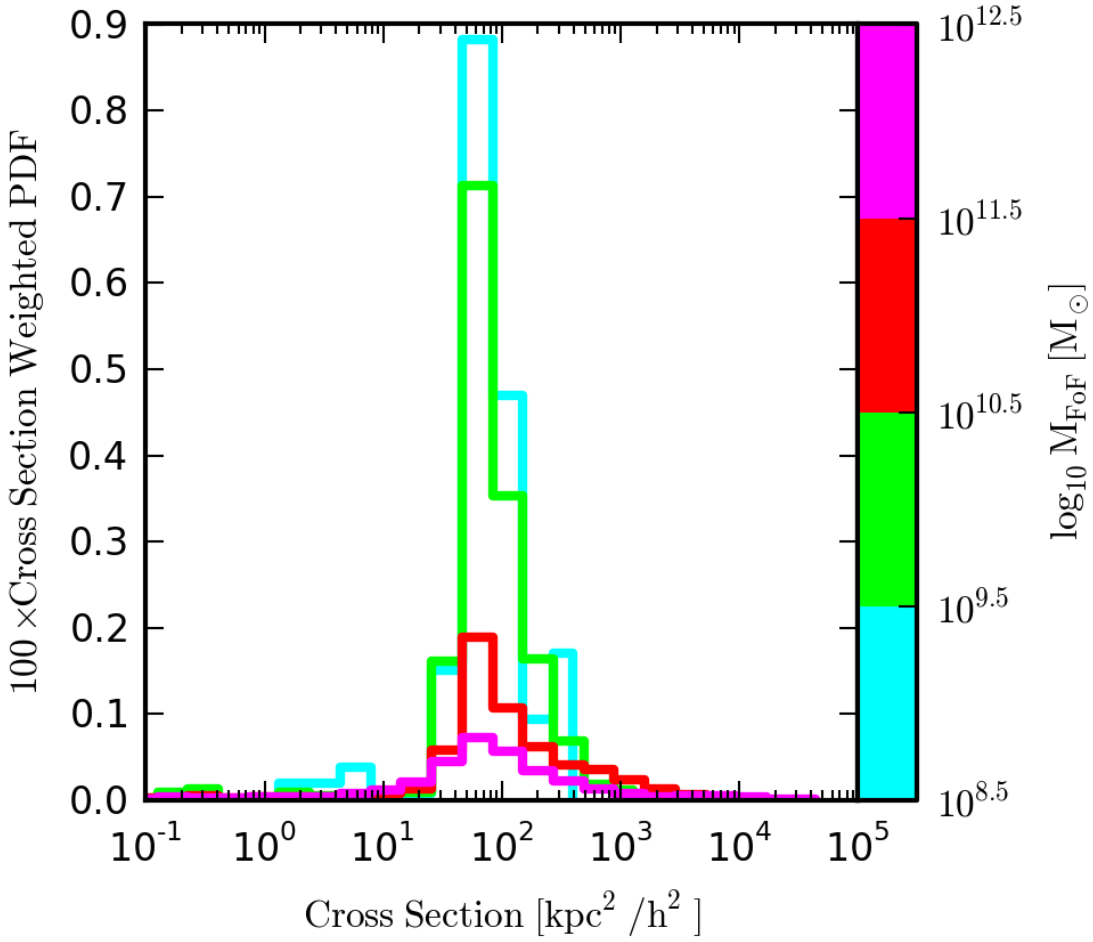

Figure 4.7: The cross section weighted PDF of continuous DLA projection (or silhouette) sizes for our sample of projected FOF halos, binned by halo mass. In other words: the likelihood of intersecting a DLA silhouette of a given size. Within each mass bin, each halo projection's PDF is weighted by an integral of the halo mass function. The DLA covering is far more fragmented for high mass halos than for low mass halos, yielding a broader range of silhouette sizes. Overall, small-but-common silhouettes and large-but-rare silhouettes produce a near-symmetric (in log space) PDF for all halo masses, peaking at $\sim 65 \mathrm{kpc}^2/\mathrm{h}^2$. Note that each silhouette may infact be due to the projection of multiple distinct regions of neutral gas along the line of sight.

4.2 Further Saturation Bias

In this section, we revisit the effects of saturation bias (section 3.2.5)

As a thought experiment, we consider 9 consecutive absorbers of temperature 10^4K. Each absorber occupies a single velocity phase e.g. a non-diverging/collapsing, non-turbulent cloud of gas. We separate these absorbers sufficiently in velocity space such that their optical depth profiles appear discrete. Each absorber has a geometrically decreasing column density, starting at the DLA threshold. We assume a solar silicon-to-metal abundance ratio (Asplund et al., 2009). Thus: $N_{\rm SiII} = 2^{-n} \times 10^{20.3-4.49+[\rm M/H]}[\rm cm^{-2}]$ for $n \in [0, 8]$. This setup will allow us to demonstrate that low column density absorbers may bias velocity widths to high values, contrary to the motivation behind the v_{90} statistic.

In the top panel of figure 4.8, we show the 1526Å Si II intrinsic optical depth profile for these consecutive absorbers. We vary the metallicity of the absorbers over two orders of magnitude, from $[M/H] = -0.5$ to $[M/H] = -2.5$, as colored in the inset which also serves as a colorbar. The highest column density (principal) absorber peaks at $\tau = 144$ at $[M/H] = -0.5$ (dark red) and $\tau = 1.44$ at $[M/H] = -2.5$ (dark blue) – recall that intrinsic optical depth is linearly proportional to column density by definition. This metallicity range encompasses most DLAs and almost all of the observational sample in Neeleman et al. (2013).

In the bottom panel, we show the corresponding apparent optical depth profiles, observed using a FWHM=8 km/s Gaussian instrument. We do not smooth the apparent optical depth profiles. The effects of saturation on these unresolved absorbers are clearly evident as the principal absorber peaks at $\tau_{\rm app} = -ln(0.1)$ at $[M/H] = -0.5$ (dark red) – apparently unsaturated despite an intrinsic optical depth of 144! At this metallicity, the amplitude of $\tau_{\rm app}$ does not follow a geometric distribution and low column density absorbers now appear significant. In fact, the velocity width at $[M/H] = -0.5$ is calculated to be 210 km/s – the two outermost absorbers are sufficient to influence v_{90} despite containing just 0.587% of the total column density:

$$\frac{\sum_{n=7}^{n=8} 2^{-n}}{\sum_{n=0}^{n=8} 2^{-n}} = 5.87 \times 10^{-3} \tag{4.2.1}$$

At $[M/H] = -2.5$ (dark blue) the principal absorber peaks at $\tau_{\rm app} = -ln(0.6)$ – sufficiently strong for the profile to be considered suitable for measuring sightline kinematics. However, even in this low optical depth regime, the amplitude of $\tau_{\rm app}$ does not follow a truly geometric distribution and low column density absorbers are relatively more significant than in the intrinsic optical depth case. The measured velocity width is 125 km/s, being determined by the four outermost absorbers, despite containing just 2.94% of the total column density.

Note that the actual values of v_{90} above are unimportant as we (somewhat arbitrarily) chose the velocity phases for each absorber to occupy. What is important is that low column density features on the outskirts of optical depth profiles may determine velocity widths due to saturation effects. This bias towards higher velocity widths originates in the definition of v_{90} – see section 2.5 and equations 2.5.1; this statistic being dependant on the total integrated apparent optical depth.

As outlying, low column density absorption features are common, saturation bias effects the DLA VWD, as seen in section 3.2.5, and is exacerbated by choosing the strongest "unsaturated" low ion metal transition on which to measure sightline kinematics.

However, this is only strictly true for absorbers occupying discrete velocity phases. Overlapping phases yield extended absorption features, over which saturation information is not lost.

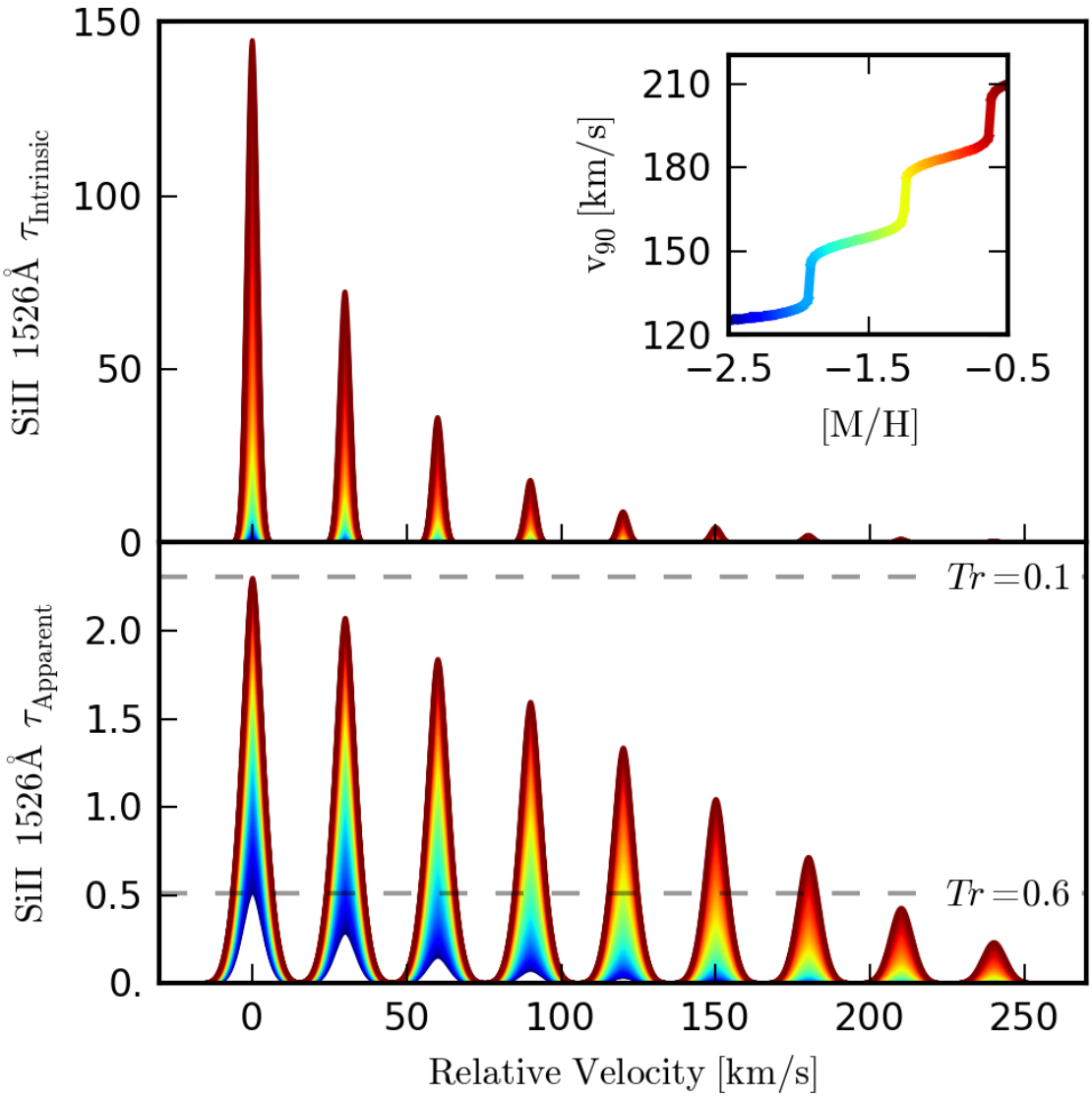

Figure 4.8: Top: the intrinsic Si II 1526Å optical depth profile for 9 consecutive absorbers at 10^4K, each occupying a single velocity phase. $N_{\rm SiII} = 2^{-n} \times 10^{20.3-4.49+[{\rm M/H}]}[{\rm cm}^{-2}]$, $n \in [0, 8]$. The absorber metallicity is varied over two orders of magnitude, as coloured in the inset, which also serves as a colorbar. Bottom: The corresponding apparent optical depth profiles, observed using a FWHM=8 km/s Gaussian instrument. Inset: v_{90} for this thought experiment as a function of [M/H]. The absolute values of v_{90} here are not important. What matters is that low column density features on the outskirts of optical depth profiles may determine velocity widths due to saturation effects.

4.3 Stochastic Velocity Width

Previous we have seen that velocity width does not appear correlated with impact parameter: see figures 3.8 and 2.2. This is a counterintuitive result which we quantify further in section 4.4.

Here, we present two visualisations of an isolated FoF halo in order to better communicate the message that v_{90} is a highly stochastic statistic. This observation simply reflects the diversity of configurations of neutral gas that may be randomly probed by a background quasar sightline – even for isolated FoF halos. Neutral gas is not distributed in a spherically symmetric way around DLA host galaxies or halo structures.

In figure 4.9, we project the H I and Si II column densities for an isolated $10^{11.86} M_{\odot}$ mass FoF halo, alongside a map of velocity widths. In this instance, we calculated v_{90} for all sightlines intersecting the halo, not just those host to DLA. At the centre of the halo, you can clearly make out (in N_{SiII}) an edge-on disk galaxy. This structure is less obvious in N_{H1} because of our chosen colour scale which highlights the various DLA, LLS, and Lyman-α forest silhouettes. We have added a black contour to the velocity width map to highlight sightlines host to DLA.

In figure 4.10, we project the same velocity width map, limited to DLA sightlines. We plot six example apparent optical depth profiles demonstrating the diversity of profile shapes that may arise from a single FoF halo. The top two spectra are particularly interesting, yielding dramatically different profiles and velocity widths despite both intersecting a small DLA silhouette.

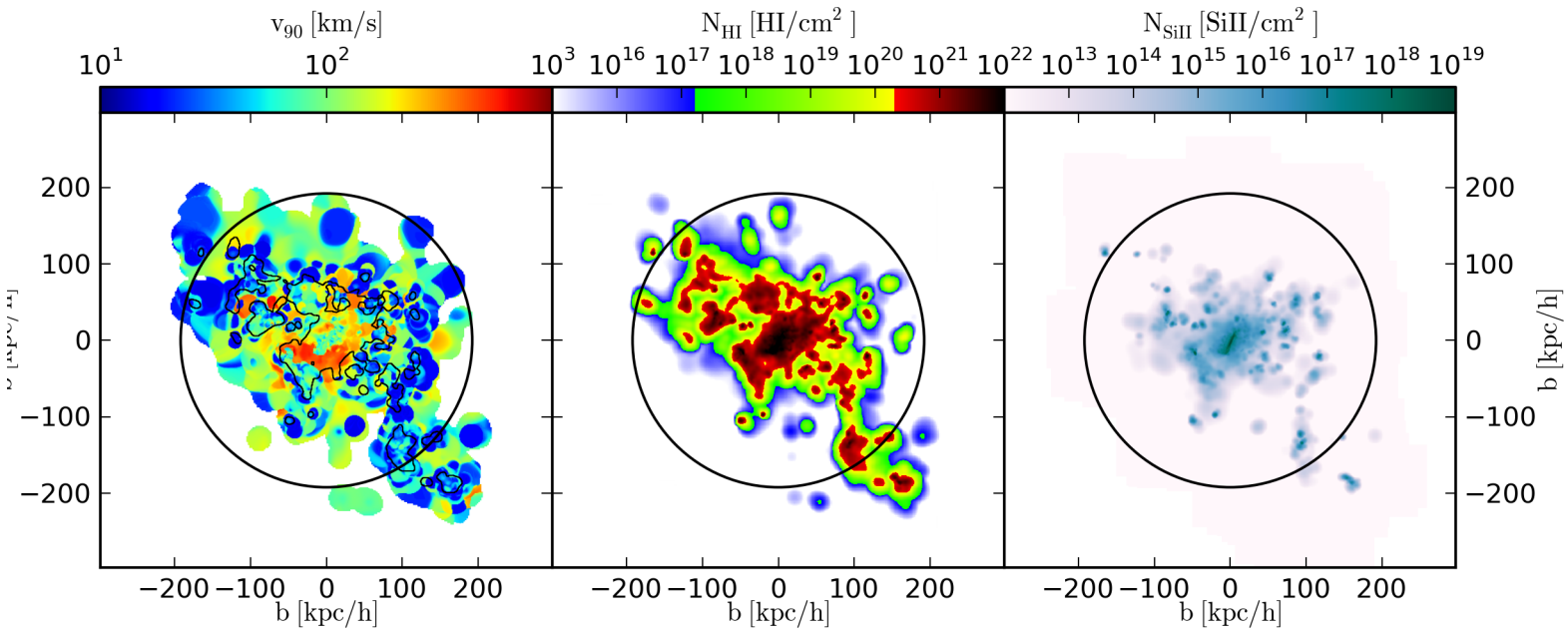

Figure 4.9: The H I (middle) and Si II (right) column density projections, alongside a map of velocity widths (left), for all sightlines intersecting a $10^{11.86} M_{\odot}$ mass FoF halo – host to an edge-on spiral galaxy. The halo's virial radius is shown by the black circle. We find that visualisations such as these better communicate the conclusions in this work; v_{90} is a highly stochastic statistic, reflecting the diversity of configurations of neutral gas that may be randomly intersected by a background quasar sightline.

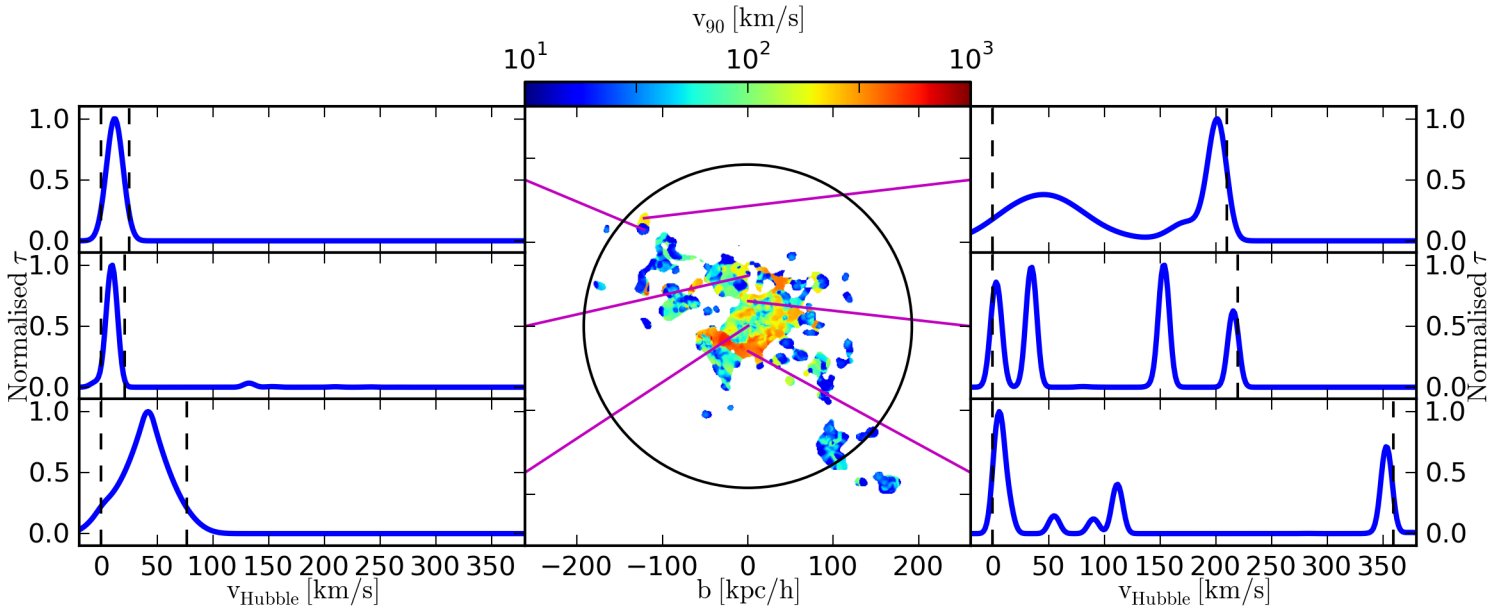

Figure 4.10: A velocity width map for DLA sightlines intersecting a $10^{11.86} M_{\odot}$ mass FoF halo – host to an edge-on spiral galaxy (as per figure 4.9). The halo's virial radius is shown by the black circle. We demonstrate the diversity of profile shapes that may arise from a single FoF halo by plotting six example apparent optical depth profiles for this projection. We do not add artificial noise for display purposes. The top two spectra are particularly interesting, yielding dramatically different profiles and velocity widths despite both intersecting a small DLA silhouette. We find that visualisations such as these better communicate the conclusions in this work; we cannot extract information such as impact parameter from statistics such as v_{90} alone.

4.4 Correlations in more detail

In section 3.7, we presented evidence that H I column density and velocity width are correlated at high column densities.

In figure 4.11, we show explicitly the mass evolution of the velocity width PDF as a function of $N_{\rm HI}$ – the global distribution being shown previously in figure 3.10. It is evident that the spread of the velocity with data and the available v_{90}-$N_{\rm HI}$ space also evolves with host halo mass.

In figure 4.12, we transpose the previous figure, showing the mass evolution of the $N_{\rm HI}$ PDF as a function of velocity width. The previously observed v_{90}-$N_{\rm HI}$ correlation can be seen here as a spur in the data distribution, extending all the way down to the DLA threshold. However, a second, uncorrelated population of DLA sightlines also exists, dominating the $N_{\rm HI}$ PDFs at almost all velocity widths. Fortunately, low column density and low velocity width DLA sightlines are the most common, which may facilitate a diagnostic of host halo mass from these two observables in the future.

In figure 4.13 we show the Si II analogue of figure 4.11. There is no clear correlation between $N_{\rm SiII}$ and v_{90}. Any underlying correlation between the velocity extent of the underlying DLA host halo and $N_{\rm SiII}$ is confused by the practice of choosing the strongest, unsaturated Si II transition on which to measure v_{90}. We stand by our conclusion however that saturation bias most likely contributes to the observed v_{90}-metallicity correlation.

In figure 4.14 we show explicitly the mass evolution of the velocity width PDF as a function of b/R_{200} – the (transposed) global distribution being shown previously in figure 3.8. There is no appreciable evolution of the v_{90}–$N_{\rm HI}$ correlation with b/R_{200}. Neither v_{90} nor $N_{\rm HI}$ are correlated with b/R_{200}.

In figure 4.15 we show explicitly the mass evolution of the velocity width PDF as a function of impact parameter Some evolution of the v_{90}–$N_{\rm HI}$ correlation is present at low column densities, although this is uncertain. It is not likely that the v_{90}–$N_{\rm HI}$ correlation may be used to infer the underlying impact parameter of DLA sightlines, as neither of these observable quantities are correlated with b. We show together the mass evolution of the corresponding PDF medians in figure 4.16.

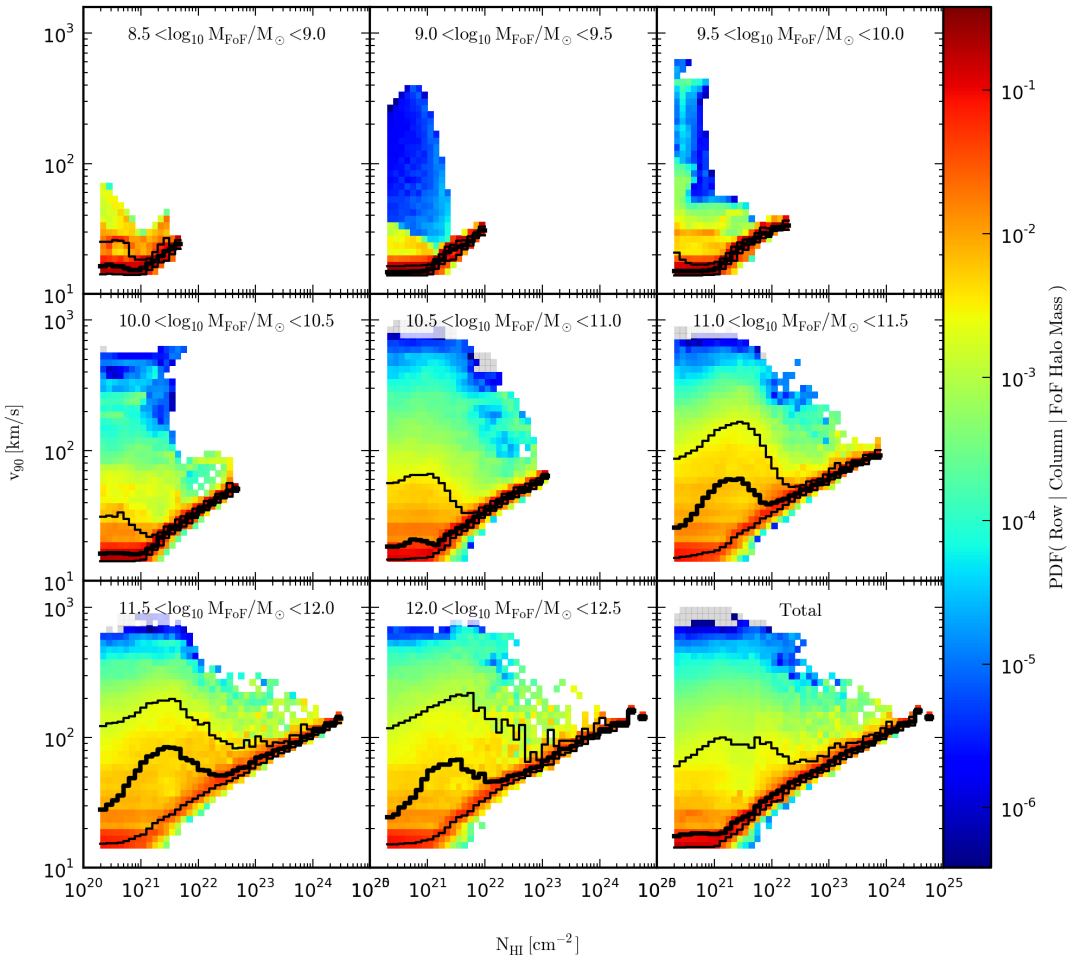

Figure 4.11: The stacked, column normalised PDFs of H I column density as a function of velocity width, binned by halo mass, for our sample of FoF halo projections. Within each mass bin, each halo projection is weighted by its total DLA cross section and by an integral of the halo mass function. The 16th, 50th and 84th percentiles are indicated by the solid black lines. Grey pixels have a probability density less than the colourbar's lower bound. See figures 3.10 and 3.11. Here it is evident that the spread of the velocity with data, and the available v_{90}-$N_{\rm HI}$ space also evolves with host halo mass.

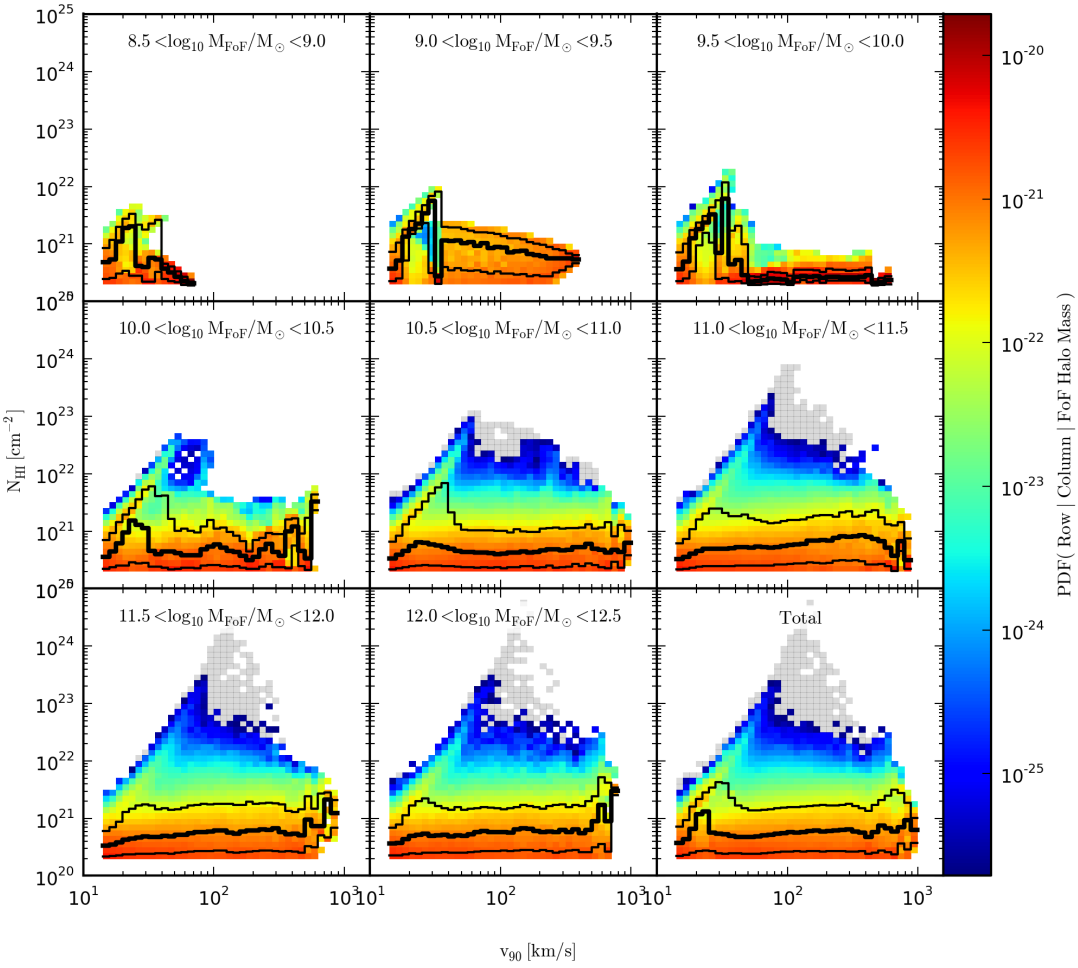

Figure 4.12: The stacked, column normalised PDFs of H I column density as a function of velocity width, binned by halo mass, for our sample of FoF halo projections. Within each mass bin, each halo projection is weighted by its total DLA cross section and by an integral of the halo mass function. The 16th, 50th and 84th percentiles are indicated by the solid black lines. Grey pixels have a probability density less than the colourbar's lower bound. The previously observed v_{90}-$N_{\rm HI}$ can be seen here as a spur in the data distribution, extending all the way down to the DLA threshold. However, a second, uncorrelated population of DLA sightlines also exists, dominating the $N_{\rm HI}$ PDFs at almost all velocity widths. Fortunately, low column density and low velocity width DLA sightlines are the most common, which may facilitate a diagnostic of host halo mass from these two observables in the future.

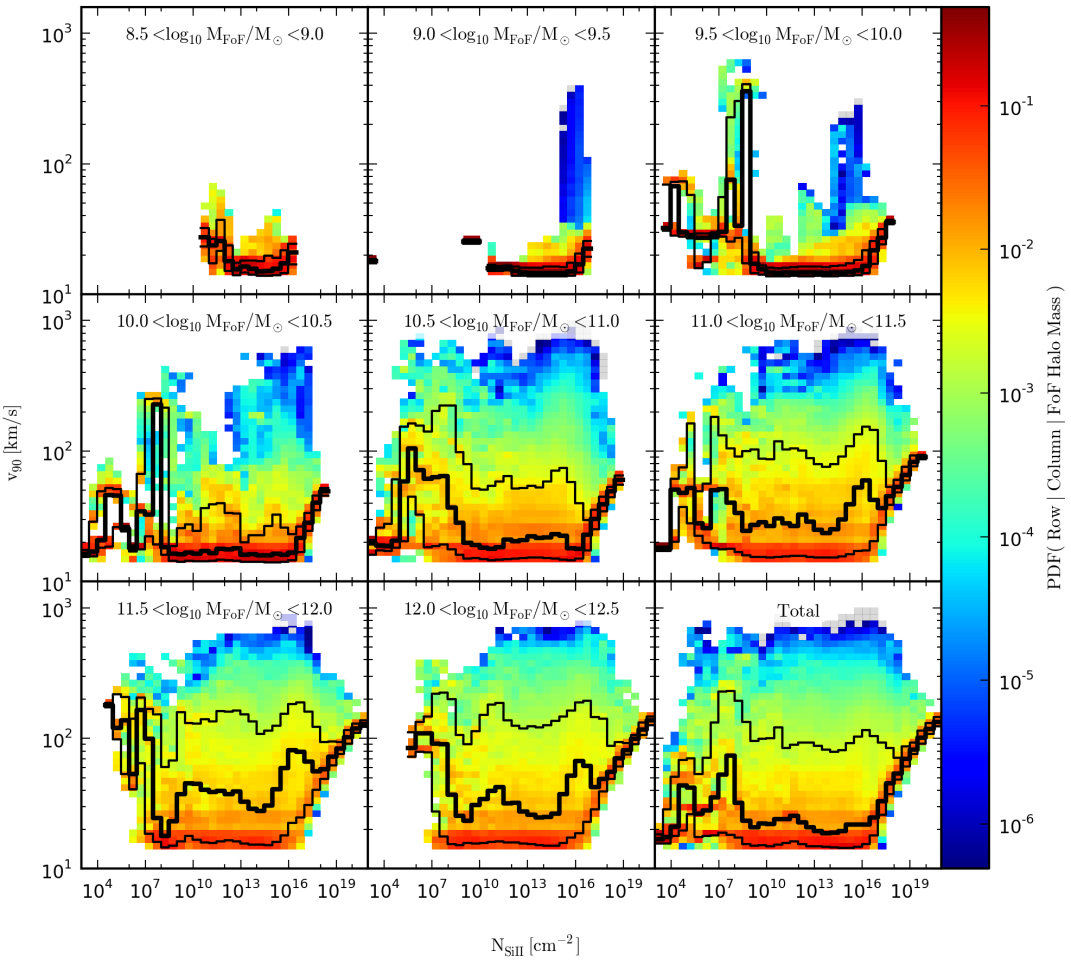

Figure 4.13: The stacked, column normalised PDFs of Si II column density as a function of velocity width, binned by halo mass, for our sample of FoF halo projections. Within each mass bin, each halo projection is weighted by its total DLA cross section and by an integral of the halo mass function. The 16th, 50th and 84th percentiles are indicated by the solid black lines. Grey pixels have a probability density less than the colourbar's lower bound. There is no clear correlation between $N_{\rm SiII}$ and v_{90}. Any underlying correlation between the velocity extent of the underlying DLA host halo and $N_{\rm SiII}$ is confused by the practice of choosing the strongest, unsaturated Si II transition on which to measure v_{90}. We stand by our conclusion however that saturation bias most likely contributes to the observed v_{90}-metallicity correlation.

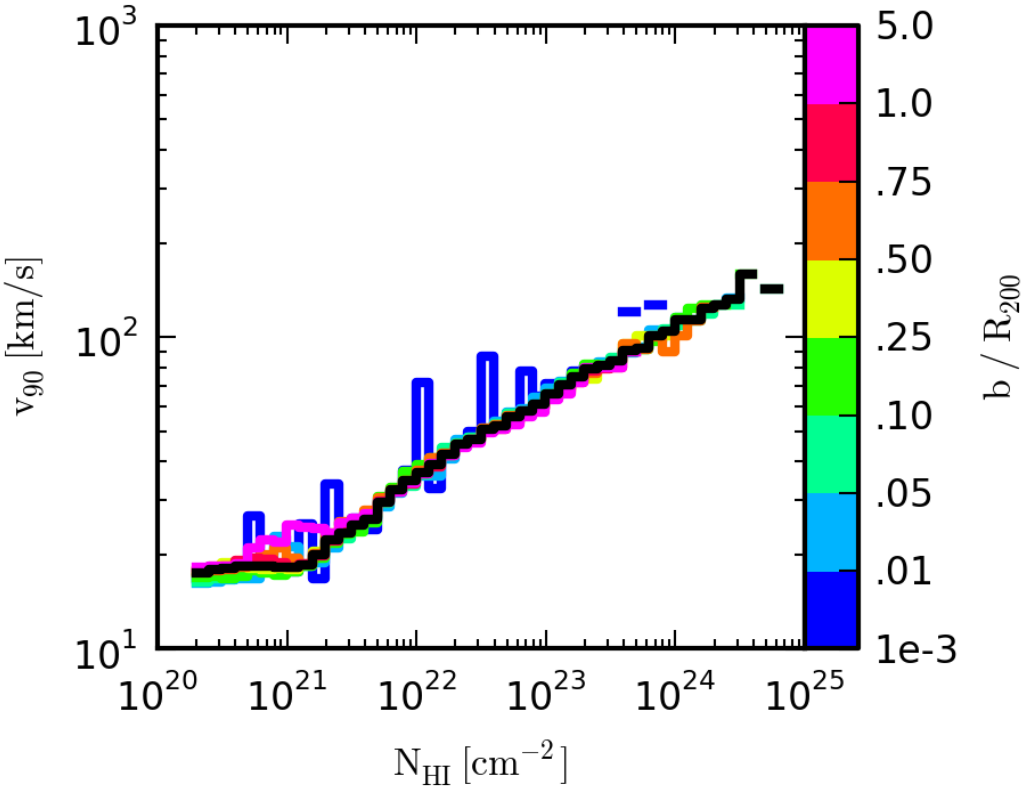

Figure 4.14: The median velocity width as a function of H I column density, binned by impact parameter over virial radius, for our sample of FoF halo projections. Within each b/R_{200} bin, each halo projection is weighted by its total DLA cross section and by an integral of the halo mass function. In black, we also plot the global median as per figure 3.10. There is no appreciable evolution of the v_{90}–N_{HI} correlation with b/R_{200}. Neither v_{90} nor N_{HI} are correlated with b/R_{200}.

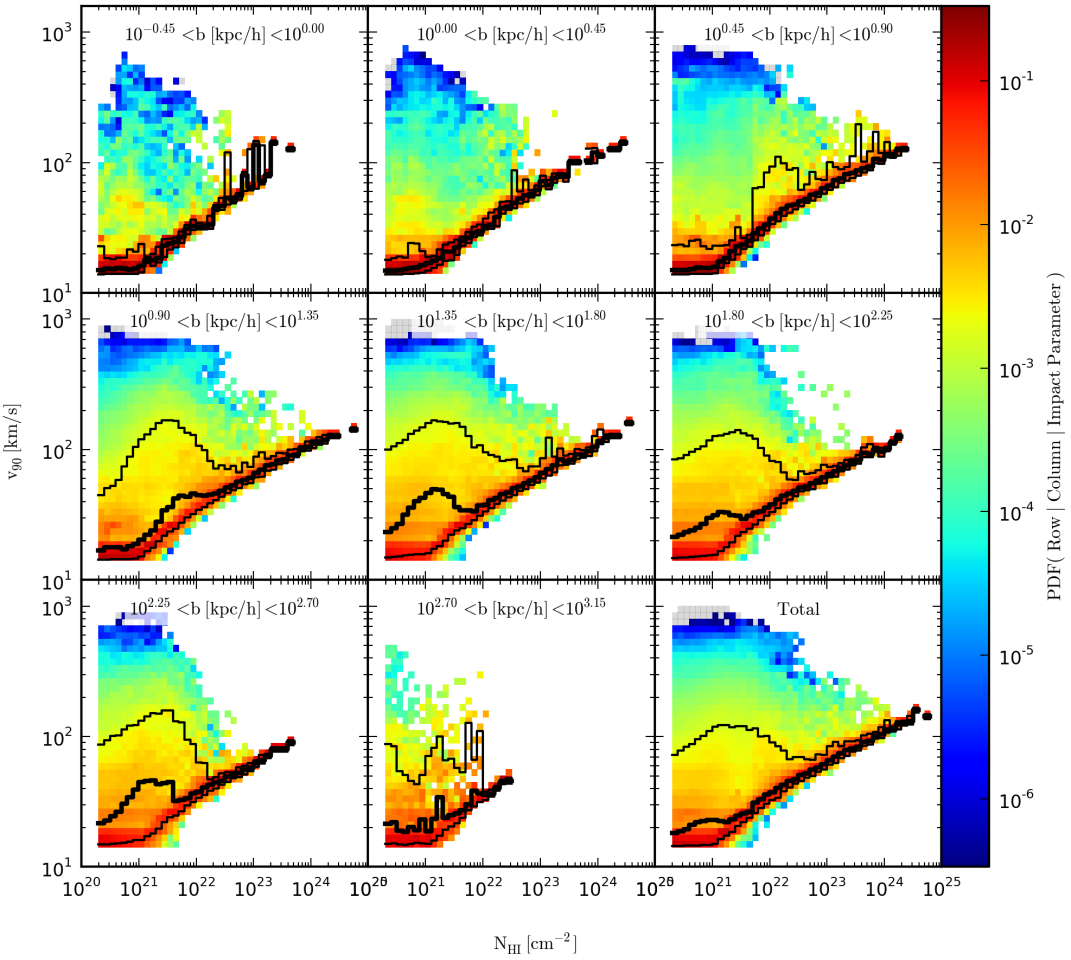

Figure 4.15: The stacked, column normalised PDFs of velocity width as a function of H I column density, binned by comoving impact parameter, for our sample of FoF halo projections. Within each impact parameter bin, each halo projection is weighted by its total DLA cross section and by an integral of the halo mass function. The 16th, 50th and 84th percentiles are indicated by the solid black lines. Some evolution of the v_{90}–N_{HI} correlation is present at low column densities, although this is uncertain. It is not likely that the v_{90}–N_{HI} correlation may be used to infer the underlying impact parameter of DLA sightlines, as neither of these observable quantities are correlated with b. Also see figure 4.16.

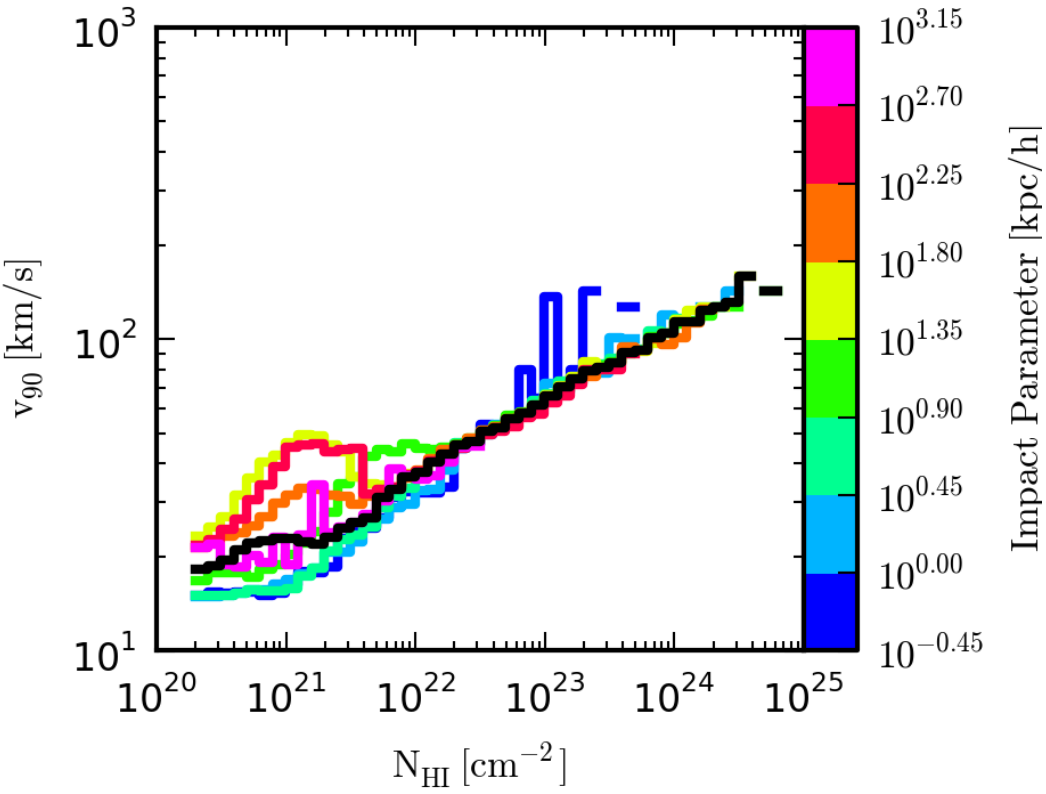

Figure 4.16: The median velocity width as a function of H I column density, binned by comoving impact parameter, for our sample of FoF halo projections. Within each impact parameter bin, each halo projection is weighted by its total DLA cross section and by an integral of the halo mass function. In black, we also plot the global median as per figure 3.10. Some evolution of the v_{90}–N_{HI} correlation is present at low column densities, although this is uncertain. It is not likely that the v_{90}–N_{HI} correlation may be used to infer the underlying impact parameter of DLA sightlines, as neither of these observable quantities are correlated with b. Also see figure 4.15.

4.5 Photoionisation UVB Model

Throughout this work we have assumed a Haardt & Madau (2001) (HM01) model for the photoionising background radiation at redshift $z = 3$. However, we find that the total line density of DLAs in the reference simulation is too low to be consistent with observations. This inconsistency is even worse if we were to adopt the photoionisation fitting formulae of Rahmati et al. (2013a), rather than correct for self shielding using full 3D radiative transfer (Altay & Theuns, 2013). However, some more recent models of the photoionising UVB are of lower amplitude than HM01. It is possible that the HM01 model UVB amplitude is too high in reality, overly suppressing the formation of neutral hydrogen in our simulations. If we were to use a lower amplitude model, it is most likely that the DLA line density would increase. That said, our simulated volume being too small (see section 3.7), is also partially responsible for our low DLA line density.

We show in figure 4.17 the total photoionisation rate as a function of redshift for HM01 and for a lower amplitude model Haardt & Madau (2012) (HM12). Overplotted are the corresponding values derived from Rahmati's fitting formulae.

However, this uncertainty in UVB amplitude and spectral shape is far less significant than that between post-processing radiative transfer models. In figure 4.18 we show that the transition from highly ionised to neutral gas is far steeper in URCHIN (using a HM01 UVB model) than for Rahmati using either a HM01 or HM12 UVB model. It would be interesting to re-analyse the OWLS reference simulation assuming a HM12 photoionisation model – implemented live and in post processing for consistency. No doubt, the resulting updated neutral gas distribution would impact our DLA kinematic analysis.

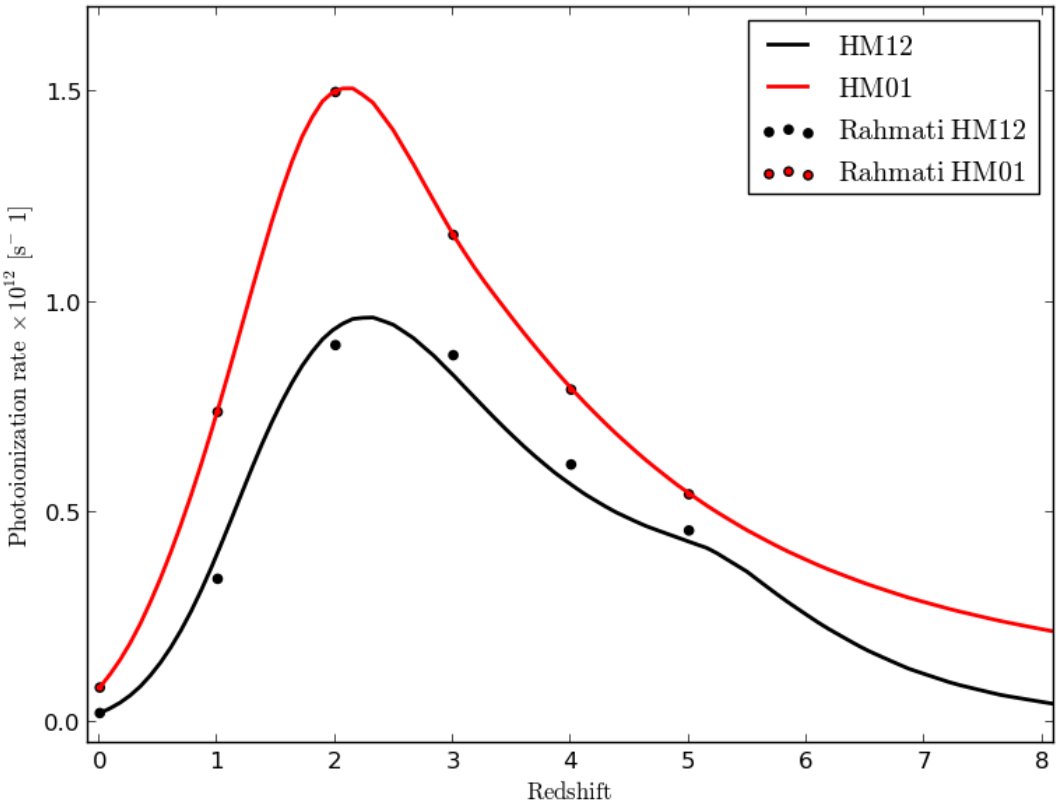

Figure 4.17: The total photoionisation rate of the Universe due to a uniform, isotropic field of photons, as a function of redshift according to two popular models: Haardt & Madau (2001) (red) and more recently Haardt & Madau (2012) (black). Overplotted are the corresponding values derived from the photionisation rate fitting formulae presented in Rahmati et al. (2013a).

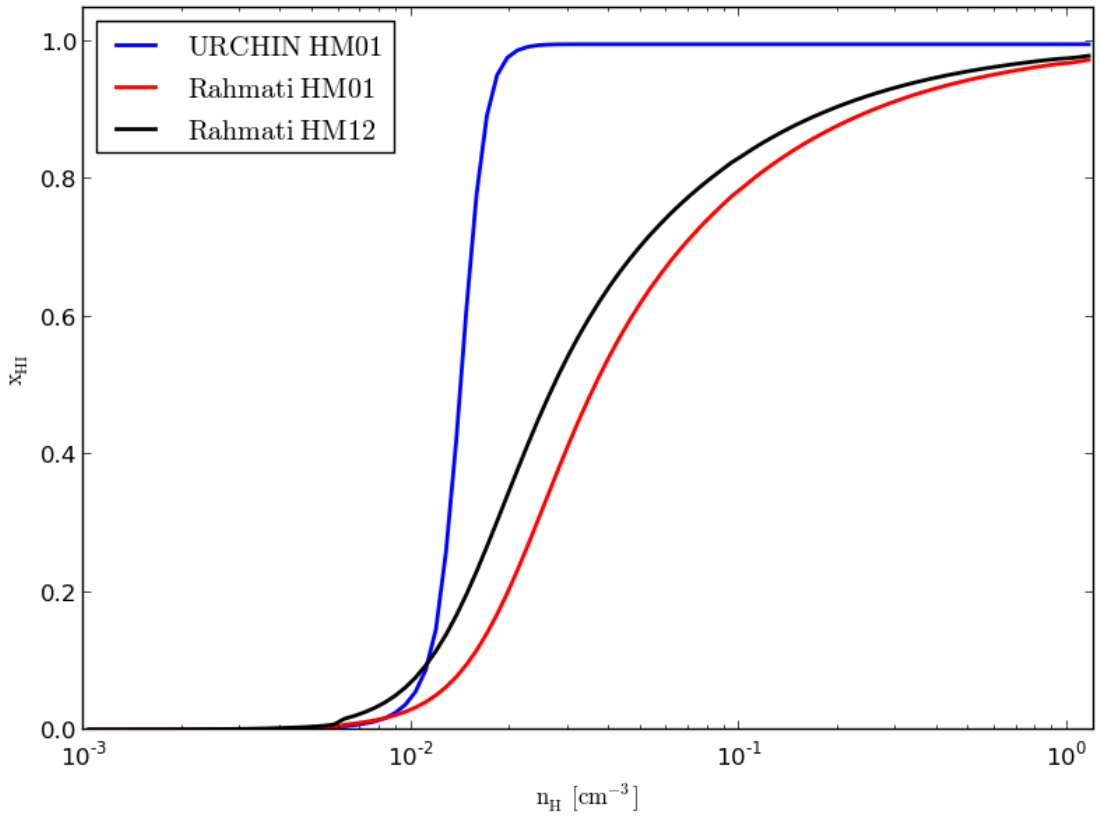

Figure 4.18: The median hydrogen neutral fraction for particles in the reference simulation at redshift $z = 3$ as a function of hydrogen number density. We do not remove molecular hydrogen from the H I field for this exercise. In blue, we show that full, accurate, 3D radiative transfer code URCHIN (Altay & Theuns, 2013) results in a steep transition from highly ionised to neutral gas (assuming HM01). In red/black, we show that the photoionising fitting formulae presented in Rahmati et al. (2013a) results in a far smoother transition (assuming HM01/HM12) – due to their explicit treatment of recombination radiation. The lower amplitude of the HM12 photoionising UVB model moves the ionisation front to slightly lower densities than for HM01.

Chapter 5

Conclusions

We have investigated the velocity widths of Damped Lyman-α Absorption systems, utilizing a suite of cosmological, hydrodynamic simulations, post-processed for radiative transfer. We succeeded in producing high velocity width DLAs, but also produced a persistant over abundance of low velocity width sightlines in comparison with recent observations. The velocity width distribution was found to be remarkably robust to many variations in our implementation and to all reasonable changes to the reference simulation model.

A new discovery was that of "saturation bias" against low velocity width measurements. The velocity widths of narrow apparent optical depth profiles close to saturation are particularly sensitive to outlying, relatively low column density absorption features. This effect is due to intrinsically saturated, unresolved metal lines yielding unsaturated apparent optical depth profiles, even for state of the art high resolution quasar spectra. This caveat may weaken the v_{90}–metallicity correlation seen in observations.

We have derived a novel prescription for unresolved turbulent motion within SPH particles (see appendix) such that their total internal energy is conserved. Both thermal and turbulent broadening contribute to the total Doppler parameter for absorber features in this work.

Another novel prescription defined in this work is that of kinematic weight – a quantification of the contributions by 9 distinct kinematic origins to the DLA VWD:

- Instrumental, thermal and turbulent broadening

- Hydrodynamic / internal gravitational dynamics
- Supernovae feedback / galactic winds
- Satellite motion between galaxy groups
- Relative motion / Hubble flow between unassociated halos
- Significant, serendipitous absorption by the IGM

Notably, we do not interpret metal line absorbers, associted with DLA spectral features, as being exclusively hosted by independant halo structures. Absorbers offset by large comoving separations experiencing Hubble flow are indistinguishable from cospatial absorbers with large relative velocities. Care must be taken in interpreting the physical origins of DLA velocity width measurements.

We also anaylsed 1000 isolated FoF halos in order to better understand the nature of DLA host systems. We found that v_{90} is a highly stochastic statistic, reflecting the diverse configurations of neutral gas that may be probed by an unassociated background quasar. However, we also found that the DLA VWD evolves with host halo mass; and that v_{90} and $N_{\rm HI}$ are strongly correlated at (very) high H I column densities. Hence, it may be possible to constrain DLA host halo masses using these two observable properties. That said, such a diagnostic will be hindered by multiple halo intersections, projection effects and the fact that such column density sightlines are very rare.

Below, we candidly identify the main limitations of this work:

- Our results are not converged with respect to the size of the cosmological volume. High mass mass halo structures not probed within our limited simulation volume are expected to influence both our DLA population and kinematic results.
- It is most likely that our results are not converged with respect to the particle mass resolution. Sub-resolution scale real/velocity space structures have the potential to alleviate our over-abundance of single velocity phase, low velocity width systems.

- We cannot rule out that the absence of metal diffusion between SPH particles has affected our results, although we found no direct evidence that this is the case.

- We identified a peculiar population of low mass but (nevertheless) neutral clouds in our simulations that contributed to the DLA population. These objects may be numerical artifacts of the hydrodynamics.

- The choice of (post-processing) self-shielding implementation significantly affects the H I distribution within our simulations.

- We only considered one photoionizing UVB radiation model in this work.

- We did not include local (stellar/accreting black hole) sources of photoionizing radiation in this work.

- Our reference DLA line density (abundance) is only about half that found by recent observations, despite matching the observed CDDF of H I well, over ten orders of magnitude (Altay et al., 2011).

- We did not *directly* verify whether neglecting the slightly higher IP of Si II than that of H I, may be biasing our velocity width measurements to low values (as concluded by Bird et al., 2015). However, it is a fundamental assumption of DLA kinematic analysis that associated low-ion metal lines trace the velocity field of any underlying neutral gas.

Relevant areas not investigated in this work include kinematic statistics other than v_{90} (Prochaska & Wolfe, 1997), the observed velocity width – metallicity correlation between DLAs and further, the plane correlation between $\log_{10}(v_{90})$, redshift and metallicity (Neeleman et al., 2013). We look forward to such matters being addressed in future work. Huge (100^3Mpc^3), high resolution (2×1504^3 particles), cutting edge cosmological hydrodynamical simulations such as EAGLE (Schaye et al., 2015) present exciting, fresh opportunities for the community to further our understanding of DLA systems.

Appendices

A Particle Turbulence

The internal energy per unit mass u for a SPH particle with pressure P and density ρ is given by:

$$u = \frac{P}{(\gamma - 1)\rho} \ , \tag{A1}$$

where $\gamma = 5/3$ is the ratio of specific heats. The temperature stored for such particles is given by:

$$T_{\rm part} = \frac{\mu m_{\rm P}}{k_{\rm B}} \frac{P}{\rho} \ , \tag{A2}$$

where $k_{\rm B}$ is Boltzmann's constant, $m_{\rm P}$ is the proton mass and μ is the particle's mean molecular weight. As the average molecular kinetic energy per unit mass $u_{\rm therm}$ for an ideal gas at temperature T is simply:

$$u_{\rm therm} = \frac{3}{2} \frac{k_{\rm B} T}{\mu m_{\rm P}} \ , \tag{A3}$$

it follows that $u_{\rm therm} \equiv u$ provided that $T = T_{\rm part}$.

However, for particles that fall on the polytropic equation of state:

$$P = P^* \left(\frac{\rho}{\rho^*} \right)^{\gamma_{\rm eff}} \ , \tag{A4}$$

it can be shown that the stored temperature is simply a function of the gas density. Note: $P^*/k_{\rm B} = 1.08 \times 10^3$ cm^{-3} K is the pressure at the equation of state threshold ρ^*, and the value $\gamma_{\rm eff} = 4/3$ was chosen to prevent the spurious fragmentation high density gas due to a lack of numerical resolution (Robertson & Kravtsov, 2008; Schaye & Dalla Vecchia, 2008). We set the temperature of these EoS particles to equal $T_{\rm EoS} = 10^4$ K – a value typical of the warm-neutral phase of the ISM. In order to conserve the total internal energy of these particles, as used in the simulations, we attribute a fraction (ϵ) of the missing energy per unit mass $u_{\rm turb}$ to unresolved turbulent motion:

$$\frac{u_{\rm turb}}{\epsilon} = \frac{P^*}{(\gamma - 1)\rho *} \left(\frac{\rho}{\rho^*} \right)^{\gamma_{\rm eff} - 1} - \frac{3}{2} \frac{k_{\rm B} T_{\rm EoS}}{\mu m_{\rm P}} \ , \tag{A5}$$

Only the corresponding turbulent velocity dispersion of gas in one dimension will contribute to the Doppler-broadening of any corresponding absorption. Hence the internal, unresolved turbulent velocity dispersion $\sigma_{\rm turb}$ for each particle is given by:

$$\sigma_{\rm turb} = \sqrt{\frac{2}{3} u_{\rm turb}} \ , \tag{A6}$$

$\sigma_{\rm turb}$ is projected along 1D real space sightlines, weighted by the particle kernel and ion number density in the same manner as other particle properties, see section 2.4. We calculate the absorber's Doppler broadening parameter b (not to be confused with sightline impact parameter b) by adding in quadrature the thermal component $b_{\rm therm}$ to the turbulent component $b_{\rm turb}$ thus (Meiksin, 2009):

$$b_{\rm therm} = \sqrt{\frac{2k_{\rm B}T}{m_{\rm ion}}} \ , \tag{A7a}$$

$$b_{\rm turb} = \sqrt{2}\sigma_{\rm turb} \ , \tag{A7b}$$

$$b = \sqrt{b_{\rm therm}^2 + b_{\rm turb}^2} \ , \tag{A7c}$$

where $m_{\rm ion}$ is the ion mass.

In summary:

$$b = \sqrt{\frac{4}{3}\left(\epsilon u + \left(\frac{\mu m_{\rm P}}{m_{\rm ion}} - \epsilon\right) u_{\rm therm}\right)} \ , \tag{A8}$$

By setting $\epsilon = 1.0$ in this work, the spectral broadening for each absorber is independent of the modified particle temperatures: $T_{\rm EoS}$ and $T_{\rm shld}$. However, the final ionisation states for each particle do depend on these values.

/

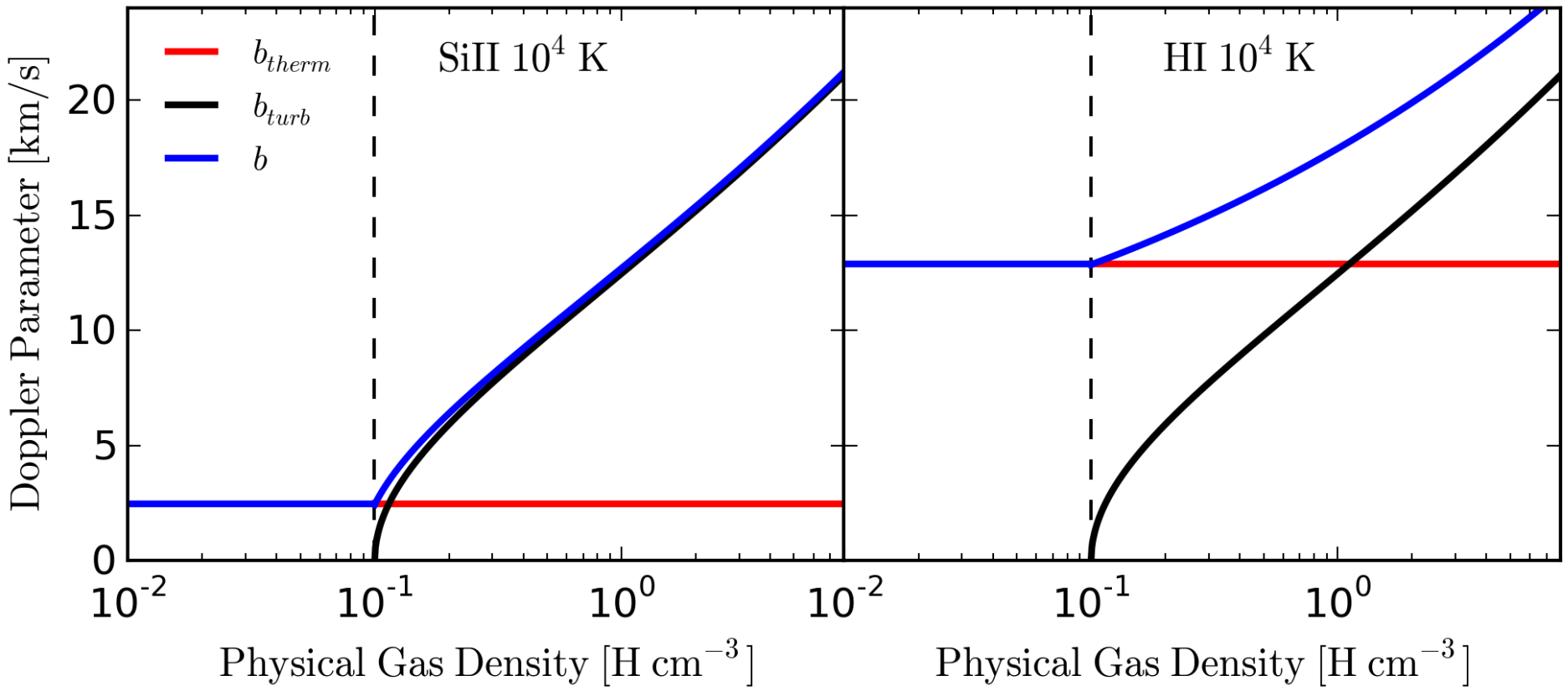

Figure A.1: Doppler parameter (blue, b) as a function of physical gas density for 10^4K Si II (left) and H I (right) gas, broken down by the thermal (red, b_{therm}) and turbulent (black, b_{turb}) broadening components.

Bibliography

Altay G., Theuns T., 2013, MNRAS, 434, 748

Altay G., Theuns T., Schaye J., Booth C. M., Dalla Vecchia C., 2013, MNRAS, 436, 2689

Altay G., Theuns T., Schaye J., Crighton N. H. M., Dalla Vecchia C., 2011, ApJ, 737, L37

Asplund M., Grevesse N., Sauval A. J., Scott P., 2009, ARA&A, 47, 481

Bahcall J. N., Peebles P. J. E., 1969, ApJ, 156, L7

Barnes L. A., Haehnelt M. G., 2014, MNRAS, 440, 2313

Bird S., Haehnelt M., Neeleman M., Genel S., Vogelsberger M., Hernquist L., 2015, MNRAS, 447, 1834

Blitz L., Rosolowsky E., 2006, ApJ, 650, 933

Cen R., 2012, ApJ, 748, 121

Dalla Vecchia C., Schaye J., 2008, MNRAS, 387, 1431

Dalla Vecchia C., Schaye J., 2012, MNRAS, 426, 140

Davis M., Efstathiou G., Frenk C. S., White S. D. M., 1985, ApJ, 292, 371

Dolag K., Borgani S., Murante G., Springel V., 2009, MNRAS, 399, 497

Ferland G. J. et al., 2013, Rev. Mexicana Astron. Astrofis., 49, 137

Fumagalli M., O'Meara J. M., Prochaska J. X., Kanekar N., Wolfe A. M., 2014, MNRAS, 444, 1282

Haardt F., Madau P., 2001, in Clusters of Galaxies and the High Redshift Universe Observed in X-rays, Neumann D. M., Tran J. T. V., eds.

Haardt F., Madau P., 2012, ApJ, 746, 125

Hong S., Katz N., Davé R., Fardal M., Kereš D., Oppenheimer B. D., 2010, ArXiv e-prints

Meiksin A. A., 2009, Reviews of Modern Physics, 81, 1405

Morton D. C., 2003, ApJS, 149, 205

Neeleman M., Wolfe A. M., Prochaska J. X., Rafelski M., 2013, ApJ, 769, 54

Noterdaeme P. et al., 2012, A&A, 547, L1

Noterdaeme P., Petitjean P., Ledoux C., Srianand R., 2009, A&A, 505, 1087

Okamoto T., Gao L., Theuns T., 2008, MNRAS, 390, 920

Pawlik A. H., Schaye J., 2008, MNRAS, 389, 651

Pawlik A. H., Schaye J., 2011, MNRAS, 412, 1943

Pawlik A. H., Schaye J., van Scherpenzeel E., 2009, MNRAS, 394, 1812

Pontzen A. et al., 2008, MNRAS, 390, 1349

Prochaska J. X., 2003, ApJ, 582, 49

Prochaska J. X., Herbert-Fort S., Wolfe A. M., 2005, ApJ, 635, 123

Prochaska J. X., Wolfe A. M., 1997, ApJ, 487, 73

Prochaska J. X., Wolfe A. M., 2010, ArXiv e-prints

Rahmati A., Pawlik A. H., Raicevic M., Schaye J., 2013a, MNRAS, 430, 2427

Rahmati A., Schaye J., Pawlik A. H., Raicevic M., 2013b, MNRAS, 431, 2261

Raicevic M., Pawlik A. H., Schaye J., Rahmati A., 2014, MNRAS, 437, 2816

Robertson B. E., Kravtsov A. V., 2008, ApJ, 680, 1083

Schaye J. et al., 2015, MNRAS, 446, 521

Schaye J., Dalla Vecchia C., 2008, MNRAS, 383, 1210

Schaye J. et al., 2010, MNRAS, 402, 1536

Spergel D. N. et al., 2007, ApJS, 170, 377

Springel V., 2005, MNRAS, 364, 1105

Springel V., White S. D. M., Tormen G., Kauffmann G., 2001, MNRAS, 328, 726

Tescari E., Viel M., Tornatore L., Borgani S., 2009, MNRAS, 397, 411

Theuns T., Leonard A., Efstathiou G., Pearce F. R., Thomas P. A., 1998, MNRAS, 301, 478

Theuns T., Viel M., Kay S., Schaye J., Carswell R. F., Tzanavaris P., 2002, ApJ, 578, L5

Vogt S. S. et al., 1994, in Society of Photo-Optical Instrumentation Engineers (SPIE) Conference Series, Vol. 2198, Instrumentation in Astronomy VIII, Crawford D. L., Craine E. R., eds., p. 362

Wiersma R. P. C., Schaye J., Smith B. D., 2009, MNRAS, 393, 99

Wiersma R. P. C., Schaye J., Theuns T., Dalla Vecchia C., Tornatore L., 2009, MNRAS, 399, 574

Wolfe A. M., Gawiser E., Prochaska J. X., 2005, ARA&A, 43, 861

Wolfe A. M., Turnshek D. A., Smith H. E., Cohen R. D., 1986, ApJS, 61, 249